THE UNIVERSITY OF CHICAGO

INTERACTIONS OF ATOMIC AND MOLECULAR SPECIES WITH ICE AND SELF-ASSEMBLED MONOLAYERS

A DISSERTATION SUBMITTED TO
THE FACULTY OF THE DIVISION OF THE PHYSICAL SCIENCES
IN CANDIDACY FOR THE DEGREE OF
DOCTOR OF PHILOSOPHY

DEPARTMENT OF CHEMISTRY

BY
WENXIN LI

CHICAGO, ILLINOIS
DECEMBER 2015

TABLE OF CONTENTS

LIST OF FIGURES v

ACKNOWLEDGEMENTS viii

ABSTRACT x

CHAPTER 1 1

INTRODUCTION 1

- 1.1 Motivation 1
- 1.2 Organization of this thesis 2
- References 5

CHAPTER 2 7

EXPERIMENTAL SETUP AND TECHNIQUES 7

- 2.1 The Molecular Beam Source 7
- 2.2 Ultra-high Vacuum (UHV) Surface Analysis Chamber 9
- 2.3 Reflection-Absorption Infrared Spectroscopy (RAIRS) 10
- 2.4 X-ray Photoelectron Spectroscopy (XPS) 13
- 2.5 Time-of-Flight (TOF) Techniques 15
- References 17

CHAPTER 3 18

FORMATION OF STABILIZED KETENE INTERMEDIATES IN THE REACTION OF O(^{3}P) WITH OLIGO(PHENYLENE ETHYNYLENE) THIOLATE SELF-ASSEMBLED MONOLAYERS ON AU(111) 18

- 3.1 Introduction 19
- 3.2 Experimental 21
  - A. SAM Preparation 21
  - B. Molecular Beam/Reflection-Absorption Infrared Spectroscopy 21
  - C. UHV-STM 22
- 3.3 Results 23
- 3.4 Discussion 27
  - A. Mechanism of O(^{3}P)/oPE-SAM Reaction 27
  - B. Kinetics of the O(^{3}P)/oPE-SAM Reaction 34
- 3.5 Conclusions 37
- 3.6 Acknowledgments 38

References..38
CHAPTER 4..42
MOLECULAR INTERACTIONS WITH ICE: MOLECULAR EMBEDDING, ADSORPTION, DETECTION AND RELEASE..42
4.1 Introduction..43
4.2 Experimental..47
A. Thermal Desorption..47
B. RAIRS..50
4.3 Results and Discussion..51
A. Thermal Desorption..52
B. RAIRS..65
C. Comparison of the Results..70
4.4 Conclusions..73
4.5 Acknowledgments..75
References..75
CHAPTER 5..79
CAPTURE OF HYPERTHERMAL CO_2 BY AMORPHOUS WATER ICE VIA MOLECULAR EMBEDDING..79
5.1 Introduction..80
5.2 Experimental..81
5.3 Results and Discussion..83
A. Embedding: Ice Structure and Composition..83
B. Kinetics and Dynamics of CO2 Embedding in Ice..86
C. Embedding as an Activated Process..90
5.4 Conclusions..94
References..96
CHAPTER 6..101
REVERSE WATER-GAS SHIFT REACTION IN SUPERSONIC NOZZLE WITH CATALYTIC METAL SURFACE..101
6.1 Introduction..101
6.2 Experimental..102
A. Molecular Beam Source..102
B. RWGS Reaction Yield Calculation..103
6.3 Results and Discussion..106

A. Yield of the reaction 106
B. Thermodynamics and Reaction Mechanism 112
6.4 Conclusions 119
References 120
APPENDIX 123
Supplementary Figures 123

LIST OF FIGURES

2.1 Schematics of experimental apparatus 8
2.2 Infrared radiation reflecting from a substrate at incident angles (θ) 12
2.3 Energy level diagram of an ejected photoelectron 14
3.1 Absorption bands of oPE-SAM on polycrystalline gold substrates 25
3.2 Scanning tunneling microscopy images of the pristine oPE-SAM 26
3.3 RAIRS spectra of monolayer before and after $O(^3P)$ exposure 28
3.4 Proposed mechanism for $O(^3P)$ reaction with oPE-SAM 31
3.5 STM spectra of monolayer before and after $O(^3P)$ exposure 32
3.6 Plotting the log of remaining unreacted oPE versus total $O(^3P)$ exposure 35
4.1 Example TPD spectra for CF_4 and Xe 53
4.2 Uptake rates for CF_4 and Xe on ASW as a function of incident energy 56
4.3 TPD spectra for 5.11 eV Xe as a function of exposure 57
4.4 Comparison of TPD spectra for CF_4 with different exposures 58
4.5 TPD spectra of capping experiments for Xe 60
4.6 TPD spectra of capping experiments for CF_4 61
4.7 TPD spectra of co-deposition of SF_6 and water 64
4.8 TPD spectra for exposures at different θ 66
4.9 RAIRS spectra of deposition of 5.3 eV CF_4 into ASW ice 67
4.10 Langmuir isotherm fit to the FTIR data of CF_4 saturation experiments 69
4.11 Energy dependence of embedding rate 71
4.12 Summary for the rare gases Kr and Xe from TPD experiments 72
5.1 Example chronological spectra obtained by exposing an ASW film to CO_2 84
5.2 RAIRS spectra of co-deposition of CO_2 and water 88
5.3 Initial embedding probabilities on ASW for three different average CO_2 energies 89
5.4 polynomial nonlinear least-squares fit to the initial CO_2 embedding probability 91
5.5 Embedding probability against the incident translational momentum 93
6.1 Gas intensity dependence with stagnation pressure 104
6.2 TOF beam profile of RWGS reaction 107
6.3 Corrected CO intensity 109
6.4 Intensity dependence of gas CO, CO_2 and H_2O at different temperatures 110

6.5 Dependence of yield with nozzle temperature at various pressures 111

6.6 Plot of lnK as a function of $({}^{1}/_{T})$ 114

6.7 Dependence of yield with nozzle temperature with different P_{CO_2}/P_{H_2}ratios 115

6.8 Dependence of yield with nozzle stagnation pressure at nozzle temperature 600 ℃ 116

A.1 RAIR spectra of oPE monolayer versus O(^{3}P) exposure 124

A.2 RAIR spectra of energetic ballistic deposition of 4.1eV CF4 into ASW ice 125

A.3 RAIR spectra of energetic ballistic deposition of 3.7eV CF4 into ASW ice 126

A.4 RAIR spectra of energetic ballistic deposition of 4.7eV CF4 into ASW ice 127

A.5 RAIR spectra of exposure of 3.0eV CO_2 into ASW ice 128

A.6 RAIR spectra of energetic of 4.2eV CO_2 into ASW ice 129

A.7 RAIR spectra of energetic of 4.0eV CO_2 into ASW ice 130

A.8 RAIR spectra of energetic of 3.7eV CO_2 into ASW ice 131

A.9 RAIR spectra of energetic of 3.7eV CO_2 into ASW ice 132

A.10 RAIR spectra of energetic of 3.4eV CO_2 into ASW ice 133

A.11 TOF spectra of 10% CO_2 in H_2 gas mixtures at pressure 400 psi, temperature 550 ℃ 134

A.12 TOF spectra of 10% CO_2 in H_2 gas mixtures at pressure 500 psi, temperature 550 ℃ 135

A.13 TOF spectra of 10% CO_2 in H_2 gas mixtures at pressure 600 psi, temperature 550 ℃ 136

A.14 TOF spectra of 10% CO_2 in H_2 gas mixtures at pressure 700 psi, temperature 550 ℃ 137

A.15 TOF spectra of 10% CO_2 in H_2 gas mixtures at pressure 400 psi, temperature 600 ℃ 138

A.16 TOF spectra of 10% CO_2 in H_2 gas mixtures at pressure 500 psi, temperature 600 ℃ 139

A.17 TOF spectra of 10% CO_2 in H_2 gas mixtures at pressure 600 psi, temperature 600 ℃ 140

A.18 TOF spectra of 10% CO_2 in H_2 gas mixtures at pressure 700 psi, temperature 600 ℃ 141

A.19 TOF spectra of 10% CO_2 in H_2 gas mixtures at pressure 400 psi, temperature 650 ℃ 142

A.20 TOF spectra of 10% CO_2 in H_2 gas mixtures at pressure 500 psi, temperature 650 ℃ 143

A.21 TOF spectra of 10% CO_2 in H_2 gas mixtures at pressure 600 psi, temperature 650 ℃ 144

A.22 TOF spectra of 10% CO_2 in H_2 gas mixtures at pressure 700 psi, temperature 650 ℃ 145

A.23 TOF spectra of 10% CO_2 in H_2 gas mixtures at pressure 400 psi, temperature 700 ℃ 146

A.24 TOF spectra of 10% CO_2 in H_2 gas mixtures at pressure 500 psi, temperature 700 ℃ 147

A.25 TOF spectra of 10% CO_2 in H_2 gas mixtures at pressure 600 psi, temperature 700 ℃ 148

A.26 TOF spectra of 10% CO_2 in H_2 gas mixtures at pressure 700 psi, temperature 700 ℃ 149

A.27 SQW spectra of 1% CO_2 in H_2 gas mixtures at pressure 400 psi, temperature 550 ℃.. 150
A.28 SQW spectra of 1% CO_2 in H_2 gas mixtures at pressure 500 psi, temperature 550 ℃.. 151
A.29 SQW spectra of 1% CO_2 in H_2 gas mixtures at pressure 400 psi, temperature 600 ℃.. 152
A.30 SQW spectra of 1% CO_2 in H_2 gas mixtures at pressure 500 psi, temperature 600 ℃.. 153
A.31 SQW spectra of 1% CO_2 in H_2 gas mixtures at pressure 400 psi, temperature 650 ℃.. 154
A.32 SQW spectra of 1% CO_2 in H_2 gas mixtures at pressure 500 psi, temperature 650 ℃.. 155

ACKNOWLEDGEMENTS

Above all, I would like to express my sincerest gratitude and appreciation to my advisor and mentor, Professor Steven Sibener, for his invaluable guidance and support throughout my graduate studies. He was always there to listen to the little problems and give us advice when we had research hardships. His innumerable mentor moments and insights on the working of academic research were essential to the completion of this dissertation. I am indebted to him for all his inspiration which enriched my growth as a student, and all his caring which made me feel at home when studying abroad. He is more than a mentor, but a family member to me. I also thank the other members of my thesis committee, Professor Laurie Butler and Professor Greg Engel, for their time and helpful discussions.

I have been fortunate to work with so many brilliant and helpful chemists in the Sibener group. Specifically, I would like to thank former members Hanqiu Yuan and Ryan Brown for training me on the apparatus during my first year. I truly appreciate Kevin Gibson who gives a lot of help and advice over all the years. I was extraordinarily fortunate to have Grant Langlois as my coworker, he is brilliant, responsible and helpful. Thanks to Grant for developing such a great friendship, and having countless insightful discussions in the lab. I also very much appreciate the help from Natalie Kautz. She generously helped us on scanning tunneling microscopy with our samples, and offered a lot of suggestions with our research project. Other group members, new and old, have provided a very friendly environment; I thank Hyung Ju Ryu, Bryan Wiggins, Zack Hund, Kevin Nihill, Jon Raybin, Darren Veit, Jeff Sayler and Ross Edel. To Becca Thompson, it

is unfortunate that we haven't had a lot of opportunities to work together. But it's so great to have a smart person like you take over my project, and best luck on your candidacy exam.

The research described in this thesis relies heavily on the support from departmental facility staff members. I thank Helmut Krebs for helping us with our machining needs, and Qiti Guo for his help with the equipment. I also thank Melinda Moore, Vera Dragisich, Maria Jimenez, John Phillips, Zena Anderson, Tanya Hagerman for their assistance of miscellaneous matters. I'd like to express my sorrow at the loss of Dave Smith and Gerard Jendraszkiewicz, who helped us to fix our electronics, and left a lot of great memories with us.

Support from friends both within and outside of the department is crucial throughout graduate school. I want to extend thanks to all my friends who helped fill my Ph.D. years with many fond memories. I especially want to thank Lei Wang, who is my very close friend, for sharing laughter and tears with me over the years. I thank all the other students in the 2010 unprecedently big class: Ge Feng, Ying Zhao, Li Wang, Nian Liu, Hao Zhang, Junjie Zhai, Tianyue Zheng, Zhiyou Deng, Xiao Wang and Wei Qin, Yunjie Chen, Bobo Dang, Haibin Zheng, Yichen Yu, and Luyao Lu. They made my grad school experience more enjoyable.

Finally, but most importantly, I would like to thank my husband, Yuxing Peng, for being beside me, supporting me, and taking care of me for more than 10 years. I'd like to quote a line of a poem by Robert Browning, to my dearest love and friend: "Grow old along with me, the best is yet to be".

ABSTRACT

The study of gas-surface interaction reactivity and dynamics is important both for developing fundamental knowledge and for aiding the development of various applications. Thorough understanding of interactions of gases with ice and organic films can help answer important questions related to geophysics and global energy issues. Additionally, experimental measurements of these processes can be used to validate advanced computer models. The experiments in this thesis have been carried out under well-defined conditions, namely in ultrahigh vacuum and using highly-ordered surfaces and molecular beams.

This thesis mainly focused on two kinds of interactions: atomic oxygen with organic thin films, and gaseous species with ice surfaces. The first aspect investigated the kinetics and dynamics of bimolecular reactions utilizing a supersonic beam of atomic oxygen and self-assembled monolayers (SAMs). With a combination of in situ infrared spectroscopy and scanning tunneling microscopy, the mechanism of the reaction of $O(^3P)$ with phenyl-substituted alkynes has been characterized and confirmed. This technique has the potential to elucidate orientation-dependent kinetics, with the added ability to "collisionally stabilize" reactive intermediates.

Here, we demonstrate a new mechanism of energetic ballistic deposition, to trap and concentrate gases into ice at a surface temperature where gases adsorption is infeasible. The embedding of CO_2, CF_4 and other small atoms and molecules into ice has been characterized. The results show that the ice composition can be modified by a gas with high translational energies. These findings have implications for many fields including environmental science, astrophysics, and astrochemistry.

This thesis also includes a finding of reverse water-gas shift (RWGS) reaction in our supersonic nozzle with catalytic metal surface. Utilizing a supersonic expansion beam technique, we demonstrate highly selective reactivity between carbon dioxide and molecular hydrogen involved in the RWGS reaction. This reaction exhibits reaction yields as high as 90% at nozzle temperatures approaching 750 ℃. The metal surface was found to serve as a heterogeneous catalyst for the reaction. This supersonic expansion technique provides opportunities to screen various catalytic reactions under high temperature and high pressure conditions. Thus, it is feasible for this technique to facilitate such reactions with surface-generated gas-phase radicals, followed by rapid desorption and cooling of the intermediate products.

CHAPTER 1
INTRODUCTION

1.1Motivation

The study of gas-surface interactions is important in numerous natural and industrial processes, such as combustion, atmospheric, and materials chemistry. The information obtained from investigation of such interaction dynamics is therefore crucial for both fundamental knowledge discovery and various applications, such as sputtering, plasma etching and heterogeneous catalysis. Elementary steps in the interactions, such as chemical reactions, adsorption and scattering are prototypical of more complex processes and better understanding of them deepens our knowledge of such processes. Hence the experiments in this thesis have been carried out under well-defined condition, namely in ultrahigh vacuum, and utilizing supersonic expansion molecular beam to explore gas-surface interactions. The thesis is primarily focused on understanding the interaction of atomic oxygen $O(^3P)$ and volatile gas species with ice and self-assembled monolayer via supersonic molecular beam technique.

The interaction of atomic and molecular species with water and ice is of fundamental importance to numerous scientific disciplines. In interstellar space, the collisions of icy surfaces and other species can lead to the chemical modification of the interior of the ice.[1-4] Energetic collisions on ice surfaces are also highly relevant for the evolution of the composition of icy bodies in space.[5-7] When energetic molecules collide with ice surface, the energy exchange from the impact of the incident species with the ice can lead to several possible outcomes. An atom or molecule can adsorbed to the ice, be buried, or absorbed into the ice surface. But these processes typically require either additional condensate or low temperatures (<100 K).[6,8] Thus, a direct approach to inject the gas-phase species directly into the ice would improve understanding of how species can be trapped into ice, which have significance in atmospheric processes.[9,10]

In our previous studies, we found a new mechanism of trapping neutral xenon with non-porous amorphous or crystalline ice surfaces by energetic ballistic deposition.[11,12] Transnationally energetic xenon atoms can penetrate the ice surface and become stably embedded within the ice above the xenon desorption temperature. Because of the widespread interest in the interactions of gas species with ice, I expanded on our previous work and examine how small molecules can be implanted in ice surfaces and further study the nature of the absorption sites. More background will be introduced in the following chapters of this thesis.

Studies of gas-surface collisional energy exchange between atomic oxygen with hydrocarbons have been studied extensively due to their essential role in many important chemistry fields, such as combustion, atmospheric chemistry.[13-19] Studies of material degradation and durability under atomic oxygen attack have been performed in decades, especially for advanced aircraft and spacecraft flight in the low earth orbit environment (LEO).[20-23] To better quantify the kinetics and dynamics of such reactions, we developed a methodology utilizing self-assembled monolayers (SAMs) to establish some degree of control over the intended pathways. Because SAMs have the ability to spontaneously form well-ordered structures, the control of the orientation and packing of the chemical functional groups on the surface can be used to tune the physical properties.[24] The use of a SAM surface as an ensemble of reactants is also advantageous due to its ability to rapidly dissipate excess energy.[25-27] These surfaces provide us opportunities to probe the mechanisms of reactions at interfaces, and are thus of importance to many fields of endeavor.

1.2 Organization of this thesis

This thesis could be divided into four parts. In Chapter 3, the reaction mechanism and kinetics of a self-assembled monolayer thin film with O(^{3}P) are investigated. In order to study the kinetics and dynamics of bimolecular reaction, we developed a methodology to establish some degree of steredynamic control by dosing reactive species onto the surface of a self-assembled monolayer (SAM). The chemical and structural changes in an oligo(phenylene ethynylene) SAM reaction with O(^{3}P) was monitored by time-resolved reflection-absoption infrared spectroscopy (RAIRS) and scanning tunneling microscopy (STM) under ultrahigh vacuum conditions. We have confirmed electrophilic addition of O(^{3}P) onto the alkyne moieties, resulting in formation of a ketene intermediate via phenyl migration. Moreover, we have observed that the phenyl ring at the vacuum/film interface significantly cants toward the substrate plane as a result of this reaction. This approach of using preoriented reactive molecules in ordered SAMs in combination with angle- and velocity-selected energetic reagents provides a general approach for probing geometric constraints associated with reaction dynamics for a wide range of chemical reactions.

In next part, Chapter 4, the interaction of atomic and molecular species with water and ice is investigated. We explored embedding, absorption process of inert molecular species in the near surface region of ice surfaces. Amorphous solid water (ASW) films were exposed to high-energy CF_4 ($\geq$3 eV) molecules, resulting in the embedding into ice. This embedding was quantified using infrared spectroscopy. The initial adsorption rate is strongly activated by translational energy. The uptake rate for CF_4 is much less than for Xe at the same incident energy, given they have similar van der Waals radii. This indicates that the momentum is the key factor in determining whether the incident atom or molecule can embed into ice. Move massive SF_6 molecule was also investigated, which cannot stably embed in the ice due to its larger van der Waals radius. These observations establish a new channel by which incident species can be trapped under conditions where they would not be bound stably as surface adsorbates.

In Chapter 5, the uptake of CO_2 by water ice was studied with energetic ballistic embedding. Carbon dioxide (CO_2) has been played a fundamental role in earth's geophysics. It is also present in interstellar and circumstellar ice mantles. ASW is the most abundant phase of water in interstellar clouds. To understand interactions between ice and CO_2, we investigated the embedding and trapping behavior of CO_2 molecules into ASW with RAIRS. We demonstrated that CO_2 molecules can be injected and trapped into ASW at temperatures above CO_2 adsorbed on the ice surface (85K). The CO_2 are embedded under ice surface rather than burial or adsorption. In FTIR spectra, the ν3 stretching modes near 2341 cm^{-1} and 2361 cm^{-1} together suggest a crystalline nature of CO_2. The embedding probability of CO_2 is on the order of 10^{-6}, which is much smaller than other projectiles we have studied, including Xe and CF_4. The morphology of ice surface also determines the CO_2 uptake into ice, as no CO_2 was observed embedded into CI even though CI and ASW has similar density at temperature 125K. This finding may be considered as a route to trap CO_2 into icy surface in interstellar space, which can lead to molecular complexification.

In the last chapter, a highly selective reverse water-gas shift (RWGS) reaction using supersonic expansion nozzle will be discussed. The RWGS reaction is an important industrial reaction, but the conversion is often companioned with formation of other hydrocarbons, and the conversion rate is less than 50%. Here we reported a high-temperature, short-contact-time supersonic nozzle made with stainless steel to facilitate the RWGS reaction. This highly selective reaction could reach a yield of CO as high as 90% at temperature 750 ℃. The products are CO and H_2O only, no other hydrocarbons were observed. The relationships between reaction yield and temperature, stagnation pressure, and number density ratio were also investigated. The mechanism of the chemical process is shortly discussed.

References

1. Strazzulla, G.; Leto, G.; Gomis, O.; and Satorre, M. A. *Icarus*, **2003**, 164, 163
2. Gomis, O.; Satorre, M. A.; Strazzulla, G.; Leto, G. *Planet. Space Sci*., **2004 ,** 52, 371
3. Strazzulla, G.; Baratta, G. A.; Leto, G.; Gomis, O. *Icarus*, **2007,** 192, 623
4. Strazzulla, G. *Methods Phys. Res. B*, **2011,** 269, 842
5. A'Hearn, M. F.; Feaga, L. M.; Keller, H. U.; Kawakita, H.; Hampton, D. L.; Kissel, J.; Klaasen, K. P.; McFadden, L. A.; Meech, K. J.; Schultz, P. H.; Sunshine, J. M.; Thomas, P. C.; Veverka, J.; Yeomans, D. K.; Besse, S.; Bodewits, D.; Farnham, T. L.; Groussin, O.; Kelley, M. S.; Lisse, C. M.; Merlin, F.; Protopapa, S.; Wellnitz, D. D. *Astrophys. J*., **2012,** 758, 1
6. Notesco, G.; Bar-Nun, A.; Owen, T. *Icarus*, **2003,** 162, 183
7. Owen T.; Bar-Nun, A. *Icarus*, **1995,** 116, 215
8. Iro, N.; Gautier, D.; Hersant, F.; Bockelee-Morvan, D.; Lunine, J.I. *Icarus*, **2003,** 161, 511
9. Toon, O. B.; Turco, R. P.; Jordan, J.; Goodman, J.; Ferry, G. *J. Geophys. Res*, **1989,** 94, 11359
10. Turco, R. P.; Toon, O. B.; Hamill, P. *J. Geophys. Res., [Atmos.]* **1989,** 94, 16493
11. Killelea, D. R.; Gibson, K. D.; Yuan, H.; Becker, J. S.; Sibener, S. J. *J. Chem. Phys*., **2012,** 136, 144705
12. Gibson, K. D.; Killelea, D. R.; Becker, J. S.; H. Yuan; Sibener, S. J. *Chem. Phys. Lett*., **2012,** 531, 18

13. Andresen, P.; Luntz, A. C. *J. Chem. Phys.*, **1980,** 72, 5842

14. Luntz, A. C. *J. Chem. Phys.*, **1980,** 73, 1143

15. Luntz, A. C.; Andresen, P. *J. Chem. Phys.*, **1980,** 72, 5851

16. Ausfelder, F.; McKendrick, K. G. *Prog. React. Kinet. Mech.*, **2000,** 25, 299

17. Zhang, J. M.; Garton, D. J.; Minton, T. K. *J. Chem. Phys.*, **2002,** 117, 6239

18. Wagner, A. J.; Wolfe, G. M.; Fairbrother, D. H. *J. Chem. Phys.*, **2004,** 120, 3799

19. Paz, Y.; Trakhtenberg, S.; Naaman, R. *J. Phys. Chem.* **1994,** 98, 13517

20. Leger, L. J. Oxygen Atom Reaction with Shuttle Materials at Orbital Altitudes (NASA, Lyndon B. Johnson Space Center, 1982)

21. Leger, L. J.; Visentine, J. T. *J Spacecraft,* **1986,** 23, 505

22. Haruvy, Y. *ESA Journal,* **1990,** 14, 109

23. Murr, L. E.; Kinard, W. H. *American Scientist,* **1993,** 81, 153

24. Gleiche, M.; Chi, L. F.; Fuchs, H. *Nature,* **2000,** 403, 173

25. Gibson, K. D.; Isa, N.; Sibener, S. J. *J. Chem. Phys.*, **2003,** 119, 13083

26. Lu, J. W.; Day, B. S.; Fiegland, L. R.; Davis, E. D.; Alexander, W. A.; Troya, D.; Morris, J. R. *Prog. Surf. Sci.*, **2012,** 87, 221

27. Isa, N.; Gibson, K. D.; Yan, T.; Hase, W. L.; Sibener, S. J. *J. Chem. Phys.*, **2003,** 120, 2417

CHAPTER 2

EXPERIMENTAL SETUP AND TECHNIQUES

The experimental studies were performed under well controlled ultra-high vacuum (UHV) conditions. The instrument consists of a molecular beam source and an UHV surface analysis chamber (base pressure 10^{-9} Torr), connected to each other through a gate valve. A schematic is shown in Figure 2.1. The surface processes were characterized in situ by the analytical techniques available on the UHV chamber, the beam was characterized using time-of-flight techniques. The remainder of this chapter describes the layout of the molecular beam source and surface analysis chamber. Modifications to the system and sample preparation procedures are described in detail in subsequent chapters.

2.1 The Molecular Beam Source

The supersonic molecular beamline consisted of a beam source chamber and two stages of differential pumping. The beam is produced by supersonic expansion of gas through a pinhole mounted in a nozzle holder machined from a VCR ¼" blank gland. The gas expands into a source chamber pumped by a 10 inch, 4000 L/sec diffusion pump, backed by a Pfeiffer blower and a Pfeiffer rotary vane pump (typical operating pressure ~ 10^{-6} torr). The expansion is skimmed by a nickel skimmer (Gentry) with a 0.5 mm aperture, which is mounted on a movable platform. The skimmed beam then passes into a second chamber pumped by a 4 inch, 850 L/sec diffusion pump equipped with a Mexican hat cold cap to reduce back streaming (typical operating pressure ~ 10^{-7} torr). This chamber contains a variable speed mechanical chopper and an infrared LED combined with a photodiode operational amplifier detector (United Detector Technologies) to provide the signal trigger from the chopper. It also contains a solenoid operated beam flag positioned in front

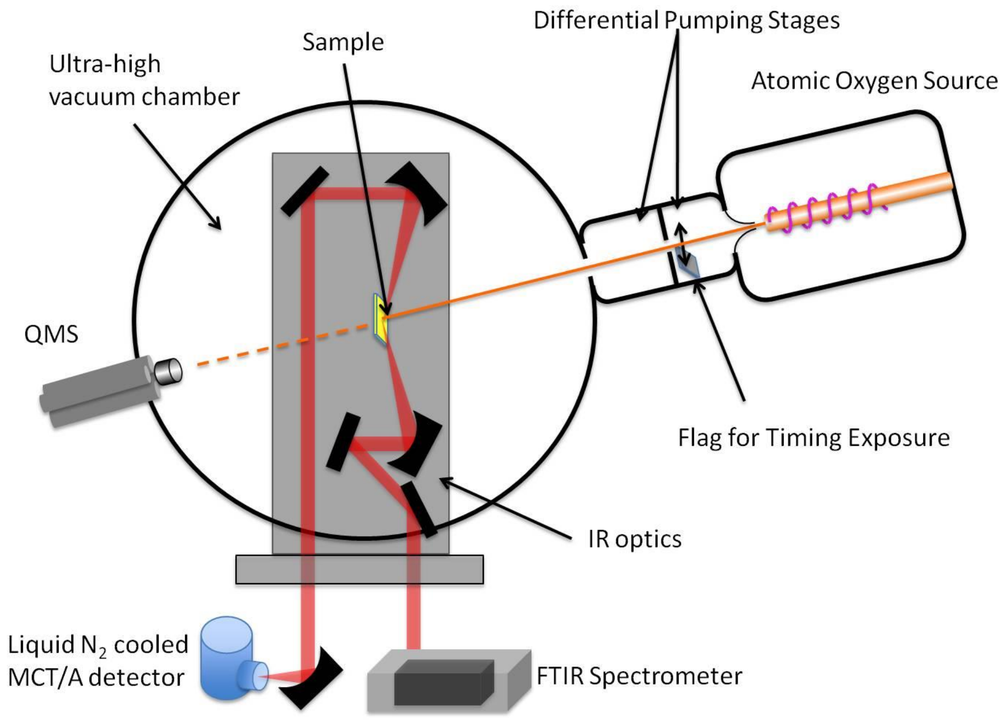

Figure 2.1. Schematics of experimental apparatus. UHV scattering chamber with a single molecular beam and RAIRS detection.

of the exit aperture. The molecular beam leaves the second chamber through a 0.135 inch collimating aperture, and enters a third differentially pumped region. The latter is pumped by a 240 L/sec turbo molecular pump, which is backed by the second differentially pumped chamber (typical operating pressure ~ 10^{-8} torr). The beam then leaves this third region through a 0.089 inch final collimating aperture and passes through a bellow and a gate valve before entering the main scattering chamber.

The nozzle to skimmer distance was typically 7 mm. The skimmer to chopper distance was 12.7 cm, the chopper to the first collimating aperture (3.43 mm in diameter) was 10.7 cm, and the distance from the first to the second collimating aperture (2.26 mm in diameter) was 24.1 cm. The distance from the final collimating aperture to the sample was 43.8 cm. The total distance from the chopper to the detector was 116.2 ± 1 cm.

2.2 Ultra-high Vacuum (UHV) Surface Analysis Chamber

The experiments in this thesis were conducted in the two-level Ultra-high Vacuum (UHV) Surface Analysis Chamber. The base pressure of the chamber after a standard bake-out procedure is typically ~10^{-10} torr as measured by a Bayard-Alpert nude ion gauge. The lower level of the UHV chamber houses part of an Infrared Reflection-Absorption Spectrometer (IRRAS) setup. It is also equipped with a number of ports for attachment of other equipment.

The upper level of the chamber contains various surface analysis and preparation tools including quadrupole mass spectrometer (QMS), low energy electron diffraction (LEED), Auger spectroscopy, an ion gun for sample preparation, an X-ray gun, and a cylindrical mirror analyzer (CMA).

The sample is clamped to a block of molybdenum with two tantalum tabs fitted into grooves that were spark cut into the side of the sample. The molybdenum block was connected to a liquid nitrogen reservoir through a flexible copper braid, which served to cool the sample. Heating of the sample was achieved by radiative heating of the back of the substrate for temperatures below 400 K, or by electron bombardment of the back of the substrate (resistive heating) for higher temperatures, with the filament used for electron bombardment, in combination with liquid nitrogen cooling. Temperatures were measured with a type K thermocouple spot welded to the side of the sample and clamped below the latter, and could be controlled to within 0.1 K with a Eurotherm temperature controller. The manipulator itself was mounted on a rotating lid, equipped with three spring-loaded Teflon seals differentially-pumped to 5×10^{-11} torr. It was mounted two inches off-center on the lid, to allow the sample to be positioned in front of the various surface diagnostics in the upper chamber. It could also be lowered into the lower chamber at the focal point of RAIRS in order to position the sample for spectroscopy as well as molecular beam dosing or irradiation.

2.3 Reflection-Absorption Infrared Spectroscopy (RAIRS)

To characterize the surface, we choose to use reflection-absorption infrared spectroscopy (RAIRS) because RAIRS provides us with a non-destructive, real time analysis, and information about the orientation of absorbed molecules on the surfaces.[1,3] The basic principles of RAIRS are very similar to traditional FTIR transmission spectroscopy experiments. Infrared radiation is directed toward a sample and photons from the radiation excite vibrations within the sample molecules. Then the interferogram is converted into a spectrum by a Fourier transform within the spectrometer’s electronics. The resulting spectrum is a plot of intensity versus wavenumber. The main difference between RAIRS and transmission spectroscopy is that RAIRs obey a set of surface selection rules, first described by Greenler.[1,2]

Figure 2.2 is a schematic demonstrating the findings of Greenler. A beam of infrared radiation that is reflective off a planar substrate can be resolved into two components: perpendicular (s-polarized) and parallel (p-polarized) to the plane of incidence. When light that is polarized perpendicular to the incident plane (E_s) is reflected off a planar substrate, the reflected light undergoes a phase shift close to 180º at all angles of incidence (θ). The phase shift causes destructive interference, which almost completely cancels out the component that is perpendicular to the plane of incidence directly at the surface. Therefore, s-polarized light has very little interaction with dipole moments of molecules absorbed on the reflective interface. In contrast, light that is polarized parallel to the plane of incidence (E_p) undergoes a phase shift at the interface that increases rapidly as the incident angle approaches grazing angles. Greenler determined that p-polarized light reflected from a substrate at an incident angle between 80 ºto 85 ºwould have a ~90 º phase shift. A phase shift near 90 ºresults in a net doubling of the p-polarized light's amplitude at the reflective surface, and therefore, p-polarized light will interact significantly with dipoles of molecules absorbed at the interface. Greenler's findings can be summarized by a surface selection rule that states: only surface bound molecules with active IR modes that have a component of their transition dipole moment perpendicular to the surface will be observable in IRRAS measurements. With these selection rules, we are able to obtain the information of orientation and chemical environment of absorbed molecules.

In this thesis, in situ IRRAS measurements were performed with a Thermofisher Nicolet 6700 infrared spectrometer. Infrared radiation from a SiC globar source was reflected off a gold coated parabolic mirror (focal length 180 mm) and focused through an aperture (0.9 mm - 4 mm)

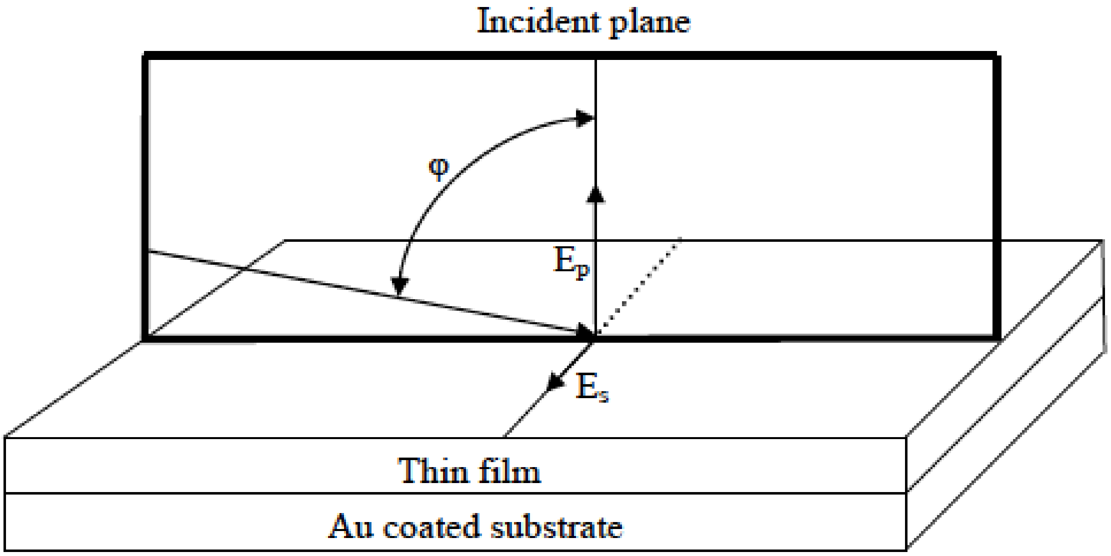

Figure 2.2. Infrared radiation reflecting from a substrate at incident angles (φ) near grazing can be resolved into two components: perpendicular to the plane of incidence (E_s) and parallel to the plane of incidence (E_p)

on a variable aperture wheel. The IR beam was then sent through an interferometer and focused onto a movable mirror. The moveable mirror allowed the IR radiation to be sent to either an internal sample compartment or an external sample compartment. In the external sample compartment, the IR light was focused by a parabolic mirror (focal length 250 nm) through a ZnSe window attached to the UHV chamber previously described. The IR radiation was reflected off the sample in the UHV chamber at ~ 75 ° relative to the surface normal. After reflecting off the surface, the IR radiation exited the UHV chamber through a KBr window and was focused by a parabolic mirror (focal length 250 mm), reflected from a flat mirror, and finally focused by a second parabolic mirror (focal length 43 mm) into a mid-range (750–4000 cm^{-1}) mercury cadmium telluride (MCT) detector, which was cooled with liquid nitrogen. The spectrometer also has the option to collect spectra from samples within the internal sample compartment.

2.4 X-ray Photoelectron Spectroscopy (XPS)

X-ray photoelectron spectroscopy (XPS) is well established to determine the chemical identity and local chemical environment of elements on substrates. XPS relies on the photoelectric effect described by Einstein in 1905.[4] The photoelectric effect describes the phenomenon of core level electrons being ejected form a surface when exposed to photons of sufficient energy. The samples are irradiated with photons with energies in the range of 200-2000eV, which have sufficient energy to eject core level electrons from a sample. An energy analyzer is used to determine the kinetic energy of the ejected electrons. As shown in figure 2.3, the kinetic energy of ejected electrons is related to the energy of the exciting photon (hν), binding energy of the core electron (E_b), and the minimum energy needed to remove an electron form a solid to a point immediately outside the solid surface (Φ)with equation:

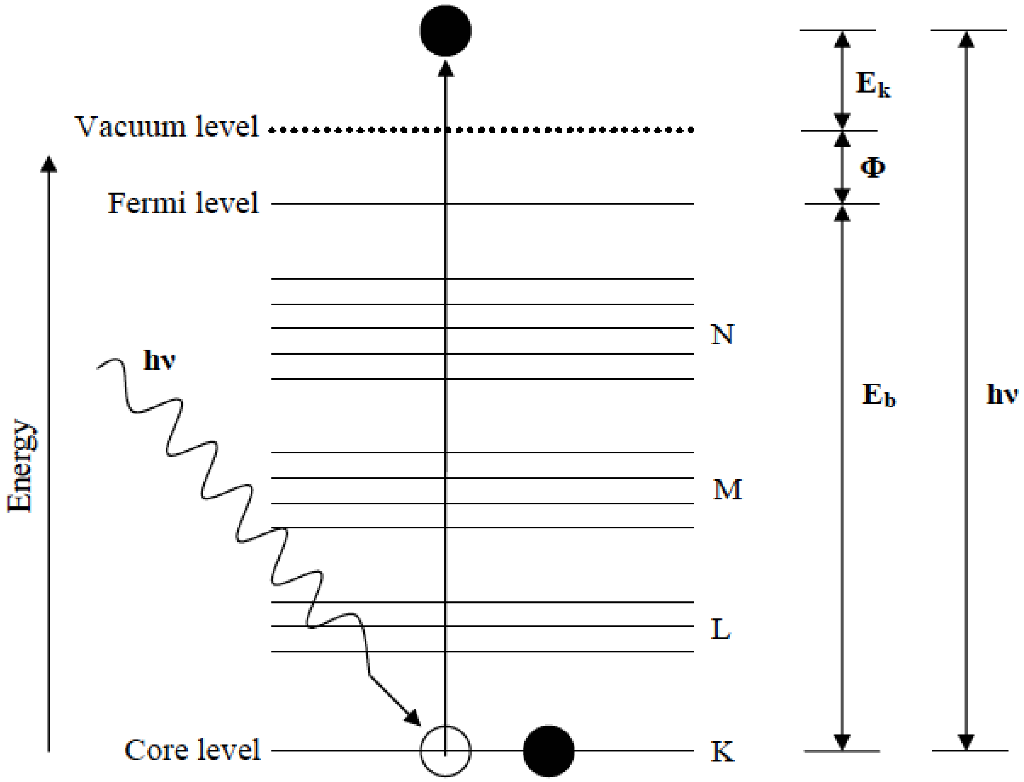

Figure 2.3. Energy level diagram of an ejected photoelectron. E_k is the kinetic energy of the ejected photoelectron, E_b is the binding energy of the electron, and Φ is the work function of the instrument.

$$\mathrm{E_k = h\nu - E_b - \Phi} \tag{2-1}$$

The chemical identity can be determined by the binding energy of ejected electron. In our project, we use XPS to quantitatively measure the percentage of C, S, O. We observe C(1s), S(2p), O(1s) peaks, whose positions are around 284.6 eV, 162.0 eV and 531.6 eV respectively.

In the research presented in this thesis, achromatic Al Kα (1486.6 eV) radiation was generated from a SPECS X-ray source operating at 300 W (10 kV and 30 mA). Ejected photoelectrons were detected by a cylindrical mirror analyzer (CMA) (Physical Electronic, 15-250) operating with pass energies between 50–100 eV. Survey spectra were collected with a step size of 10 eV, and high resolution spectra were collected with a step size of 0.1 eV. The binding energies for all spectra are referenced to the Au(4f 7/2) peak at 83.8 eV.

2.5 Time-of-Flight (TOF) Techniques

In this thesis, we use TOF to measure the velocity/energy distributions of particles in beam. The data obtained from TOF measurements are the distribution of flight times in a given beam at a specific scattering condition. These spectra are obtained by utilizing the four slot chopping pattern on the chopper wheel, which consists of 4 slits (0.02" width) having a 1% duty cycle. The observed flight time can be used to determine energy distribution of the beam, with followed calculation.

For an expanded beam, what we measure is the number of density distribution $n(t)$ in time domain. Thus transformation between velocity/energy distributions and TOF distributions is important. Here we consider the transformation from number of density distribution in time domain to energy distribution in flux for a TOF experiment. The particle velocity can be expressed in terms of v, given that the flight time can be related to the velocity and total flight path:

$$v = \frac{L}{t} \tag{2-2}$$

Where v is the speed of the particle, from the measurement of the time t, with L being the chopper-to-ionizer flight path, which is 116.2 cm with our apparatus. The distribution $n(t)$ will thus be given by:

$$n(t)dt = n\left(\frac{L}{t}\right)dv(t) = -\frac{L}{t^2}n(v)dt \tag{2-3}$$

$n(v)dv$ or $n\left(\frac{L}{t}\right)dv$ represent the number of particles that cross a unit area per unit time with velocities in the range (v, v +d v). Generally, the minus sign is disregarded in plotting distributions, and normalization constants could also be dropped for simplicity, as eq 2-4:

$$n(t) \sim \frac{1}{t^2}n(v) \tag{2-4}$$

Next, we convert from $n(t)$ to energy distribution in time domain. The energy and velocity have relation:

$$\mathrm{E} \propto v^2 \tag{2-5}$$

$$\mathrm{dE} \sim v dv \sim \frac{1}{t}dv \tag{2-6}$$

$$\mathrm{n}(v) \sim \frac{dE}{dv}n(E) \sim \frac{1}{t}n(E) \tag{2-7}$$

$$n(t) \sim \frac{1}{t^2}n(v) \sim \frac{1}{\mathrm{t}^3}n(E) \tag{2-8}$$

From equation 2-5 to 2-8, we convert time distribution to energy distribution in time domain. Last, we convert from time domain $n(E)$ to flux domain $\Phi(E)$. The flux and number of density have:

$$n(E) = \Phi(E) \bullet v = \frac{\Phi(E) \bullet L}{t} \sim \frac{1}{t}\Phi(E) \tag{2-9}$$

$$n(t) \sim \frac{1}{\mathrm{t}^3}n(E) \sim \frac{1}{t^4}\Phi(E) \tag{2-10}$$

With equations discussed above, we could invert measured TOF distributions to obtain the desired velocity/energy distributions.

References

1. Greenler, R. G. *J. Chem. Phys.,* **1966,** 44, 310
2. Greenler, R. G. *J. Chem. Phys.*, **1969,** 50, 1963
3. Trenary, M. *Ann. Rev. Phys. Chem.*, **2000,** 51, 381
4. Einstein, A. *Annalen der physic*, **1905,** 17, 132

CHAPTER 3

FORMATION OF STABILIZED KETENE INTERMEDIATES IN THE REACTION OF O(^{3}P) WITH OLIGO(PHENYLENE ETHYNYLENE) THIOLATE SELF-ASSEMBLED MONOLAYERS ON AU(111)

The data presented in this chapter was previously published in the Journal of Physical Chemistry C. The following content was reprinted with permission from [Wenxin Li, Grant G. Langlois, Natalie A. Kautz, and S. J. Sibener, "Formation of Stabilized Ketene Intermediates in the Reaction of O(^{3}P) with Oligo(phenylene ethynylene) Thiolate Self-Assembled Monolayers on Au(111)" J. Phys. Chem. C, DOI 10.1021/jp504466r (2014).] Copyright 2014, American Chemical Society.

We have taken steps to develop a methodology for observing and trapping organic reaction intermediates by exposing well-ordered self-assembled monolayers to supersonic beams of atomic oxygen. The use of a SAM stabilizes highly energetic intermediates formed from bimolecular reactions at the interface due to rapid thermal equilibration with the SAM matrix. In this paper we will discuss the elucidation of the mechanistic details for the fundamental reaction between O(^{3}P) and phenyl-substituted alkyne bonds by monitoring chemical and structural changes in an oligo(phenylene ethynylene) SAM reacting with O(^{3}P) under collision conditions having specified initial reaction orientation. Utilizing time-resolved reflection-absorption infrared spectroscopy (RAIRS) and scanning tunneling microscopy (STM) under ultrahigh vacuum conditions, we have directly observed electrophilic addition of O(^{3}P) onto the alkyne moieties, resulting in formation of a ketene intermediate via phenyl migration. Under single-collision conditions in the gas phase the vibrationally-excited ketene intermediate cleaves to release CO. In contrast to this, herein we have directly observed the formation of the condensed-phase stabilized singlet ketene by RAIRS. Moreover, we have observed that the phenyl ring at the vacuum/film interface significantly cants towards the substrate plane as a result of this reaction. STM images of the SAM taken before and after O(^{3}P) exposure show an expansion of the ordered lattice resulting from formation of the new nonlinear molecular structures within the adsorbed film and the reaction preferentially propagates along the lattice direction of the monolayer domain. This approach of using pre-oriented reactive molecules in ordered self-assembled monolayers in combination with angle and velocity selected energetic reagents provides a general approach for probing the geometric constraints associated with the reaction dynamics for a wide range of chemical reactions.

3.1 Introduction

At the heart of chemistry lies an initiative to both elucidate and predict the behavior of chemical reactions through analysis of the complex molecular dynamics taking place. Direct study of reaction mechanisms, however, is naturally precluded by establishment of some degree of control over the intended pathways. Historically, this has been accomplished in the gas phase through either excitation of relevant internal states of reacting molecules[1-3] or controlling their mutual orientation.[4] Early examples in the literature of the latter method include alignment of polar molecules in molecular beams using either hexapole or "brute-force" techniques.[5,6]

Our goal is to apply this same notion of dynamic control by dosing reactive species prepared in a molecular beam to the exposed interface of a self-assembled monolayer. SAMs offer unique opportunities to probe the mechanisms of reactions at interfaces due to their well-defined, ordered structures and chemical stability, and organothiolates on gold are a classically robust system of choice for studying reactions of organic matter.[7] Their self-assembly in solution is often simple and effective, utilizing precursors with nearly any functional terminus of choice.[8,9] The use of a SAM surface as an ensemble of reactants is also advantageous due its ability to rapidly dissipate excess energy.[10-12] Highly energetic intermediates that fall apart or further react in the gas phase can instead be "trapped" at the interface and be directly observed, a process akin to collisional stabilization in the gas phase at high pressures. Utilizing reflective spectroscopic techniques and high-resolution scanning probe microscopy, we are uniquely situated to successfully characterize reactions occurring at these interfaces in both real time and real space.

We aim to directly observe reaction intermediates in the foundational reactions of O(^{3}P) with unsaturated hydrocarbons using this technique, specifically considering addition onto phenyl-substituted alkynes. Reactions with phenylacetylene, 2-propynylbenzene, and biphenylacetylene have previously been experimentally characterized, with energetic barriers associated with O(^{3}P) addition onto the side chains measured to be low (< 8 kJ/mol) compared with the phenyl rings (~20 kJ/mol).[13,14] Specifically in the case of biphenylacetylene, Eichholtz *et al.* reported the formation of biphenyl as a main product and proposed a mechanism for its formation through, in part, decomposition of a vibrationally-excited biphenylketene via phenyl ring migration to release CO.[14] This mechanism is supported by experimental[15-17] and theoretical[18-22] studies of analogous reactions with acetylene and other substituted alkynes where CO formation results from cleavage of singlet ketenes formed from intersystem crossing of long-lived triplet ketocarbenes. These observations are also in line with experimental studies of O(^{3}P) addition onto ethylene, where intersystem crossing is observed to contribute heavily to overall product formation.[23,24]

Ketenes have previously been directly observed in studies of acetylene/O(^{3}P) reactions in low-temperature solid matrices[25] and at high pressures,[26] so the ability to directly observe the biphenylketene intermediate expected in this reaction via rapid thermal equilibration of the terminal intermediate with the SAM matrix is expected. The SAMs used in this study were composed of oligo(phenylene ethynylene)thiolate (oPE) molecules which have previously been shown to self-assemble onto Au(111) in solution to form well-ordered, densely-packed monolayers of upright molecules.[27-29] This surface yields an exposed interface of phenyl-substituted alkyne bonds.

3.2 Experimental

A. SAM Preparation

oPE-SAMs were prepared on commercially-fabricated Au(111) substrates deposited onto mica (1.1 cm x 1.0 cm), obtained from Agilent Technologies. These substrates were cleaned in a commercial UV/O_3 cleaning unit for two hours, rinsed thoroughly with ethanol, and dried under a stream of pure nitrogen prior to immersion into a solution containing the oPE-SAM precursor.

2 mg of *S*-[4-[2-[4-(2-Phenylethynyl)phenyl]ethynyl]phenyl]thioacetate (oPE) and 25 μL of 30%(w/v) aqueous NH_3 (both obtained from Sigma-Aldrich) was diluted to 10 mL in a 2:1 acetone/ethanol mixture to form a 0.5 mM thiolate solution, similar to literature preparation.[30] A thioacetate precursor was used instead of the free thiol to prevent side-reactions with functional groups in the SAM precursor backbone. Since SAMs formed from thioacetates are inferior in quality compared to those formed from free thiols,[31] the acetate protecting group is removed via base-catalyzed hydrolysis initiated by the addition of NH_3. The prepared solutions were left to sit at room temperature, with 30 minutes being sufficient for complete deprotection,[32] and the cleaned Au(111) substrates were immersed into these solutions for 24 hours at 60 ℃, followed by subsequent washes in fresh 2:1 acetone/ethanol and pure ethanol. This method routinely produces SAMs of high quality.[27,31]

B. Molecular Beam/Reflection-Absorption Infrared Spectroscopy

All reactions were carried out in a molecular beam scattering apparatus that consisted of an ultra-high vacuum chamber and supersonic molecular beam. Previous publications have described this instrument in great detail,[33] so only a brief description including the relevant modifications is included here.

A radio-frequency plasma source was used to generate a supersonic atomic oxygen beam formed by igniting and expanding a gas mixture of 5% O_2 in Neon through a water-cooled quartz nozzle. The beam is characterized using time-of-flight techniques to determine both the extent of O_2 dissociation and the average kinetic energy of the resultant $O(^3P)$ atoms. Typical experimental conditions yield an $O(^3P)$ flux of 9×10^{13} atoms/cm^2/s, impinging upon SAM surfaces at normal incidence with an average kinetic energy of 9 kJ/mol. The energy was chosen to discourage side reactions, namely the addition of $O(^3P)$ onto the phenyl rings of oPE-SAM occurring near 18 kJ/mol.[14] Flux is determined from monitoring the change in pressure within the reaction chamber when it is open to the incoming beam, given that the extent of O_2 dissociation is known.

In situ time-resolved reflection-absorption infrared spectroscopy (RAIRS) is accomplished through the use of incoming infrared radiation from a commercial IR spectrometer (Nicolet 6700), which is polarized perpendicular to the substrate of interest prior to reflection at a 75 °incidence angle and collected with a liquid-nitrogen-cooled HgCdTe detector. Spectra were averages of 1000 scans at a 2 cm^{-1} resolution taken in reference to a clean Au(111)/mica substrate, with peaks fit to Gaussian line shapes with cubic polynomial baselines using a nonlinear least-squares routine. The time-resolved nature of this technique stems from the ability to block the incoming $O(^3P)$ with the beam flag, allowing for precise control over the amount of time the SAM is exposed to incoming $O(^3P)$.

C. UHV-STM

All scanning tunneling microscopy (STM) images were taken at room temperature in a commercial UHV-STM system (UHV 300 from RHK Technology, Inc.), with a base pressure of

$1x10^{-10}$ Torr. Reacted SAMs were exposed to the molecular beam in the RAIRS system before transferring through air to the STM system, with total exposure to air lasting less than ten minutes. STM images were taken with typical scanning parameters of ±0.7 V and 40-50 pA. Fresh oPE-SAM samples were prepared for each reacted surface imaged.

3.3 Results

RAIRS signals detailed in Figure 3.1 show relevant absorption bands of oPE-SAM on polycrystalline gold substrates, the locations of which are in good agreement with literature.[28] Due to the surface selection rule, only vibrational modes with dipole moments perpendicular to the surface are observable,[34] allowing inferences regarding molecular orientation to be made. The average tilt angle of the molecules relative to the surface normal was not quantitatively characterized in this study, however the most intense peaks observed correspond to modes with transition dipole moments parallel to the molecular axis. This is consistent with the oPE molecules being anchored with their molecular axes nearly perpendicular to the substrate, which is expected since SAMs composed of these and similar oligophenyl molecules have been reported to exhibit small tilt angles relative to the surface normal.[27,29,35-38]

Scanning tunneling microscopy images of the pristine oPE-SAM are shown in Figure 3.2. The oPE molecules form highly-ordered domains composed of two distinct close-packed structures: (1) a $(\sqrt{3} \times 2\sqrt{3})R30^{\circ}$ structure commensurate with the underlying Au(111) surface, containing lattice constants of a = 5.0 Å and b = 9.7 Å and observed by Sita *et al.*[28] and (2) an incommensurate structure with a rectangular lattice of a = 5.5 Å and b = 8.0 Å observed by Liu *et al.*[29] While both of these domains coexist on the surface and are shown in Figure 3.1B, we observe ~75% of the monolayer is composed of the incommensurate structure under our preparation conditions. Additionally, this structure remains constant throughout a bias voltage range of ±1 V.

The close-packed oPE molecules are bonded to the underlying Au(111) through the sulfur atom, with the molecular chain standing near-perpendicular to the surface (Figure 3.2C). Adjacent molecules are rotated to maximize π-π interactions between the benzene substituent on neighboring chains, forming a herringbone-styled array of molecules across the domain. The face of the benzene rings located on the same molecular chain are orientated along the same plane and

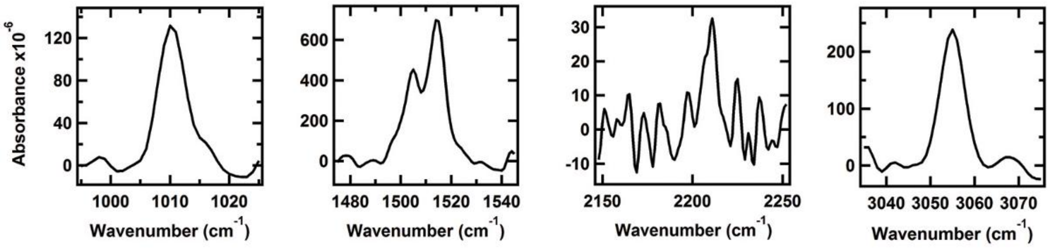

Figure 3.1. Relevant vibrational modes of prepared oPE-SAM as measure by RAIRS: (from left to right) C-C bending mode at 1010 cm^{-1}, C=C semicircle stretches at 1504 and 1514 cm^{-1}, alkyne stretching mode at 2210 cm^{-1}, C-H stretching mode at 3055 cm^{-1}. All modes are parallel to the molecular axis.

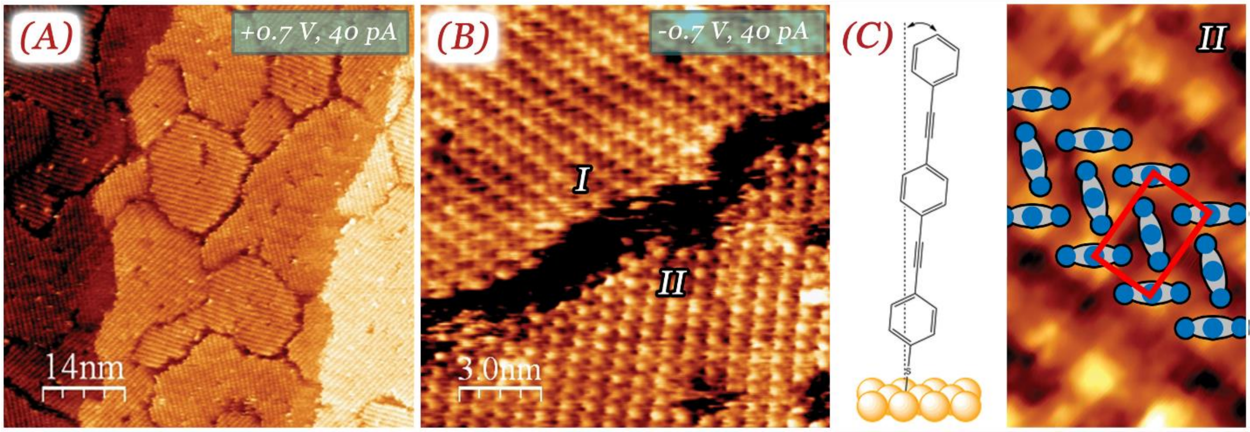

Figure 3.2. **(A)** oPE readily forms an ordered monolayer with large domains on Au(111) in solution. **(B)** The monolayer consists of two types of domains: a “commensurate” (I) and “incommensurate” (II) structure, both of which have been observed previously in the literature. We observe that the overall structure of the monolayer is dominated (~75%) by the “incommensurate” domains. **(C)** The oPE molecules are anchored with their molecular axes nearly perpendicular to the Au(111) substrate. Intermolecular interactions are the main driving force for this ordering, resulting in a herringbone-like packing on the surface.

locked into this position by the triple bonds between the carbon atoms; this results in a different structure than self-assembled monolayers composed of biphenylthiol molecules, in which the orientation of the benzenes are independent from one another and are rotated with respect to each other on the same molecule to minimize steric effects.[39]

The rectangular unit cell is composed of oPE molecules that appear as both bright and dark features in the STM image. Liu et. al proposed that the difference in apparent STM height is the result of a change in the electronic structure between oPE molecules bound at different Au(111) lattice sites;[29] however, replicating the unit cell across a bulk-terminated Au(111) surface does not result in consistent binding locations for a given feature (i.e. not all "bright" molecules bind at the same Au(111) lattice site). More recently, a number of experimental groups have revealed the presence of gold adatoms at the interface of bulk-terminated Au(111) and thiol-based self-assembled monolayers.[40-44] While STM is unable to image the gold-monolayer interface directly, changes in relative electronic structure across the monolayer surface is detectable and we believe the rectangular unit cell with bright and dark features is the result of a complex interfacial structure involving bulk-terminated Au(111), gold adatoms, and oPE molecules. Further study of oPE SAM formation is needed to fully explain this observation.

3.4 Discussion

A. Mechanism of O(^{3}P)/oPE-SAM Reaction

Upon exposure to O(^{3}P), distinct structural changes in the SAM are observed. These changes are summarized in Figure 3.3. The most notable is the appearance of a new mode at 2102 cm^{-1} immediately upon exposure of oPE-SAM to O(^{3}P). The peak position is consistent with formation of a ketene, and closely matches that of the C=C=O stretching mode of biphenylketene

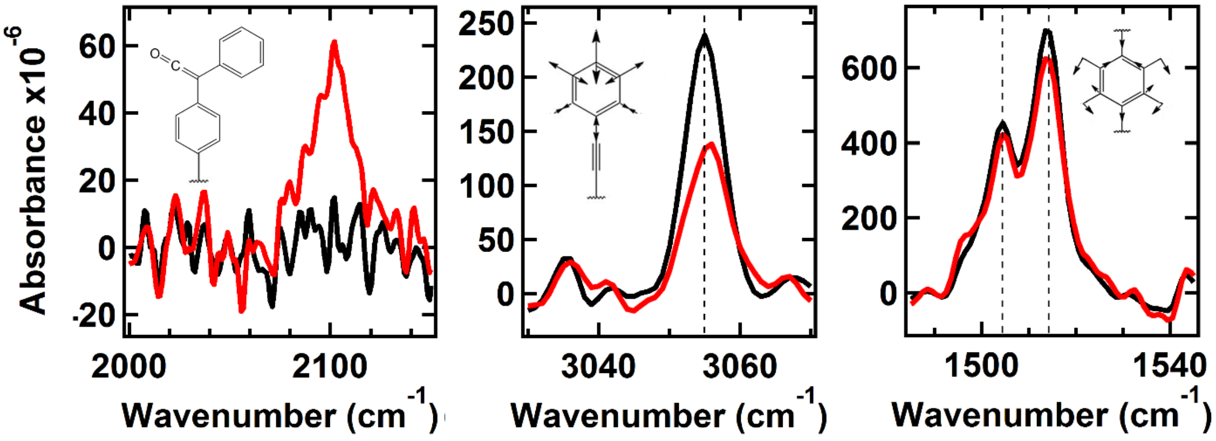

Figure 3.3. RAIRS spectra of monolayer before (black) and after (red) exposure of ~8 x 10^{15} $O(^3P)/cm^2$. New mode associated with ketenyl stretching appears at 2102 cm^{-1} (left), consistent with expected position of a biphenylketene-like moiety. Peak associated with C-H stretching mode of the phenyl ring at the vacuum/film interface (middle) decreases significantly upon exposure of the monolayer to $O(^3P)$. Other peaks, such as the C=C semicircle stretching modes (right), remain unchanged at this level of exposure, suggesting that initial exposure results in formation of ketenes, resulting in canting of interfacial phenyl rings' planes towards the substrate, with the rest of the molecular backbone remaining intact.

at 2094 cm^{-1}.[45] This is consistent with an expected product of electrophilic addition of O(^{3}P) onto an alkyne bond in oPE. In the gas phase, a phenyl shift occurring after addition onto biphenylaceylene results in a highly vibrationally-excited triplet ketene, which cleaves to form CO and a carbene. On the thermally equilibrated surface, however, the excess energy from the reaction can dissipate through the SAM matrix. Additionally, the triplet biradical intermediate is likely stabilized on the surface to the singlet ketene, similar to collisional stabilization by surrounding inert gases in high-pressure gas reactions. While we can make no spectroscopic distinction between the two alkyne bonds of oPE, the argument can nevertheless be made that the alkyne bond closest to the vacuum/film interface is initially the most accessible.

Formation of a nonlinear ketene structure at the vacuum/film interface would naturally result in the canting of the interfacial benzene, given that the other end of the molecule is anchored to the substrate. Concurrent with the appearance of the ketene mode, exposure results in significant decay of the phenyl C-H peak at 3055 cm^{-1} alone; this change is not reciprocated in the rest of oPE-SAM's IR signals. We assign this peak to the C-H stretching mode (20a) of the monosubstituted benzene of oPE located at the vacuum/film interface.[46] Decay of the 20a mode is attributed to a change in orientation of the phenyl ring plane—and therefore the orientation of the 20a transition dipole moment (TDM)—relative to the surface normal. The decrease supports canting of the ring, resulting in the 20a TDM ending up more parallel to the surface plane. Due to the surface selection rule of RAIRS, the intensity appears smaller due to the decrease in the magnitude of the perpendicular component of the 20a TDM even though the structure is still on the surface. The parallel component is "invisible" since the image dipole induced by the gold surface is equal in magnitude but opposite in direction, effectively cancelling it out.

It is important to address other possible causes for the decrease in C-H mode intensity. Abstraction of hydrogen atoms from the phenyl rings can be ruled out due to the associated high energetic barrier (~60 kJ/mol for benzene[46]). Due to the persistence of the rest of the modes, oxidation of sulfur headgroups leading to desorption of entire chains does not satisfactorily account for the observed decay. Were this the case, all modes belonging to oPE would decay to the same extent, but the modes associated with C=C semicircle stretches, for example, decay by only a few percent over this same exposure (Figure 3.3C). It is also worth noting that these changes in the SAM take place only when O(^{3}P) is present in the molecular beam. Control trials using a pure neon discharge or an O_2 gas source, seeded in either helium or neon, without the discharge resulted in no detectable change in the structure of the SAM over similar total exposures. We can thus conclude that the structural changes are directly attributable to the presence of O(^{3}P).

Based on the above observations, we are able to propose a mechanism for the reaction of O(^{3}P) with oPE-SAM, a schematic of which is detailed in Figure 3.4. Upon dosing O(^{3}P) onto oPE-SAM, the oxygen atoms react with the alkyne bond closest to the vacuum/film interface first to form a triplet biradical intermediate. This intermediate undergoes a phenyl shift to yield a vibrationally-excited ketene that is stabilized on the surface to its singlet state, yielding in a nonlinear biphenylketene-like moiety located at the vacuum/film interface. This reaction results in the canting of the interfacial phenyl ring’s molecular plane towards the substrate.

This mechanism is further corroborated by STM images of reacted oPE-SAM. The STM current, and therefore the “height” in an STM image, is a combination of both the electronic state and the topographic height; STM is not able to directly perform chemical analysis of individual molecules. Figure 3.5 shows a partially reacted oPE monolayer that contains areas of both reacted and unreacted molecules after ~3 x 10^{15} O(^{3}P)/cm^2 of exposure. We assign the bright molecules

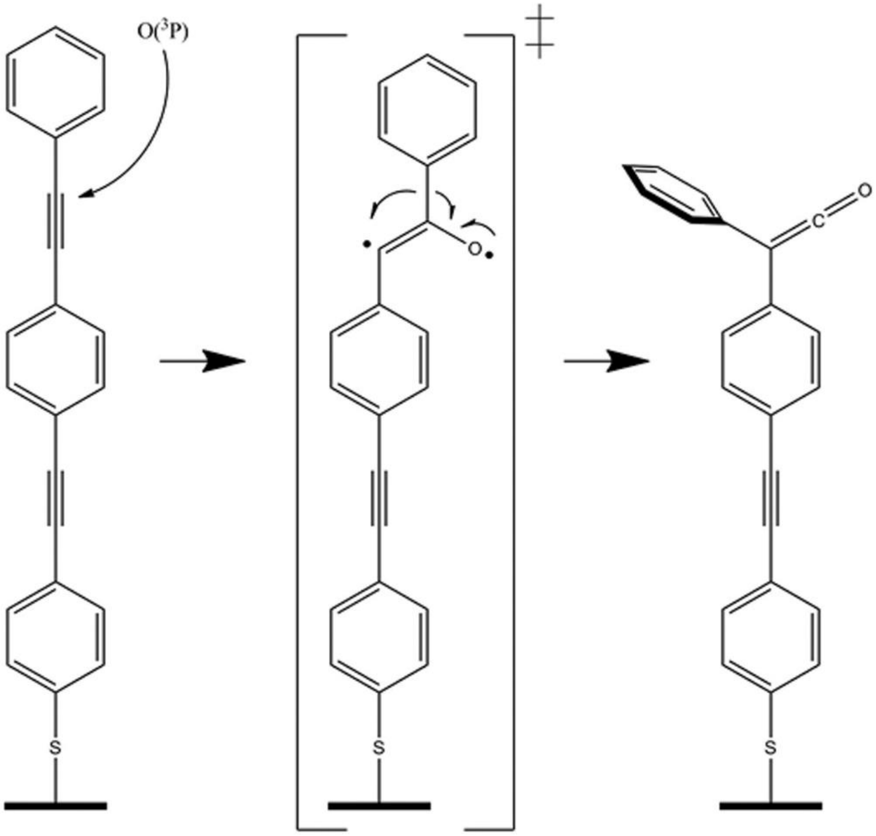

Figure 3.4. Proposed mechanism for O(^{3}P) reaction with oPE-SAM: electrophilic addition of O(^{3}P) onto the alkyne bonds closest to the vacuum/film interface results in formation of a triplet biradical intermediate that undergoes phenyl migration and is stabilized to singlet ketene by rapid equilibration with the SAM matrix.

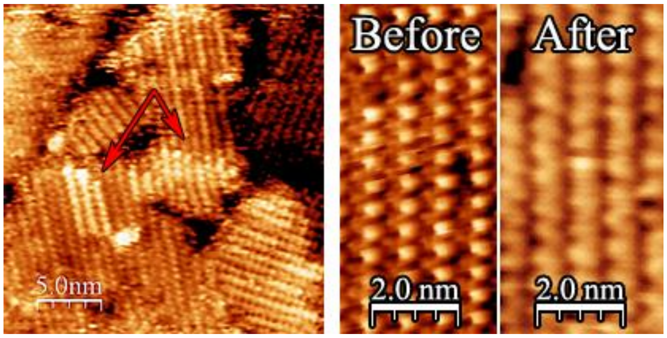

Figure 3.5. STM images (0.7 V, 40 pA) of oPE-SAM after exposure of ~3 x 10^{15} O(^{3}P)/cm^2 show that this reaction does not occur initially at domain boundaries, but instead propagates along rows of the unit cell due to greater accessibility of nearby alkyne bonds after canting of the first interfacial phenyl ring. A rectangular lattice is conserved, but with expanded dimensions (0.5 Å along each unit cell direction) to accommodate the newly-formed nonlinear structures.

as reacted oPE, based on an increased spacing of the lattice at these particular sites, while the darker molecules approximately retain the pristine lattice spacing. As observed in the RAIRS spectra, upon the formation of the ketene on a reacted molecule, the face of the top benzene rotates downward and becomes more parallel to the gold surface. The reacted molecules appear brighter in the STM image despite the lower topographic height due to the change in the electronic structure upon the addition of the ketene and the resulting exposure of the benzene face. Neighboring unreacted oPE chains tilt and adjust to accommodate the wider reacted molecule, forcing the lattice to expand. Figure 3.5 also shows a direct comparison between the unreacted and reacted SAM, where the monolayer has maintained a rectangular unit cell and its lattice constants have expanded to a = 6.0 Å and b = 8.5 Å.

We observe in the STM images (Figure 3.5) that monolayer reactivity takes place at preferential sites. Interestingly, the reaction does not appear to occur initially at every molecule located along a domain boundary, where the triple bond would be the most exposed to the incident oxygen atoms, before propagating to molecules located in the interior of the domain. Instead we observe the reacted molecules always occur along rows of the unit cell. After the reaction takes place at an initial molecule, the benzene rotates parallel to the gold surface and the neighboring molecules expand slightly to accommodate the change in structure. This increases the accessibility of the triple bond on a neighboring molecule to additional oxygen atoms, propagating the reaction along a lattice direction and into the monolayer.

It is worth noting, finally, that continued exposure of oPE-SAM to $O(^3P)$ results in severe disordering of the monolayer. All RAIRS peaks associated with oPE have significantly decayed in intensity by the time the monolayer has been exposed to ~50 x 10^{15} $O(^3P)/cm^2$. This is corroborated with STM images which display no molecular resolution at this level of exposure.

B. Kinetics of the O(^{3}P)/oPE-SAM Reaction

Appearance of the ketene mode, while reproduceable, yields an IR signature that is weak in intensity. Additionally, ketenes formed may undergo further reaction with O(^{3}P) or O_2 as exposure continues. We have therefore monitored the kinetics of the reaction by characterizing the decay of the stronger 20a mode as a function of total exposure, detailed in Figure 3.6, which follows a first-order decay. As exposure increases, the intensity of this mode clearly does not approach zero, instead decaying to a value roughly 25% that of the original intensity. This observation agrees well with the proposed mechanism. Assuming the oPE chain is nearly perpendicular to the substrate, formation of the ketene results in the angle between surface normal and the 20a TDM increasing from ~0 ° to ~60 °. This results in the magnitude of the perpendicular component of the TDM decreasing to roughly one-half its original value. Given intensity is proportional to the square of the TDM's magnitude, the relative intensity of the 20a mode should be roughly one-fourth its initial value.

Taking into account the above points, we can assert that the total signal prior to exposure represents a fraction of remaining interfacial alkyne bonds of 100%. Additionally, the total signal as exposure approaches infinity approximates a remaining fraction of zero. At any point in between, the total 20a intensity is approximately a combination of these two values:

$$I_{tot} = I_{100\%}\theta + I_{0\%}(1 - \theta) \tag{3-1}$$

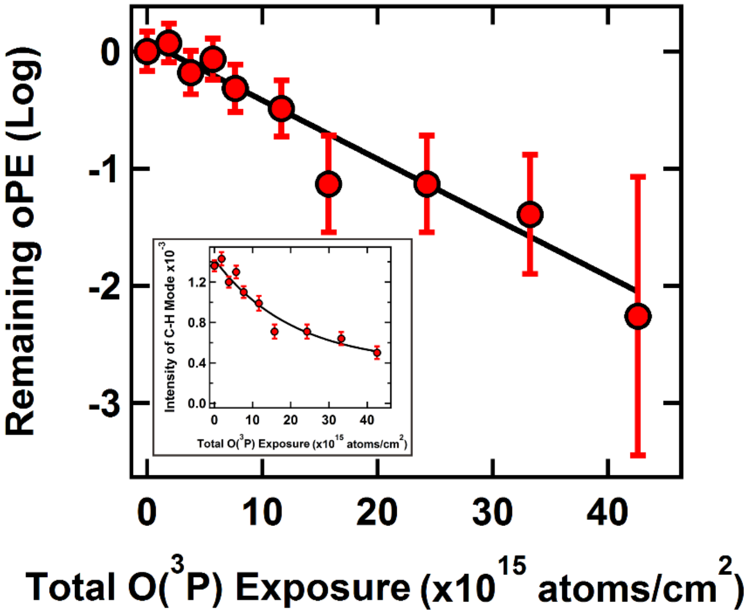

Figure 3.6. Plotting the log of remaining unreacted oPE versus total O(^{3}P) exposure yields a linear trend. Fitting the data to a Langmuirian model results in a reaction probability of 7 ±2%. These data were derived from the decay of the C-H stretching mode intensity at 3055 cm^{-1} (inset), which tends towards ~25% of its original intensity given that the decay is a change in orientation of the interfacial phenyl ring relative to the substrate and not entire removal of the structure.

where θ is the aforementioned fraction; each data point can be converted to a remaining fraction. Plotting the natural log of this fraction versus the total O(^{3}P) exposure yields a linear decay, which fits well to a first-order Langmuirian model for the rate of O(^{3}P) addition onto the alkyne bond located closest to the vacuum/film interface. This allows for estimation of the initial reaction probability, γ_o[47]:

$$\ln\theta = -(\gamma_o/4A)\Phi \qquad (3\text{-}2)$$

where Φ is the total exposure of O(3P), and A is the average density of oPE molecules on the surface. A weighted linear least-squares fit to the data yields an initial reaction probability of 7 ± 2%. The average surface density, A, was estimated from the STM data, where the commensurate (~25%) and incommensurate (~75%) structure unit cells are calculated to contain 2 molecules per 44 ± 1 Å^2 and 48 ± 1 Å^2, respectively.

Use of the SAM as an ensemble of reactants provides a framework for controlling how reactants encounter each other in real space. The barrier for addition onto the alkyne bond of biphenylacetylene in the gas phase was measured by Eichholtz *et al.* to be 0.6 kJ/mol. Collisions between O(^{3}P) and oPE-SAM occur at the phenyl rings decorating the vacuum/film interface, where no reaction is observed to occur due to unfavorable energetics. Enforcing the majority of collisions to occur under unfavorable conditions yields a low reaction probability despite incident O(^{3}P) atoms having kinetic energies (9 kJ/mol) far above the energetic barrier. Only when incoming oxygen atoms penetrate the interface can they react with the underlying alkyne bonds.

The most readily-accessible alkyne bonds in oPE-SAM are obscured from direct reaction by the interfacial phenyl rings, and so the addition reaction would not be expected to follow Eley-Rideal kinetics and instead involve incorporation of O(^{3}P) into the SAM. Although gas-surface interactions utilizing oligophenylthiolate SAMs have not been explicitly characterized in the literature, studies of these types of interactions with *n*-alkanethiol SAMs are plentiful. It is established that lateral motion in these SAMs effectively dissipates energy from collisions of gaseous species.[10-12,48,49] Specifically it has been suggested that, for O(^{3}P) collisions with *n*-alkanethiol SAMs under conditions similar to those outlined in this study, physisorption onto the interface dominates—only ~27% of O(^{3}P) penetrates the interface.[49] It is readily apparent, therefore, that the low reaction probability is a direct result of the change in accessibility of the alkyne bonds in the SAM versus the gas phase. This is also in line with the findings of Eichholtz *et al.*, where the pre-exponential factor for addition onto the alkyne bond was measured to be nearly two orders of magnitude smaller than addition onto the phenyl ring.[14] Enforcing the majority of collisions to occur with the phenyl rings naturally yields a lower probability for the addition reaction. Thus the ability to stereodynamically control a reaction is demonstrated herein, in this case by restricting accessibility to a reactive group just below the immediate vacuum/film interface.

3.5 Conclusions

Utilizing a combination of *in situ* RAIRS and STM, we have characterized and confirmed the mechanism of the reaction of O(^{3}P) with phenyl-substituted alkynes. *In situ* RAIRS indicates that decay of the phenyl mode at the vacuum/film interface is a result of ketene formation between the top two phenyl rings of oPE-SAM and subsequent canting of the phenyl moiety towards the substrate plane. Subsequent characterization of changes in local topology using STM completes the picture by establishing that the reaction propagates along rows of the unit cell due to increased accessibility of a neighboring triple bond after one oPE molecule reacts. Kinetic measurements support a mechanism that relies on incorporation of O(^{3}P) into the SAM matrix in order for reaction to occur. Unfavorable geometric constraints imposed upon the reactants’ approach yield low initial reaction probability despite establishing sufficient energetics. Through direct observation of the ketene intermediate, the use of oPE-SAM as a scaffold for an ensemble of oriented reactants proves effective in facilitating rapid thermal equilibration and detection of intermediate products.

A crucial next step is to utilize SAMs in this manner with reactive groups located directly at the vacuum/film interface. Approaching reactants prepared in a supersonic beam could undergo direct reactions exhibiting Eley-Rideal kinetics given that incoming reactants have translational energies near or above associated energetic barriers. SAMs can readily be prepared with interfacial reactive groups in different orientations with respect to the surface plane, providing a direct route to stereochemical control. This technique is effective for the elucidation of orientation-dependent kinetics, with the added ability to "collisionally stabilize" reactive intermediates not necessarily detectable under, as an example, crossed molecular beam techniques using high collision energies.

3.6 Acknowledgments

This work was supported by the National Science Foundation, Award Number CHE-0911424. Partial support from the NSF Materials Research Science and Engineering Center at the University of Chicago is also acknowledged, Award Number NSF-DMR-0820054.

References

1. Polanyi, J.C. *Acc. Chem. Res.* **1972,** *5,* 161-168.
2. (a) Bernstein, R.B. *Chemical Dynamics via Molecular Beam and Laser Techniques*; Clarendon Press Oxford University Press: Oxford New York, 1982. (b) Levine, R.D.; Bernstein, R.B. *Molecular Reaction Dynamics and Chemical Reactivity*; Oxford University Press: Oxford New York, 1987.
3. Moore, C.B.; Smith, I.M.W. *Faraday Discuss. Chem. Soc.* **1979,** *67,* 146-161.

4. Orr-Ewing, A.J. *J. Chem. Soc. Faraday Trans.* **1996,** *92*, 881-890.
5. Parker, D.H.; Bernstein, R.B. *Annu. Rev. Phys. Chem.* **1989,** *40*, 561-595.
6. Loesch, H.J. *Annu. Rev. Phys. Chem.* **1995,** *46*, 555-594.
7. Love, J.C.; Estroff, L.A.; Kriebel, J.K.; Nuzzo, R.G.; Whitesides, G.M. *Chem. Rev.* **2005,** *105*, 1103-1169.
8. Ulman, A. *Chem. Rev.* **1996,** *96*, 1533-1554.
9. Schreiber, F. *Prog. Surf. Sci.* **2000,** *65*, 151-256.
10. Gibson, K.D.; Isa, N.; Sibener, S.J. *J. Chem. Phys.* **2003,** *119*, 13083-13095.
11. Isa, N.; Gibson, K.D.; Yan, T.; Hase, W.L.; Sibener, S.J. *J. Chem. Phys.* **2003,** *120*, 2417-2433.
12. Lu, J.W.; Day, B.S.; Fiegland, L.R.; Davis, E.D.; Alexander, W.A.; Troya, D.; Morris, J.R. *Prog. Surf. Sci.* **2012,** *87*, 221-252.
13. Sloane, T.M.; Brudzynski, R.J. *J. Am. Chem. Soc.* **1979,** *101*, 1495-1499.
14. Eichholtz, M.; Kohl, S.; Schneider, A.; Vollmer, J.-T.; Wagner, H.G. *Symp. Int. Combust. Proc.* **1996,** *26*, 527-534.
15. Kanofsky, J.R.; Lucas, D.; Pruss, F.; Gutman, D. *J. Phys. Chem.* **1974,** *78*, 311-316.
16. Arringtion, Jr., C.A.; Cox, D.J. *J. Phys. Chem.* **1975,** *79*, 2584-2586.
17. Schmoltner, A.M.; Chu, P.M.; Lee, Y.T. *J. Chem. Phys.* **1989,** *91*, 5365-5373.
18. Harding, L.B. *J. Phys. Chem.* **1981,** *85*, 10-11.
19. Harding, L.B.; Wagner, A.F. *J. Phys. Chem.* **1986,** *90*, 2974-2987.
20. Xing, G.; Huang, X.; Wang, H.; Bersohn, R. *J. Chem. Phys.* **1996,** *105*, 488-495.
21. Girard, Y.; Chaquin, P. *J. Phys. Chem. A* **2003,** *107*, 10462-10470.
22. Nguyen, T.H.; Vereecken, L.; Peeters, J. *J. Phys. Chem. A* **2006,** *110*, 6696-6706.

23. Schmoltner, A.M.; Chu, P.M.; Brudzynski, R.J.; Lee, Y.T. *J. Chem. Phys.* **1989,** *91,* 6926-6936.
24. Casavecchia, P.; Capozza, G.; Segoloni, E.; Leonori, F.; Balucani, N.; Volpi, G.G. *J. Phys. Chem. A* **2005,** *109*, 3527-3530.
25. Haller, I.; Pimentel, G.C. *J. Am. Chem. Soc.* **1962,** *84,* 2855-2857.
26. Gaedtke, H.; Glänzer, K.; Hippler, H.; Luther, K.; Troe, J. *Symp. Int. Combust. Proc.* **1979,** *14,* 295-303.
27. Tour, J.M.; Jones II, L.; Pearson, D.L.; Lamba, J.J.S.; Burgin, T.P.; Whitesides, G.M.; Allara, D.L.; Parikh, A.N.; Atre, S.V. *J. Am. Chem. Soc.* **1995,** *117,* 9529-9534.
28. Dhirani, A.-A.; Zehner, R.W.; Hsung, R.P.; Guyot-Sionnest, P.; Sita, L.R. *J. Am. Chem. Soc.* **1996,** *118,* 3319-3320.
29. Yang, G.; Qian, Y.; Engtrakul, C.; Sita, L.R.; Liu, G. *J. Phys. Chem. B* **2000,** *104,* 9059-9062.
30. Cai, L.; Yao, Y.; Yang, J.; Price, Jr., D.W.; Tour, J.M. *Chem. Mater*. **2002,** *14*, 2905-2909.
31. Béthencourt, M.I.; Srisombat, L.; Chinwangso, P.; Lee, T.R. *Langmuir* **2009,** *25,* 1265-1271.
32. Singh, A.; Dahanayaka, D.H.; Biswas, A.; Bumm, L.A.; Halterman, R.L. *Langmuir* **2010,** *26,* 13221-13226.
33. Sibener, S.J.; Buss, R.J.; Ng, C.Y.; Lee Y.T. **1980,** *51,* 167-182.
34. Greenler, R.G. *J. Chem. Phys.* **1966,** *44,* 310-315.
35. Duan, L.; Garrett, S.J. *J. Phys. Chem. B* **2001,** *105*, 9812-9816.
36. Ulman, A.; Kang, J.F.; Shnidman, Y.; Liao, S.; Jordan, R.; Choi, G.-Y.; Zaccaro, J.; Myerson, A.S.; Rafailovich, M.; Sokolov, J.; Fleischer, K. *Rev. Mol. Biotechnol.* **2000,** *74,* 175-188.

37. Dunbar, T.D.; Cygan, M.T.; Bumm, L.A.; McCarty, G.S.; Burgin, T.P.; Reinerth, W.A.; Jones, II, L.; Jackiw, J.J.; Tour, J.M.; Weiss, P.S.; Allara, D.L. *J. Phys. Chem. B* **2000,** *104,* 4880-4893.

38. Kang, J.F.; Ulman, A.; Liao, S.; Jordan, R.; Yang, G.; Liu, G. *Langmuir* **2001,** *17*, 95-106.

39. Matei, D.G.; Muzik, H.; Gölzhäuser, A.; Turchanin, A. *Langmuir* **2012,** *28,* 13905-13911.

40. Maksymovych, P.; Yates, Jr., J.T. *J. Am. Chem. Soc.* **2008,** *130,* 7518-7519.

41. Maksymovych, O.; Voznyy, O.; Dougherty, D.B.; Sorescu, D.C.; Yates, Jr., J.T. *Prog. Surf. Sci.* **2010,** *85,* 206-240.

42. Kautz, N.A.; Kandel, S.A. *J. Am. Chem. Soc.* **2008,** *130,* 6908-6909.

43. Kautz, N.A.; Kandel, S.A. *J. Phys. Chem. C* **2009,** *113,* 19286-19291.

44. Jobbins, M.M.; Raigoza, A.F.; Kandel, S.A. *J. Phys. Chem. C* **2011,** *115,* 25437-25441.

45. Cerioni, G.; Plumitallo, A.; Frey, J.; Rappoport, Z. *Magn. Res. Chem.* **1995,** *33,* 669-673.

46. Barry, N.J.; Fletcher, I.W.; Whitehead, J.C. *J. Phys. Chem.* **1986,** *90,* 4911-4912.

47. Lu, J.W.; Fiegland, L.R.; Davis, E.D.; Alexander, W.A.; Wagner, A.; Gandour, R.D.; Morris, J.R. *J. Phys. Chem. C* **2011,** *115,* 25343-25350.

48. Yan, T.; Isa, N.; Gibson, K.D.; Sibener, S.J.; Hase, W.L. *J. Phys. Chem. A* **2003,** *107,* 10600-10607.

49. Tasić, U.S.; Yan, T.; Hase, W.L. *J. Phys. Chem. B* **2006,** *110,* 11863-11877.

CHAPTER 4

MOLECULAR INTERACTIONS WITH ICE: MOLECULAR EMBEDDING, ADSORPTION, DETECTION AND RELEASE

The data presented in this chapter was previously published in the Journal of Chemical Physics. The following content was reprinted with permission from [K. D. Gibson, Grant G. Langlois, Wenxin Li, Daniel R. Killelea, and S. J. Sibener, "Molecular interactions with ice: Molecular embedding, adsorption, detection, and release" J. Chem. Phys., DOI: 10.1063/1.4895970 (2014).] Copyright 2014, American Institute of Physics.

The interaction of atomic and molecular species with water and ice is of fundamental importance for chemistry. In a previous series of publications, we demonstrated that translational energy activates the embedding of Xe and Kr atoms in the near surface region of ice surfaces. In this paper, we show that inert molecular species may be absorbed in a similar fashion. We also revisit Xe embedding, and further probe the nature of the absorption into the selvedge. CF_4 molecules with high translational energies (≥ 3 eV) were observed to embed in amorphous solid water. Just as with Xe, the initial adsorption rate is strongly activated by translational energy, but the CF_4 embedding probability is much less than for Xe. In addition, a larger molecule, SF_6, did not embed at the same translational energies that both CF_4 and Xe embedded. The embedding rate for a given energy thus goes in the order Xe > CF_4 > SF_6. We do not have as much data for Kr, but it appears to have a rate that is between that of Xe and CF_4. Tentatively, this order suggests that for Xe and CF_4, which have similar van der Waals radii, the momentum is the key factor in determining whether the incident atom or molecule can penetrate deeply enough below the surface to embed. The more massive SF_6 molecule also has a larger van der Waals radius, which appears to prevent it from stably embedding in the selvedge. We also determined that the maximum depth of embedding is less than the equivalent of four layers of hexagonal ice, while some of the atoms just below the ice surface can escape before ice desorption begins. These results show that energetic ballistic embedding in ice is a general phenomenon, and represents a significant new channel by which incident species can be trapped under conditions where they would otherwise not be bound stably as surface adsorbates. These findings have implications for many fields including environmental science, trace gas collection and release, and the chemical composition of astrophysical icy bodies in space.

4.1 Introduction

Ice surfaces are nearly ubiquitous in nature, and collisions of gas-phase species with ice surfaces alter the composition and morphology of the ice.[1–3] In interstellar space, icy surfaces are bombarded by ions, which can penetrate well below the surface. These collisions deliver both energy and other species (C, S, N). leading to the chemical modification of the interior of the ice.[4–7] Energetic collisions of small molecules with ice surfaces are of particular relevance for the capture and matrix preconcentration of trace gases;[8,9] for gases with insufficient momentum are unable to penetrate into the ice, whereas heavier, or more energetic, species will be trapped in the near surface region of the solid.[10] Energetic collisions on ice surfaces are also highly relevant for the evolution of the composition of icy bodies in space.[11–13] In particular, collisions with impact energy of several electron volts are representative of the encounters between the surfaces of comets and the ambient molecules and atoms in interplanetary space as a comet orbits a star. The embedding of the gaseous species in the ice surface implies that the changes in the composition of comets can be modified by other mechanisms besides thermal desorption or accretion.[1,14,15] Finally, an improved understanding of how small molecules and atoms penetrate ice surfaces and stably embed is of high importance to the formation or destruction of clathrates or other systems of trapped gases in icy matrices. Methane clathrates have received consideration as an energy source,[16] and the importance of a firm fundamental understanding of clathrates and the interactions between gases and ice was evident in the efforts in capping the oil well during the Deepwater Horizon disaster.[16–18] Another area of significance is the role of trapped methane in the permafrost in the positive feedback loop of global warming.[19–21] Finally, collisions between icy particles and gases have significance in atmospheric processes.[22,23] Because of the widespread interest in the interactions of gas phase species with ice surfaces, we have chosen to expand on our previous work with noble gas embedding on ice and now examine how small molecules can become implanted in the selvedge of ice surfaces and further study the nature of the absorption sites.

In previous papers, we explored the sputtering of ice with high translational energy Xe[2] and the scattering of fast neutral Xe and Kr from the surface of ice.[10,24] On both ACS and CI, the energetic incident Xe atoms sputtered water molecules from the surface, and a well-defined, water isotope-dependent, threshold energy was observed for the sputtering that was on the order of the sublimation energy. The scattering experiments and chemical dynamics simulations[10,24] showed that the ice surfaces very efficiently accommodate the incident kinetic energy of the Xe or Kr atoms, and the energy of the scattered atoms is weakly correlated to their incident energy. These findings suggested that the scattering was not the result of simple binary collisions. Computational simulations[24] showed that the efficient energy accommodation is the result of extensive penetration of the ice by the energetic projectiles. In the course of these experiments, we discovered that a small, but significant, amount of the inert gases could be absorbed at surface temperatures well above where they could stably adsorb.[3,10] Ice was grown on single crystal metal surfaces, either Rh(111) or Au(111), in ultra-high vacuum (UHV) and were then exposed to beams of energetic Xe or Kr atoms. After the exposure, temperature programmed desorption (TPD) measurements were taken of the ice, and the signal from D_2O and either Xe or Kr was monitored as the ice temperature was ramped upwards. An exciting discovery was that Xe and Kr were observed to desorb at temperatures significantly (>50 K) above their surface desorption temperature.[25] The implication was that Xe or Kr atoms were embedded within the ice. Only when the ice was warmed during the TPD measurement could the trapped gases escape. For both Xe and Kr, the rate of implantation was directly related to the translational energy, and for a given energy, Xe embedded at a higher rate than the lighter Kr.[10,24] The amount embedded appeared to asymptotically approach a final value that was dependent on energy and mass.

These experiments also demonstrated very different embedding behaviors for crystalline ice (CI) and amorphous solid water (ASW). The morphology of the ice was determined by the deposition temperature for the ice from gas-phase water.[26–28] At temperatures below ~135 K, ASW is formed, whereas at 140 K and above, CI forms. ASW is metastable with respect to CI, and undergoes an irreversible transition to CI at ~160 K. On CI, Xe embedding appeared to be less probable, and the trapped gas only desorbed at a low temperature (~140 K), before any appreciable water desorption, whereas embedded rare gas in ASW desorbed during the thermal ramp up to ~160 K.

The focus of this paper is to more fully explore the nature of the embedding process. One question from the previous work was whether there was a difference in the adsorption sites that lead to both high and low temperature desorption, particularly since the rare gas begins to escape at an appreciable rate before the water begins desorbing. Also, we wanted to more thoroughly explore the embedding rate as a function of projectile mass and energy. In this context, we also used two other relatively inert gases with very different masses, SF_6 and CF_4. CF_4 has a strong IR signal, which allows for the use of time-resolved Fourier-transform reflection-absorption infrared spectroscopy (RAIRS) in addition to TPD. TPD is a destructive technique where constructing an uptake curve requires that each measured point be taken on a new ASW or CI film, so the experiment becomes prohibitively time consuming using this approach alone. RAIRS allows the same measurements to be made sequentially on the same ice sample, greatly facilitating these measurements, especially for systems or conditions with low embedding rates.

Both Xe and CF_4 show low temperature (before water begins desorbing) and higher temperature features in the TPD spectra from the exposure of ASW, though the low temperature feature is much larger for Xe.[3] The uptake rate for CF_4 is much less than for Xe at the same incident energy, which is consistent with our previous observations that mass (and thus the momentum) is an important consideration. However, it is also appears that the uptake rate is also less than for Kr, which has almost the same mass as CF_4. The previous experiments[10] with Xe and Kr showed that the rate of embedding decreased with exposure. The rates of CF_4 embedding vs. exposure curves were linear for all of the energies and exposures used, but the amount of CF_4 embedded had not reached a value as large as for the longest exposures of the rare gases.

By varying the TPD techniques used, we have come to the conclusion that the lower temperature TPD feature for ASW is due to adsorption just below the surface. The rest of the absorbed species escape concurrently with desorbing water, and are more deeply buried, to within ~3-4 layers of ice below the surface. For CI, only high energy Xe is embedded, and then, only in the topmost portion of the ice; the desorption peak due to more deeply buried atoms in not observed. Even at the highest energies (~5.3 eV), there was apparently no CF_4 embedding, even with the more sensitive RAIRS technique. Only at an energy <2.5 eV does Xe show embedding in ASW but not CI.

We also investigated whether a much larger, yet still inert molecule could be stably embedded in ASW. We exposed ASW to a beam of SF_6 molecules (MW = 146 g mol^{-1}), but it showed no detectable embedding in ASW, even with an energy of 3 eV, the energy at which Kr, Xe, and CF_4 all show detectable embedding. Tentatively, we ascribe this to the larger radius of this molecule relative to both CF_4 and the rare gases.

In the present paper, we expand significantly on our previous results; we explore the implantation of molecular species and further probe the nature of the absorption sites for Xe by ‘capping’ the surface of ASW after exposure to the Xe beam. Taken together, these results probe the complex interaction of energetic gas-phase species with ice, and provide further details of this exciting phenomenon. We explain our new results in the context of our previous experimental and computational findings, and improve our understanding of how the various parameters, including ice morphology, incident energy and angle, and the mass of the projectile are interrelated, leading to the penetration and stable embedding of gaseous species in ice.

4.2 Experimental

A. Thermal Desorption

Experiments entailed dosing a cryogenically cooled Rh(111) target crystal with a D_2O molecular beam, then exposing the surface to atomic beams of Xe or molecular beams of CF_4. After exposure, any absorbed gases, as well as the D_2O, were measured by performing mass spectrometric TPD experiments. The machine consists of a diffusion pumped source region, where the atomic or molecular beams were produced. The beam was skimmed, and then passed through three differential pumping regions before entering the ultra-high-vacuum (UHV) chamber and impinging upon the Rh(111) target crystal. Detection of the desorbed gases was done with a double-differential pumped quadrupole mass spectrometer, using an electron bombardment ionizer.

D_2O (m/e = 20) (Aldrich, 99.9 atom % D) was used since it had a much lower background signal than H_2O (m/e = 18) in our mass spectrometer system. This beam was produced by passing low pressure (2.25 psi (absolute)) He through a liquid filled room temperature bubbler and expanding through a 200 m pinhole. The coverage was determined from the integrated TPD spectra, and was calibrated by comparing with the TPD signal from a monolayer (ML) grown on clean Rh(111) (1 ML = 1.07×10^{15} molecules cm^{-2}).[29] Dosing rates were estimated to be ~0.5 ML sec^{-1} at normal incidence. All of the dosing was done at an incident angle of $\theta = 45^{o}$, and the total coverage was ~750 ML. We explored the effect of ice thickness by performing embedding measurements on thinner ice, and found that when using CF_4 (<E> between 3 and 4.4 eV) and the Rh(111) substrate, ~130 ML D_2O films had 1.5-2 times as much CF_4 as the 750 ML films. Even at 375 ML, there was possibly a slight difference in the shape of the TPD spectra. Thicker ice gave the same result as for 750 ML, which determined the thickness used in these experiments. These observations go to the self-similar structure of thick versus thin films of ice. Two forms of sold water were grown, crystalline (CI) at a surface temperature of 140 K and amorphous solid water (ASW) at T_S = 120 K. At these growth conditions, the ice is not porous.[30–32]

High translational energy beams of CF_4 (Aldrich, 99.9%), SF_6 (Aldrich, > 99.75%), Xe (Airgas, 99.995%), or Kr (Praxair, Research Grade) were made by mixing <0.5 % (by volume) of the gas with either H_2 or He. The mixture was expanded through a 10 or 15 µm pinhole with several hundred psi of backing pressure. The nozzle temperature could be varied between 300 and 673 K. This resulted in energies as high as ~7 eV for Xe and slightly more than 5 eV for CF_4, with a $\Delta E/E \approx 0.16$. Energies were determined by measuring the time-of-flight of the incident atomic or molecular beams. This was accomplished by lowering the target and rotating the detector until it was directly in line with the beam. A rotating, slotted chopper wheel in the second differential pumping region modulated the beam, and the time for the gas to travel the distance to the detector was determined.

To estimate the flux, the first step was to use a neat beam of either CF_4 or Xe and measure the pressure rise in the UHV chamber with a nude Bayard-Alpert gauge calibrated for N_2. When corrected for the relative sensitivities, 2.31 for CF_4[33] or 2.8 for Xe,[34,35] and knowing the pumping speed, the number/sec of atoms or molecules entering the chamber could be determined. This measurement was used to calibrate a residual gas analyzer (RGA) that was not in the direct line of sight of the beam. With this calibration, and the size of the beam spot at the target crystal, it was possible to determine the flux for any of the seeded beams by using the RGA signal.

The substrate for the solid D_2O growth was a Rh(111) crystal that could be cryogenically cooled with either liquid N_2 or He, and resistively heated. This crystal was mounted on a rotatable manipulator so that the incident angle that the beam impinged on the surface could be varied. In the past, we would chemisorb a half monolayer of oxygen on the clean crystal and use this as the substrate.[10] For the experiments presented in the present paper, we determined that just flashing the crystal to ~ 350 K before the ice growth gave essentially the same results, and therefore the pre-deposition O_2 exposure is unnecessary and was omitted for the results presented here. Temperature (T_S) was measured with a chromel-alumel thermocouple welded to the Rh crystal. The readings are within 2 K, verified by checking the TPD results against the kinetic parameters of Smith et al.[28] For all of the high translational energy gas exposures, the ice was held at 120 K. TPD spectra were taken with the detector normal to the surface and with a temperature ramp rate of 10 K min^{-1}. The detector had an electron multiplier operated in pulse counting mode. The signal was collected by a counter in 1 sec bins. The m/e that the quadrupole passed was set by the voltage from a computer-controlled digital-to-analog converter. By changing the voltage at the end of each bin, it was possible to collect the results for different masses in consecutive bins. For all of the TPD spectra shown, there was signal collected for the mass of the embedded species (Xe or CF_4), as well as for the desorbing D_2O. For the Xe, the results are given in ML, where 1 ML = 6×10^{14} atoms cm^{-2}. This was calibrated by growing a single monolayer of Xe, and measuring the integrated TPD signal.[10] The sensitivity of the detector for CF_4 relative to Xe was determined from the flux measurements by comparing the signal from the straight through beam into the mass spectrometer with the RGA signal. For comparing with the Xe, the CF_4 results are also given in units of ML, with 1 ML = 6×10^{14} CF_4 molecules cm^{-2}.

B. RAIRS

Complementary sets of experiments on CF_4 embedding were performed in a separate molecular beam scattering instrument capable of monitoring changes in ice films with *in situ* RAIRS. The instrument has been described at length in previous publications.[2,36] Modifications relevant to these experiments are included herein.

Ice films were grown on a Au(111) single crystal housed inside the UHV chamber ($<1x10^{-9}$ Torr), secured to a temperature-controlled sample plate on the instrument's manipulator. All embedding experiments within the RAIRS instrument, unless elsewhere noted, were performed with the crystal held at 125 K as measured by a chromel-alumel thermocouple secured to the sample plate directly beside the crystal. The sample temperature was controlled with a combination of liquid nitrogen cooling and resistive heating of a filament located directly behind the sample. ASW ranging in thicknesses from 60 to 200 layers were grown on the crystal at 125 K by backfilling the chamber with D_2O vapor through a leak valve to a pressure of $\sim 1x10^{-7}$ Torr (~0.1 layers of D_2O s^{-1}).[27,30]

RAIRS was performed with *p*-polarized light from a commercial IR spectrometer (Nicolet 6700) directed onto the surface at 75 ° incidence, collected with a liquid nitrogen cooled MCT/A detector. All spectra were averages of 200 scans taken at 4 cm^{-1} resolution in reference to either the bare or ice-covered Au(111) crystal, with peaks fit to Gaussian line shapes atop cubic polynomial baselines using a nonlinear least-squares routine over the range of 1200 to 1350 cm^{-1}. Spectra of the films were acquired at least 30 minutes after closing the leak valve to eliminate background absorption during the remainder of the experiment, and quantified by integration of the total O-D signal located near 2600 cm^{-1}. Under these conditions, background adsorption was observed to be negligible over a period of hours. Confirmation of ASW growth is straightforward with RAIRS—the peak shapes are easily distinguished from crystalline films (CI) by inspection.[2,36,37]

CF_4 beams were produced by expanding a mixture of ≈ 1% CF_4 seeded in H_2 at a stagnation pressure of 300 psi through a 15 μm Pt pinhole. The nozzle could be resistively heated from room temperature to 700 K and the temperature was controlled by a Eurotherm 818 controller to maintain stable nozzle temperatures, and correspondingly stable CF_4 translational energies. The translational energy of CF_4 used in the RAIRS experiments ranged from 2.3 eV to 5.4 eV with a width ($\Delta E/E$) of 16% as measured by TOF techniques utilizing a mechanical chopper and an in-line mass spectrometer. In order to quantify the flux of each CF_4 mixture, the signal at $m/z = 69$ of the chamber's background gas analyzer was calibrated to that of a pure CF_4 beam. The flux of the pure beam was calculated from the pressure rise in the chamber as measured by an ionization gauge, taking into account the difference in electron ionization cross section of CF_4 relative to N_2.[38,39] Unless otherwise noted, the CF_4 impinged upon the ice surface at normal incidence.

4.3 Results and Discussion

A. Thermal Desorption

For the thermal desorption experiments, both CF_4 and Xe could be detected. Illustrative results are shown in Figure 4.1 for both ASW and CI for 30 minute exposures with nearly the same fluxes of either CF_4 or Xe. Figure 4.1(a) also shows the TPD results for ASW and CI D_2O. The ASW shows an initially faster desorption than CI, before the ASW converts to CI.[27] For the Xe,

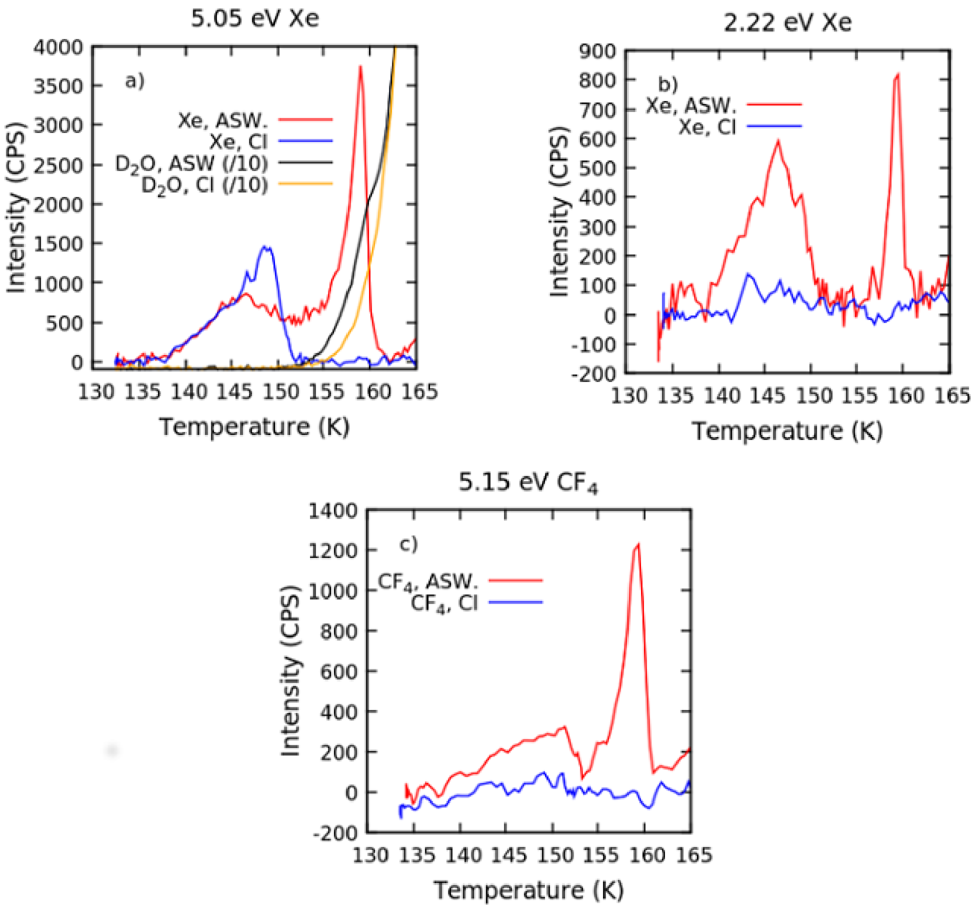

Figure 4.1. Example TPD spectra for CF$_4$ and Xe. For all of the TPD spectra, the ramp rate was 10 K/minute. The exposures were all done at $T_S = 120$ K, $\theta = 0^o$, and for 30 minutes. The fluxes were nearly identical: 1.0×10^{14} Xe atoms cm^{-2} s^{-1} for (a), 1.1×10^{14} Xe atoms cm^{-2} s^{-1} for (b), and 1.1×10^{14} CF$_4$ molecules cm^{-2} s^{-1} for (c).

Figures 4.1(a) and 4.1(b), the TPD spectra show two distinct features for embedding into ASW. The low temperature peak occurs before there is any measurable D_2O desorption. The higher temperature feature occurs where the D_2O desorption becomes appreciable. Since the exposures are nearly identical, it is clear that the embedding rate is directly related to the incident energy. For the CI, there is only one feature, which occurs at a temperature below that of any measurable D_2O desorption, and only for the higher incident energy. We also dosed ASW with 0.07 eV Xe. We only saw sticking at ~ 60 K, and all of the Xe desorbed at ~ 70 K. So, none of the features in the TPD spectra shown in this paper, where exposure was done at ~120 K, are from *adsorbed* Xe.

In previous papers, we also showed TPD spectra for Xe[3] and Kr.[10] The qualitative features are the same; there is a low and a high temperature feature for the ASW, with the high temperature feature occurring with the onset of appreciable D_2O desorption, and, in the case of Xe, just one feature for the CI which occurs at a temperature below which there is any significant D_2O desorption. The older Xe results show the low temperature feature extending to much higher temperatures than the spectra shown in Figures 4.1(a) and 4.1(b), but this is a result of the higher incident energy for the Xe and a much greater exposure (several thousand ML). In the previous paper on ballistic deposition,[3] we claimed that the high temperature TPD feature occurred at the ASW to CI transition. Re-examination has led us to the conclusion that the majority escapes before the transition, which is also the case for the data used for the present paper.

Figure 4.1(c) shows the results for CF_4 with the nearly same incident energy as the results for Xe shown in Figure 4.1(a). The results have been scaled by the difference in sensitivity between CF_4 and Xe. The exposures were nearly identical, so the intensities are directly comparable. For the ASW, there are the low and high temperature features in the TPD, though the low temperature feature is less distinct. This is qualitatively similar for the results using Kr,[10] which has a similar mass. As further supported in the plot of fraction embedded vs. incident energy shown in Figure 4.2, it is apparent that on ASW the CF_4 embedding rate is noticeably less than the Xe embedding rate. Furthermore, while Xe embedding was observed on CI, little to no CF_4 was observed to embed in CI.

Figure 4.2 show the initial embedding rate as a function of incident energy, all at $\theta = 0^o$. These are derived from the integrated TPD spectra after a long exposure. For Xe, the results in the previous paper[10] (Figure 4.10) showed that the amount absorbed rose to an asymptotic value. For the results shown in Figure 4.2, the total Xe exposure was less than 500 ML, which is still in an approximately linearly increasing part of the uptake curve.[10] Exposures for the CF_4 were similar, and as will be shown in the RAIRS section, are also linear over these exposures. It should be noted that these are total rates; as shown in a previous paper,[2] high energy Xe can slowly sputter the ice. At 2.2 eV the rate is negligible, only $6x10^{-5}$ D_2O molecules per incident Xe atom. However, at 5 eV, the rate increases to $4x10^{-3}$ D_2O molecules per incident Xe atom. For a Xe exposure of 500 ML, ~1 ML of D_2O would be sputtered from the ice surface.

As mentioned, the uptake of high energy Xe is approximately linear for low exposures. Figure 4.3 shows the TPD spectra for 5.11 eV Xe as a function of exposure. These TPD spectra were taken in two parts: the ice was heated to 145 K, which depleted the low temperature feature (shown in Figure 4.3(a)), and the sample was then cooled and the TPD repeated, *with no further Xe exposure,* to a much higher T_S so that all of the remaining Xe desorbed (shown in Figure 4.3(b)). The low temperature feature initially grows in very rapidly when exposure is begun, and then much slower after longer exposures. The higher temperature peak fills in at an approximately linear rate for these exposures. For the CF_4, the embedding rate is quite linear to high exposures. Figure 4.4

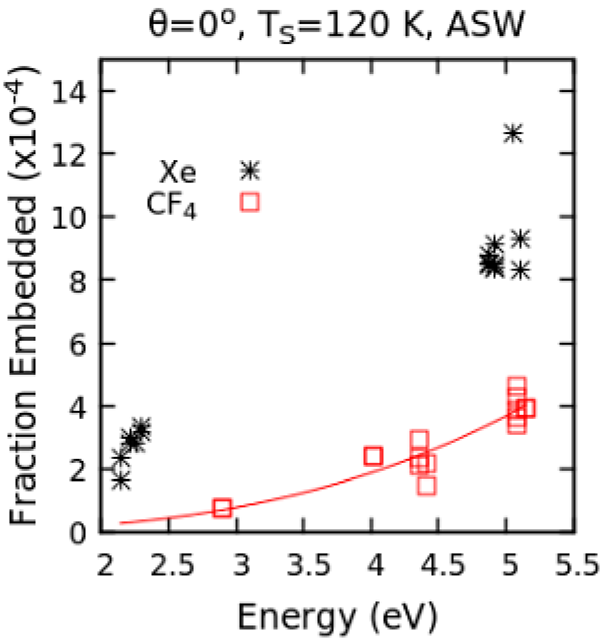

Figure 4.2. Uptake rates for CF_4 and Xe on ASW as a function of incident energy for T_S = 120 K and θ = 0 °. These were determined by integrating the TPD spectra after exposure.

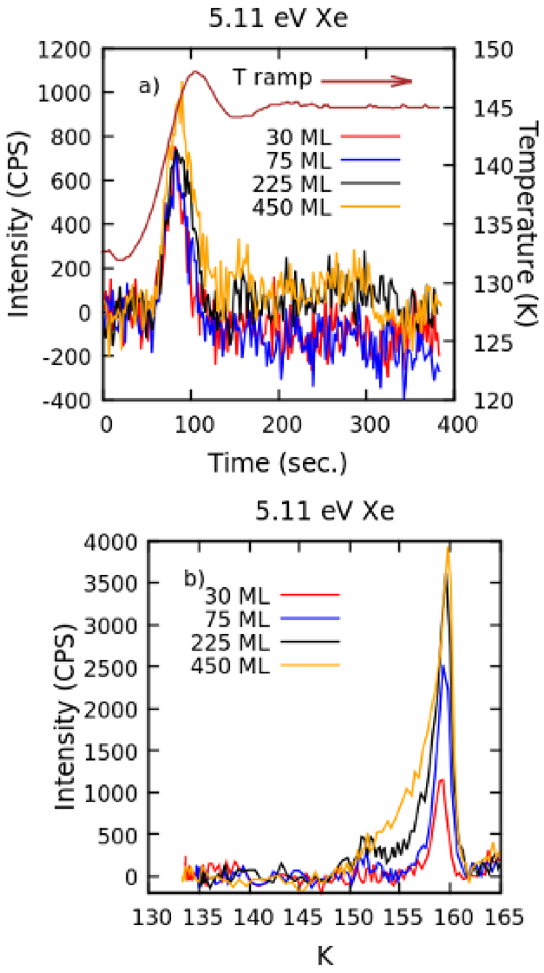

Figure 4.3. Annealing at 145 K to release low temperature Xe desorption. ASW was dosed with 5.11 eV Xe at θ = 0 °and T_S = 120 K. The Xe exposures are given in ML. The top figure (a) shows the Xe desorption as the ice is warmed to 145 K, and then held there for 300 s. The temperature profile is shown as the purple line against the right hand axis. After holding at 145 K, the ice was then cooled back to ≈ 130 K. The lower plot (b) shows the Xe desorption in a TPD experiment (ramp rate = 10 K min^{-1}) of the same ice sample as it is heated above 165 K, and clearly demonstrates that the high temperature Xe desorption is not depleted by annealing at 145 K, but the low temperature desorption is eliminated. The low temperature feature also saturates much faster than the high temperature desorption feature.

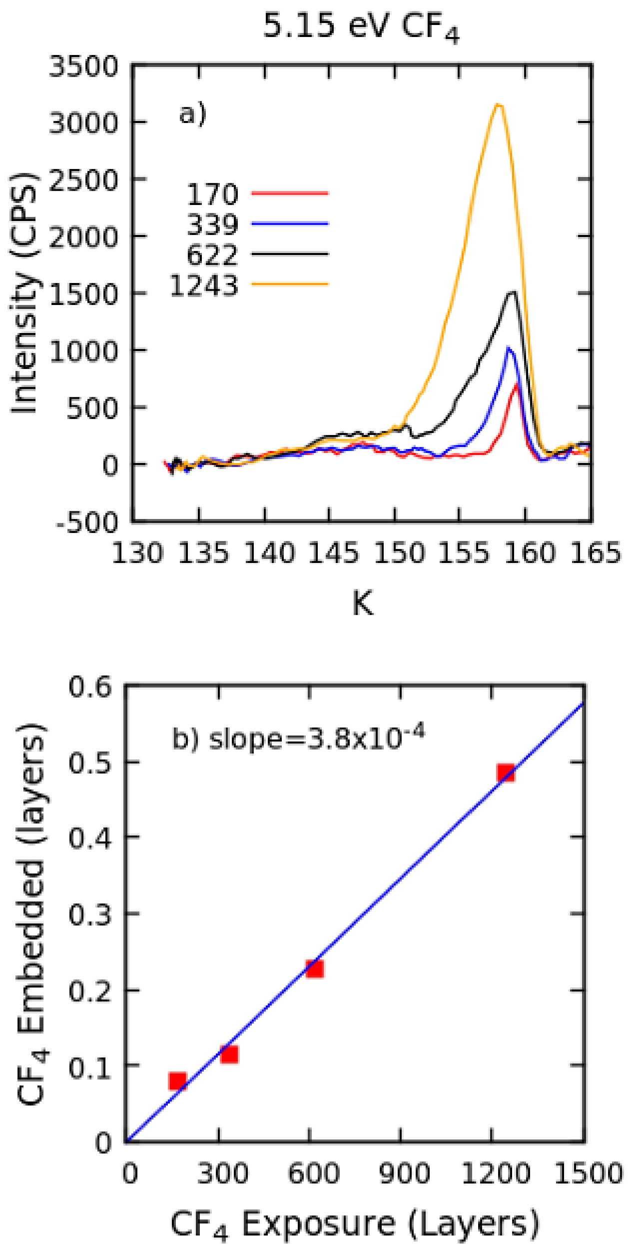

Figure 4.4. Panel a shows the TPD spectra for 5.15 eV CF_4 as a function of exposure in ML at θ = 0 ° and T_S = 120 K. Panel b shows the uptake rate derived from the integrated intensities of the TPD spectra.

shows the comparison of TPD spectra for different exposures. The CF_4 has a very intense IR signal, and the uptake will be discussed more thoroughly in the RAIRS section.

Both CF_4 and Xe show the low and high temperature features in the TPD for ASW. CI shows a similar low temperature desorption feature when exposed to high energy Xe. In previous papers,[10,24] we examined the scattering of rare gases (Xe and Kr) from both ASW and CI. These papers included realistic simulations, using as a model the {0001} surface of hexagonal ice. This model would most closely resemble the crystalline CI, so it is tempting to assign the low temperature desorption feature to processes determined by the simulations. Though ASW is much more disordered, ASW has a large degree of a similar short range order.[40] Some of the conclusions from the simulations were that at high energies and normal incidence, Xe could penetrate two or three water layers below the ice surface and become at least transiently trapped, exchanging most of the incident kinetic energy with the ice lattice. As the incident energy decreases, so does the average depth of penetration.

Much of the low temperature desorption occurs between 140 and 150 K. In this temperature range, we saw no measurable D_2O desorption. Using the Arrhenius parameters from Smith et al.,[28] the expected desorption rate for ASW is 1×10^{-3} ML s^{-1} at 140 K, and only 3×10^{-2} ML s^{-1} at 150 K. For CI, the desorption rates are even lower: 4×10^{-4} ML s^{-1} at 140 K and 1×10^{-2} ML s^{-1} at 150 K. The absorbed gas must be percolating up from the selvedge. By stopping the TPD at an intermediate temperature, it is possible to deplete the species that leads to the low temperature peak, without any appreciable change in the intensity of the higher temperature feature. Examples are shown for Xe in Figure 4.5 and CF_4 in Figure 4.6. Both of these are two part spectra like those of Figure 4.3. As shown in Figure 4.1(c), the low temperature feature for CF_4 extends to higher temperatures than is the case for Xe. This is also shown in a comparison of Figure 4.5 and 6; the

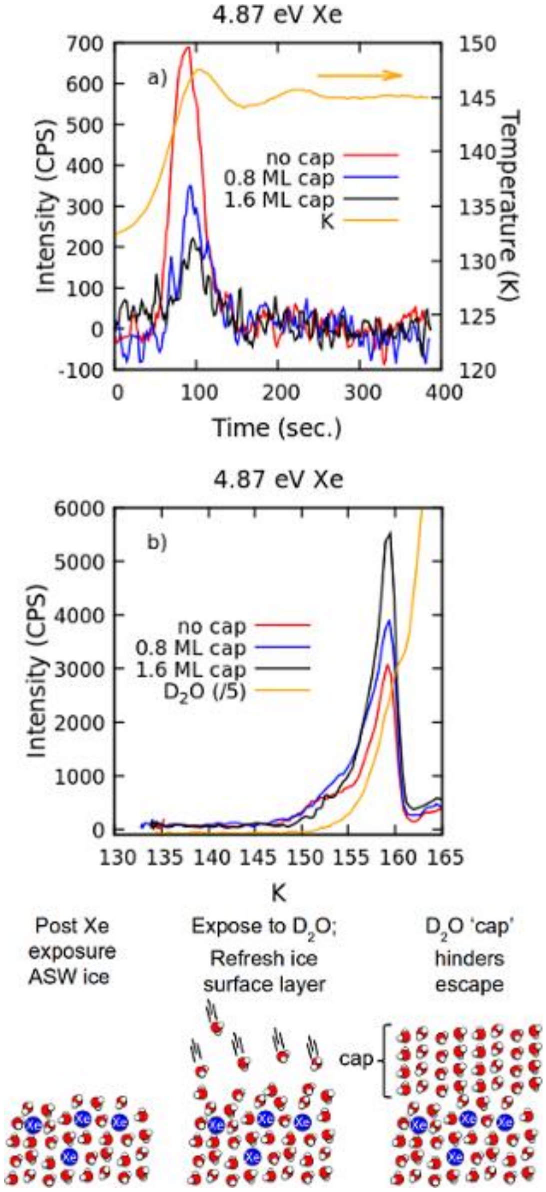

Figure 4.5. Capping experiments for Xe. ASW at T_S = 120 K was exposed to 4.9 eV Xe with a flux of 1.6×10^{14} atoms cm^{-2} s^{-1} for 30 minutes at $\theta = 0^o$. It was then beam dosed with the indicated amount of D_2O. The TPD spectra were taken in two parts, first to 145 K (a) (the temperature profile is also shown), and then cooled before another TPD spectra was taken to a temperature well past D_2O desorption (b).

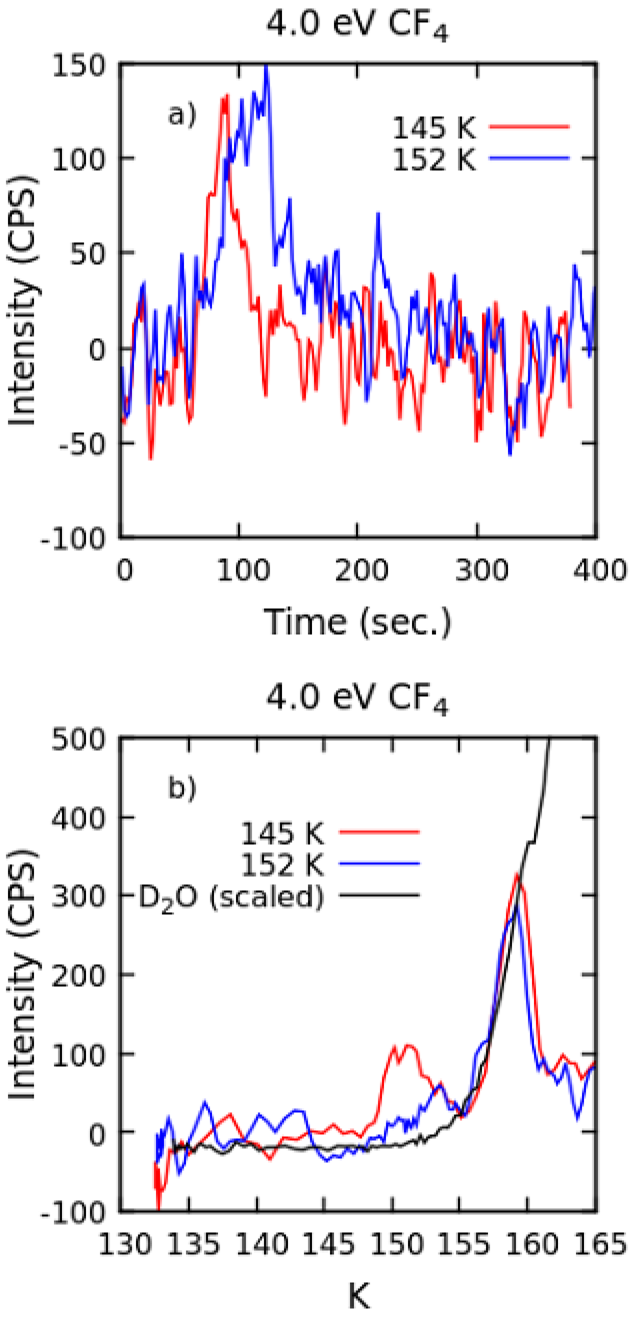

Figure 4.6. Two part TPD spectra for CF_4. ASW at T_S = 120 K was exposed to 4.0 eV CF_4 with a flux of 1.2×10^{14} CF_4 molecules cm^{-2} s^{-1} for 30 minutes at $\theta = 0^o$. The TPD spectra were taken in two parts, first to 145 K or 152 K (a), and then cooled before another TPD spectra was taken to a temperature well past D_2O desorption (b).

CF_4 dosed surface must be heated to a higher temperature to completely desorb the CF_4 from the absorption sites that lead to the low temperature TPD feature.

Also shown in Figure 4.5 are the results for experiments where the surface of ice, which already had embedded Xe, was exposed to a small amount of D_2O at $T_S = 120$ K before desorption. This additional water will ‘cap’ the ice surface embedded with Xe, further burying the implanted Xe, hindering its escape. Less than 2 ML of D_2O almost completely suppresses the low temperature desorption and most of the Xe desorbs at the high temperature. It should be noted that the time at which the peak desorption occurs does not change within our experimental error. Presumably, these observations indicate the Xe in this desorption channel exists just below the surface layer, and the top layer is perturbed enough that the molecules can rearrange at a relatively low temperature, and allow the Xe atoms to escape. Capping introduces an unperturbed overlayer, and the Xe stays trapped until the D_2O starts desorbing.

For the ASW, there is also a desorption peak that occurs concurrently with the desorption of appreciable amounts of D_2O. It is important to point out that this is not the “molecular volcano” that occurs at the ASW to CI transition,[41] but is trapped gas being released as the D_2O overlayers desorb. The peak in the CF_4 and Xe desorption occur between 159 and 160 K. By integrating the mass spectrometer signal at m/e = 20 of the D_2O TPD up to these temperatures, the amount of D_2O desorbed is between 2.5 and 4 ML. We do not know what the mobility of the Xe or CF_4 is as the temperature increases and the ice softens, but this result would suggest that the trapped Xe or CF_4 that leads to this desorption channel is only the equivalent of a few D_2O layers below the surface. This observation also qualitatively agrees with the simulations; some Xe can penetrate a few layers below the surface.

To summarize, we are assigning the low temperature TPD feature to gas absorbed just below the surface layer, and the higher temperature feature largely due to gas absorbed a few layers down. The simulations[24] showed that between 20 and 80% of the Xe could remain trapped inside the ice until the calculation was stopped at 6 ps. Our experiments last for many minutes, so it may be possible for the D_2O molecules to rearrange over a longer time scale and eventually eject the absorbed gas. Just such a process was seen for high energy Xe that penetrated an ordered 1-decanethiol monolayer.[42]

We do not know the nature of the different absorption sites which allow for the ASW to have absorption at apparently larger depths than CI, even at the highest translational energy of 5.2 eV with $\theta = 0^o$. One consideration in collisions is the momentum of the projectile. When the momentum of the Xe is lowered, it no longer absorbs into the CI. This is shown in Figure 4.1; 2.2 eV Xe has a lower momentum than 5.2 eV CF_4. To investigate further, we tried the experiments with SF_6, which is 1.11 times heavier than Xe. We prepared the SF_6 in H_2, and found that it was stable to at least a 473 K nozzle temperature. At 673 K, it decomposed in the hot stainless steel nozzle assembly. Results are shown in Figure 4.7 for an incident energy of 3 eV incident at $\theta = 0^o$ on ASW. There is no detectable desorbing SF_6 for exposures as great as those used for Xe and CF_4, at 2 or 3 eV on either ASW or CI, even at $\theta = 0^o$. At these energies, both Xe and CF_4 will at least absorb into ASW. One difference among these three molecules is their relative size. For a comparison, we estimated the sizes from the van der Waals gas constants.[43] The radii are 2.73 Å for Xe, 2.93 Å for CF_4, and 3.27 Å for SF_6. This suggests that the size has some effect. Possibly, the molecule interacts with a few more water molecules on the surface that prevents it from forming a path into the selvedge. Another possibility is that it does penetrate, but it perturbs the ice enough that it is rapidly expelled from the selvedge.

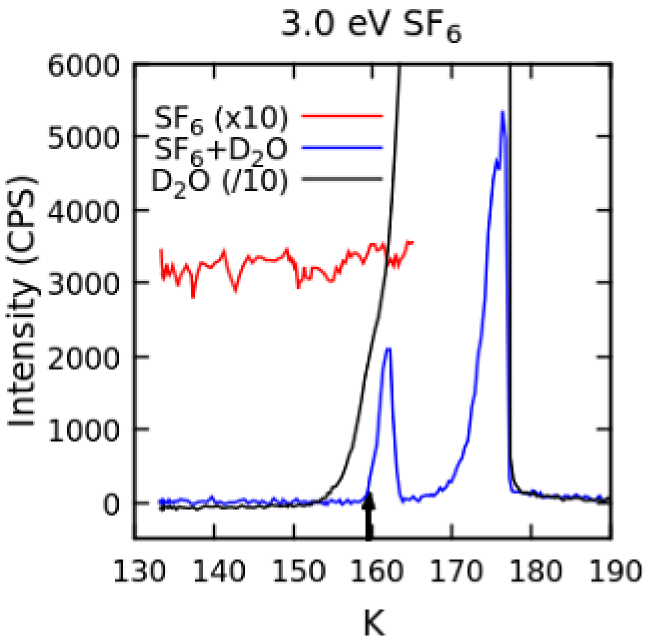

Figure 4.7. ASW was exposed to 3.0 eV SF_6 at T_S = 120 K and θ = 0° for 30 minutes. We did not explicitly measure the flux, but they should be similar to those for Xe and CF_4. The red line labeled SF_6 is the TPD of an experiment where the ASW was deposited (offset from 0 cps for clarity) first, and then the surface was exposed to the SF_6 beam (consecutive dosing). The blue line labeled SF_6 + D_2O is the TPD when the Rh(111) substrate was exposed to both the D_2O and SF_6 beams at the same time (concurrent dosing). The arrow indicates the peak position of the high temperature TPD feature in the embedding experiments with CF_4 and Xe.

Figure 4.7 also shows the results when the SF_6 and D_2O are dosed simultaneously. The D_2O flux was 0.45 ML s^{-1}, $\theta = 45^o$, and $T_S = 120$ K, where the deposited D_2O forms ASW. The SF_6 is entrapped throughout the ice, some comes out as a "molecular volcano", with one narrow desorption peak at the position of the ASW to CI transition, where the near surface molecules can escape as cracks form in the ice.[41] The more deeply absorbed SF_6 then desorbs in concert with the D_2O desorption. We show this experiment to demonstrate that we can easily detect SF_6, and also show that there is a fundamental difference between our ballistic absorption experiments, and the entrapping of gases with a large concurrent water flux.

The simulations[24] predict that the Xe penetration greatly decreases at more glancing incident angles. Figure 4.8 shows some results for 2.3 eV Xe and 5.2 eV CF_4 as a function of . The results show no major change until becomes quite glancing. It is worth noting that the surfaces showed no specular scattering of an 18 meV He beam, a strong indication that the surface is not flat on the molecular scale, so the local normal of the surface may be ill defined.

B. RAIRS

CF_4 uptake by ASW D_2O ice was confirmed with the reproducible appearance of peaks at 1276 and 1257 cm^{-1} upon exposure of the ice to the CF_4 beam at a variety of incident translational energies. An example of embedding with an incident CF_4 translational energy of 5.3 eV is detailed in Figure 4.9. Observed peak locations correspond to the Fermi resonance of the v_3 asymmetric stretch and the first overtone of the v_4 deformation. The peaks are red-shifted from the gas phase values (1283 and 1261 cm^{-1}, respectively),[44,45] a phenomenon often observed for species physically adsorbed to or bound within an inert matrix.[46] These values are not red-shifted towards values observed for condensed phases with significant CF_4-CF_4 intermolecular interaction,[46,47] and thus the CF_4 molecules are sparsely dispersed amongst the D_2O molecules in the ice film. We did not

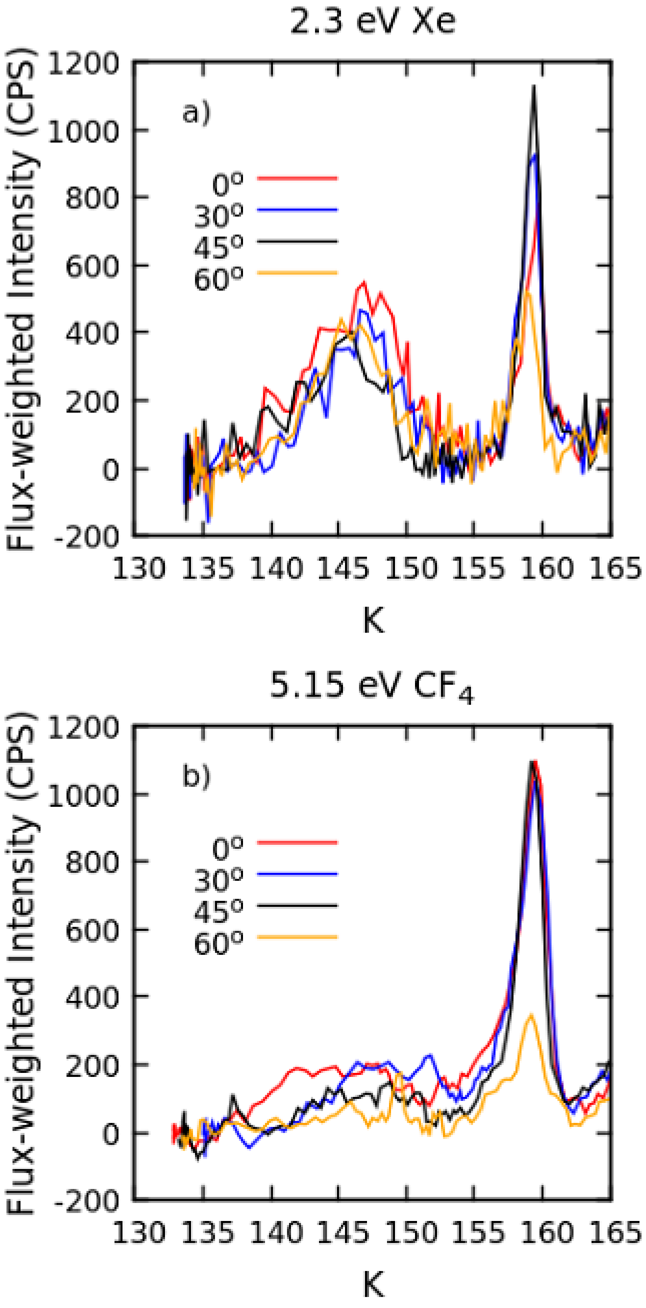

Figure 4.8. TPD spectra for exposures at different θ. All are for ASW at T_S = 120 K. Results have been corrected for flux, which changes by 1/cos(θ), either by adjusting the dosing time or the intensity.

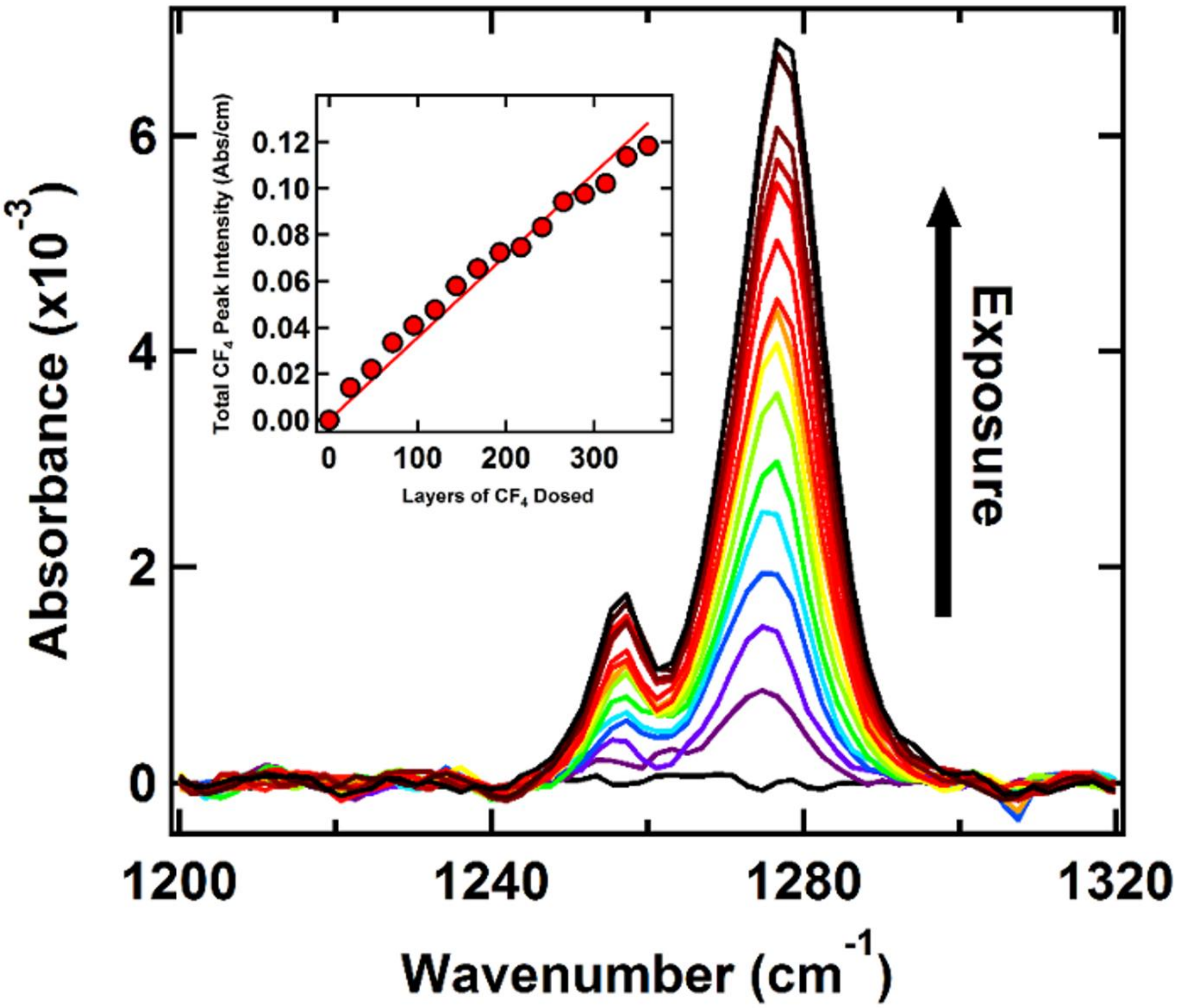

Figure 4.9. Energetic ballistic deposition of 5.3 eV CF_4 into ASW ice is characterized by the appearance of RAIRS peaks at 1276 and 1257 cm^{-1}, the intensity of which increases linearly with respect to the total amount of CF_4 dosed onto the surface at normal incidence. Inset graph details the linear dependence, the slope of which is taken as the initial rate of embedding into 60 layers of ice.

look for any decomposition. The C-F bond energy is 5.7 eV[48], as high or higher than the average translational energies we investigated. Also, from our scattering experiments[24], we know that the ice is good at adsorbing the translational energy of the incoming projectile. Thus, it is unlikely the CF_4 decomposed.

Given that sticking is observed to be negligible at this temperature, we infer that the mechanism behind CF_4 uptake is that of energetic ballistic deposition, akin to what has been previously observed for Kr and Xe in H_2O and D_2O ices.[3,10] However, there are several instances of deviation from embedding of rare gases. From Figure 4.10, for example, CF_4 embedding at 3.8 eV was not observed to saturate after more than ten thousand layers of CF_4 were dosed. This distinctly contrasts the case of rare gas embedding, where saturation occurred after dosing only four thousand layers of either Kr or Xe embedding into ASW and CI crystalline ices.[10] In the same study, it was observed that ~3 eV Kr and Xe deposition saturated near a total uptake of ~0.5 layers. For purposes of comparison to the Xe data, we have related the total CF_4 flux to a measure of "layers of CF_4" by approximating the packing density of a CF_4 monolayer as being comparable to that of Xe given its similar size. Given the comparable size of CF_4 to Kr and Xe, as well as the similar energy used in the saturation experiment detailed in Figure 4.10, we make the assumption that CF_4 saturates at this same level; the CF_4 molecules' access below the second ice layer is not probable. Applying a simple Langmuir adsorption treatment to the data (see inset of Figure 4.10), the IR intensity can be expected to saturate at 0.18 ± 0.01 for 3.8 eV CF_4 under current instrumental conditions, and we take this intensity to be that of a half-monolayer, yielding a conversion factor for the IR data of 2.8 ± 0.2 layers per integrated absorbance unit.

The initial rates for CF_4 embedding are observed to be linear in all cases, with observable embedding occurring above a translational energy threshold near ~3.0 eV, as determined by

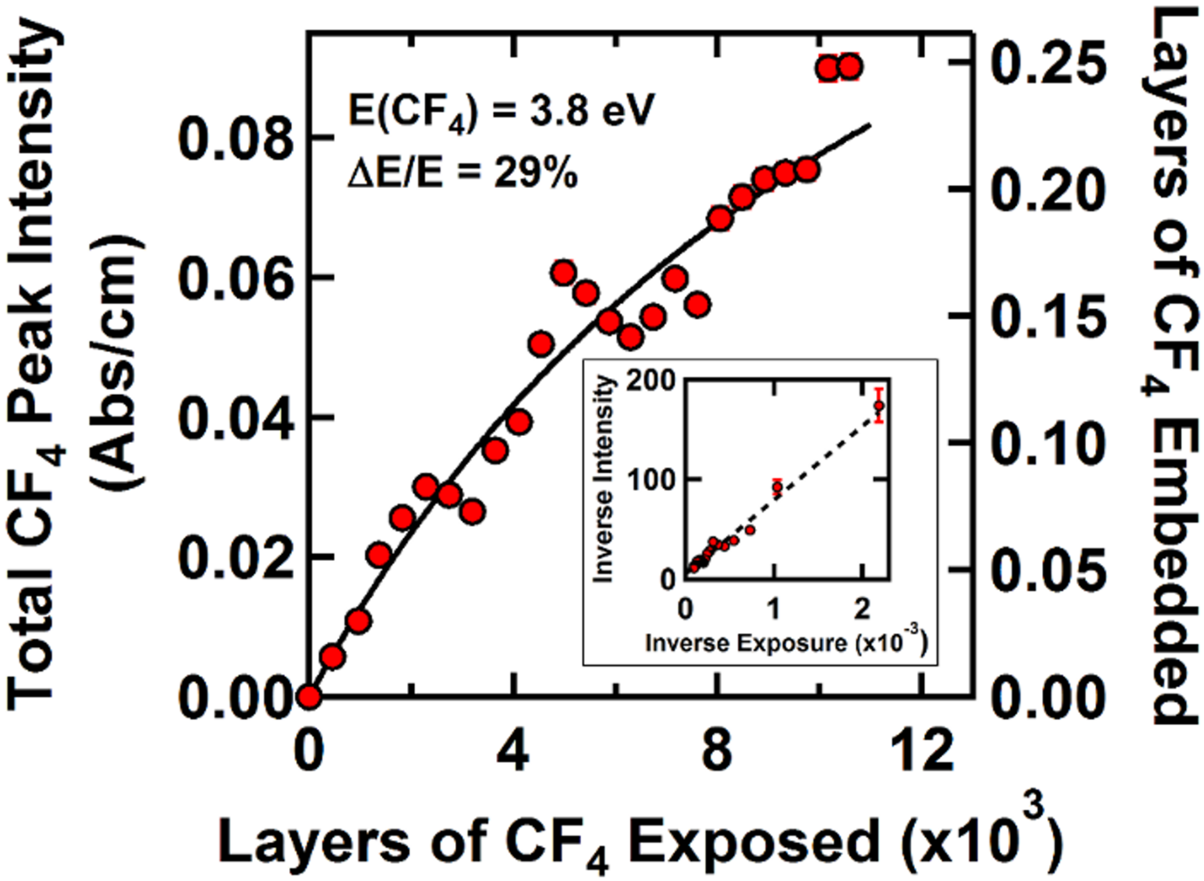

Figure 4.10. Total CF$_4$ in the ice is not observed to saturate after exposure to more than ten thousand layers of CF$_4$ as measured by RAIRS, in contrast to the trend observed with rare-gas-embedding which saturates by four thousand layers of exposure in both ASW and CI ice films. The curved solid line is the Langmuir isotherm fit to the data as determined by a linear least-squares fit shown in the figure's inset. The saturation experiments were performed with a 30 µm nozzle at 120 psig in order to maximize CF$_4$ flux, which in turn yielded a larger incident CF$_4$ energy distribution of 29%. Error bars (where visible) indicate one standard deviation with respect to the integration of peaks fit to the IR data.

RAIRS. As the CF_4 energy is increased from this critical embedding energy, the embedding rate is observed to monotonically increase for energies up to at least 5.7 eV, as detailed in Figure 4.11. It is important to note that the measured rates represent that of an ensemble of CF_4 molecules with incident energy distributions centered about the quoted values, which must be deconvoluted. To extract the true energy dependence of the embedding rate from the data, a polynomial nonlinear least-squares fit to the data, $f(E)$, was employed as an ansatz for the actual rate dependence and deconvoluted from the incident energy distribution, $P(E)$, to give the measured dependence, $F(E)$, as plotted in Figure 4.11:

$$F(E) = \int f(E)\, P(E)\, dE \tag{4-1}$$

In this case, deconvolution yields a curve nearly identical to the experimental curve, likely due to consecutive data points being spaced apart by an amount similar to the typical energy distribution width. Additionally, data derived from the independent TPD experiments are qualitatively consistent with the curve determined by RAIRS, lending credence to the fidelity of the results overall.

C. Comparison of the Results

Figure 4.12(a) shows a summary of results for the rare gases Kr and Xe from TPD experiments, as previously reported.[10] These data show that the initial uptake rate has the general trends already discussed; the rate of embedding increases with energy, and for the same incident energy, the higher mass has the higher rate. In addition, these experiments show that as the amount of absorbed atoms increases, the rate decreases and seems to be reaching a plateau at ~1ML of absorbed gas. The densities of ASW and CI are rather similar, so it is reasonable that the number density of water molecules per unit volume are similar for the two morphologies; in that case, with the embedded gas evenly distributed throughout the top 4 layers, the concentration is a rather

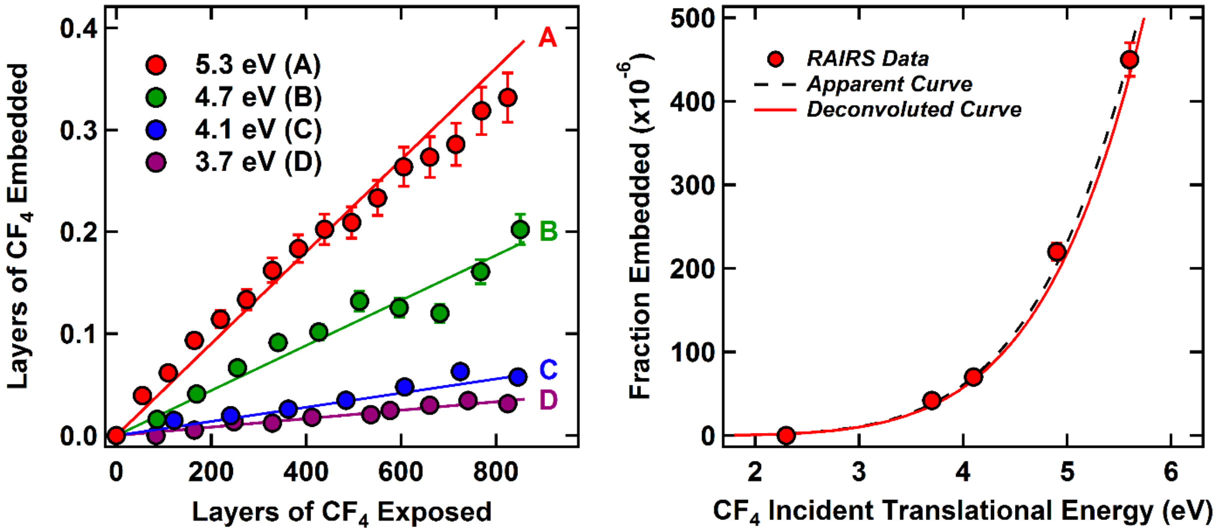

Figure 4.11. Representative initial embedding fractions of CF_4 into 60 layers of ASW D_2O ice as measured by RAIRS (*left*). In all cases, uptake was observed to be linear, with higher rates observed for higher-energy CF_4. Error bars (where visible) take into account both the error in the conversion factor and one standard deviation with respect to the integration of peaks fit to the IR data. The energy dependence of embedding rate (*right*): dashed line indicates the polynomial fit to the apparent dependence derived from experimental data (solid circles), solid line indicates deconvoluted fit (see text). Embedding of CF_4 is only observed to occur above a threshold near ~3.0 eV. Error bars (where visible) represent 95% confidence intervals for the linear fits.

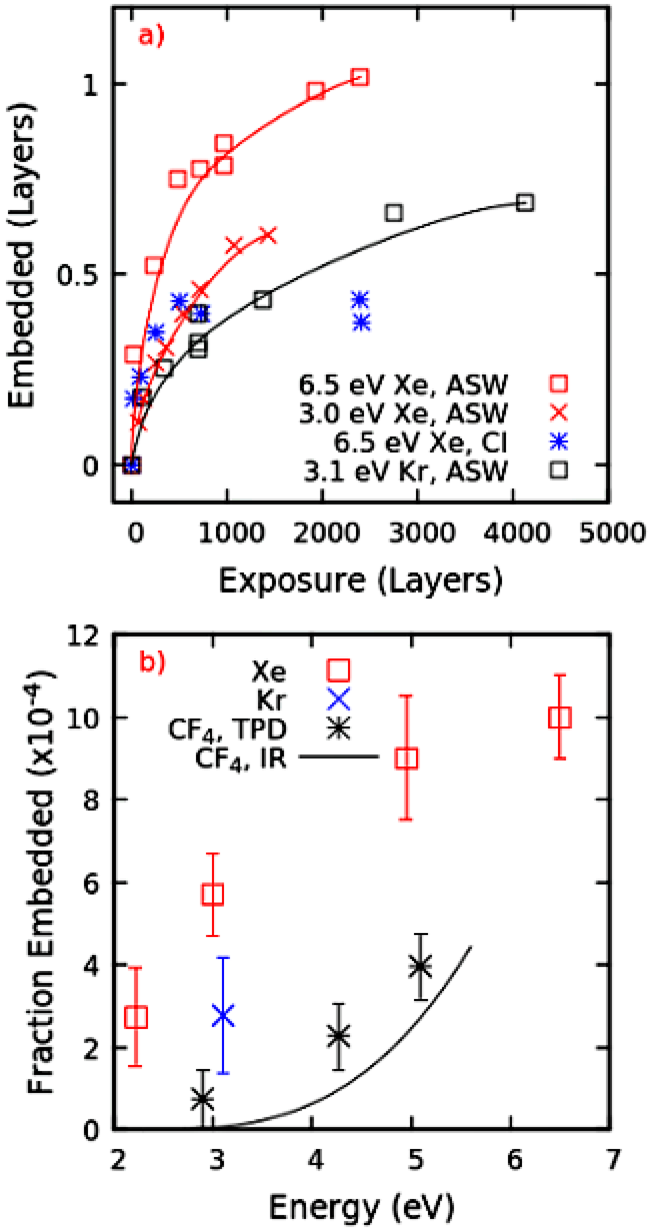

Figure 4.12. Figure 12(a) shows the layers of embedded rare gas as a function of exposure (from Gibson et al.[10]). Figure 12(b) is the initial uptake rate as a function of energy. The line for the CF_4 IR results is the fit shown in Figure 4.11.

considerable 10%. Figure 4.12(b) shows the initial uptake rate as a function of incident energy. The rare gas data are taken from the results shown in Figure 4.2 and by straight line fits of the low exposure sections of the uptake curves in Figure 4.12(a). There is a slight difference between the IR and TPD results, but the agreement is very good considering the different experimental methods and the approximations that went into estimating absolute values of the flux and coverage. What is clear is the large difference in the initial embedding rate for Xe and CF_4

4.4 Conclusions

Our previous papers showed that high energy rare gases could be embedded in ice.[3,10,24] The rate of embedding and the final amount embedded appears to be dependent upon both the energy and mass of the projectile, though always rather small. The rate decreases as gas is embedded, with the asymptotic value increasing for greater energy and mass, possibly because the atoms can penetrate further into the bulk. The TPD results for the embedding of Xe in CI vary from those for ASW, as most of the embedded Xe escapes at a temperature below any appreciable water desorption.

This paper expands on those observations, using both TPD and RAIRS experiments. We looked at three inert projectiles: Xe, CF_4 and SF_6. Using TPD experiments, we showed that for Xe and CF_4, the embedded gas that escapes at the lowest temperatures appears to be absorbed just below the surface. The remaining embedded gas escapes as the water desorbs, with the majority coming off by the time the equivalent water desorption is 2.5-4 layers of hexagonal ice. This is in agreement with scattering calculations for Xe from the surface of hexagonal ice.[24] The embedding rate of CF_4 (2/3 the mass of Xe) in ASW is always much lower than Xe at the same incident energy. CF_4 does not embed in CI at even the highest observed energies (~5.7 eV).

We explored the embedding of SF_6 into ASW by exposing the ice to an SF_6 beam with a translational kinetic energy of 3 eV. This is slightly more massive than Xe (146 g mol^{-1} vs. 132 g mol^{-1})), but there was no indication of any embedding into ASW, even though this is approximately the lowest energy for detecting CF_4 embedding, and Xe definitely embeds. One difference between SF_6 and the other gases is its van der Waals radius; it is significantly larger. Possibly, the larger size perturbs the surrounding water molecules enough that it is pushed out by rearranging molecules, as was observed for high energy Xe penetrating below the surface of a self-assembled monolayer.[42]

The results discussed in this paper have expanded significantly on the previous experimental and theoretical work. We know from calculations[10,24] for high energy Xe impinging on hexagonal ice that the Xe can penetrate several layers below the surface, and remain trapped for significant lengths of time. The depth of deepest penetration decreases with decreasing incident energy.[24] This could help explain why the final amount of embedded Xe is less for 3.0 eV than 6.5 eV; the higher energy Xe penetrates deeper into the selvedge. A similarly sized but less massive inert projectile. CF_4, also embedded, but at a much slower rate. A heavier, but also larger projectile, SF_6, did not embed. These results offer tantalizing clues as to the nature of the embedding of gases into ice. There is also the difference between CI and ASW results, which indicate fundamental differences between the near surface structures of these two forms of ice.

These results show that energetic ballistic embedding in ice is a general phenomenon for both atomic and molecular species, and represents a significant new channel by which incident species can be trapped under conditions where they would otherwise not be bound stably as surface adsorbates. These findings have implications for many fields including environmental science, trace gas collection and release, and the chemical composition of astrophysical icy bodies in space.

4.5 Acknowledgments

This work was supported by the Defense Threat Reduction Agency (DTRA) under Grant HDTRA1-11-1-0001. Additional support came from the Air Force Office of Scientific Research Grant FA9550-10-1-0219. Infrastructure support from the NSF-Materials Research Science and Engineering Center at the University of Chicago is also gratefully acknowledged.

References

1. Bar-Nun, A.; Notesco, G; Owen, T. *Icarus* **2007,** 190, 655.
2. Killelea, D.R.; Gibson, K.D.; Yuan, H.; Becker, J.S.; Sibener, S.J. *J. Chem. Phys.* **2012,** 136, 144705.
3. Gibson, K.D.; Killelea, D.R.; Becker, J.S.; Yuan, H.; Sibener, S.*J. Chem. Phys. Lett.* **2012,** 531, 18.
4. Strazzulla, G.; Leto, G;. Gomis, O.; Satorre, M.A. *Icarus* **2003,** 164, 163.
5. Gomis, O.; Satorre, M.A.; Strazzulla, G.; Leto, G. *Planet.* Space Sci. **2004,** 52, 371.
6. Strazzulla, G.; Baratta, G.A.; Leto, G.; Gomis, O.; *Icarus* **2007,** 192, 623.
7. Strazzulla, G. Nucl. Instrum. Methods Phys. Res. B **2011,** 269, 842.
8. Yokochi, R.; Marboeuf, U.; Quirico, E.; Schmitt, B. *Icarus* **2012,** 218, 760.
9. Karasek, F.W.; Clement, R.E.; Sweetman, J.A. *Anal. Chem.* **1981,** 53, 1051A.
10. Gibson, K.D.; Killelea, D.R.; Yuan, H.; Becker, J.S.; Pratihar, S.; Manikandan, P.; Kohale, S.C.; Hase, W.L.; Sibener, S.J. *J. Phys. Chem. C* **2012,** 116, 14264.
11. A’Hearn, M.F.; Feaga, L.M.; Keller, H.U.; Kawakita, H.; Hampton, D.L.; Kissel, J.; Klaasen, K.P.; McFadden, L.A.; Meech, K.J.; Schultz, P.H.; Sunshine, J.M.; Thomas, P.C.; Veverka, J.; Yeomans, D.K.; Besse, S.; Bodewits, D.; Farnham, T.L.; Groussin, O.; Kelley,

M.S.; Lisse, C.M.; Merlin, F.; Protopapa, S.; Wellnitz, D.D. Astrophys. J**. 2012,** 758:29, 1.

12. Notesco, G.; Bar-Nun, A.; Owen, T. *Icarus* **2003,** 162, 183.
13. Owen T.; Bar-Nun, A. *Icarus* **1995,** 116, 215.
14. Burke D.J.; Brown, W.A. Phys. *Chem. Chem. Phys.* **2010,** 12, 5947.
15. Ehrenfreund P.; Charnley, S.B. *Annu. Rev. Astron. Astrophys.* **2000,** 38, 427.
16. Brewer, P.G.; Orr, F.M.; Friederich, G.; Kvenvolden, K.A.; Orange, D.L. *Energy Fuels* **1998, 12,** 183.
17. Krauss C.; Saulny, S. *N. Y. Times* p. A12 (May 11, 2010).
18. McNutt, M.K.; Camilli, R.; Crone, T.J.; Guthrie, G.D.; Hsieh, P.A.; Ryerson, T.B.; Savas, O.; Shaffer, F. *Proc. Natl. Acad. Sci. U. S. A.* **2012,** 109, 20260.
19. Wuebbles D.J.; Hayhoe, K. *Earth-Sci. Rev.* **2002,** 57, 177.
20. Bousquet, P.; Ciais, P.; Miller, J.B.; Dlugokencky, E.J.; Hauglustaine, D.A.; Prigent, C.; Van der Werf, G.R.; Peylin, P.; Brunke, E.G.; Carouge, C.; Langenfelds, R.L.; Lathiere, J.; Papa, F.; Ramonet, M.; Schmidt, M.; Steele, L.P.; Tyler, S.C.; White, J. *Nature* **2006,** 443, 439.
21. Macdonald, G.J. *Clim. Change* **1990,** 16, 247.
22. Toon, O.B.; Turco, R.P.; Jordan, J.; Goodman, J.; Ferry, G. *J. Geophys. Res.***1989,** 94, 380.
23. Turco, R.P.; Toon, O.B.; Hamill, P. J. *Geophys. Res. - Atmospheres* **1989,** 94, 16493.
24. Pratihar, S.; Kohale, S.C.; Yang, L.; Manikandan, P.; Gibson, K.D.; Killelea, D.R.; Yuan, H.; Sibener, S.J.; Hase, W.L. *J. Phys. Chem. C* **2013,** 117, 2183.
25. Graham A.P.; Toennies, J.P. *J. Chem. Phys.* **2003,** 118, 2879.
26. Smith, R.S.; Huang, C.; Wong, E.K.L.; Kay, B.D. *Surf. Sci.* **1996,** 367, L13.
27. Speedy, R.J.; Debenedetti, P.G.; Smith, R.S.; Huang, C.; Kay, B.D. *J. Chem. Phys.* **1996,**

105, 240.

28. Smith, R.S.; Matthiesen, J.; Knox, J.; Kay, B.D. *J. Phys. Chem. A* **2011,** 115, 5908.
29. Gibson, K.D.; Viste, M.; Sibener, S.J. *J. Chem. Phys.* **2000,** 112, 9582.
30. Brown, D.E.; George, S.M.; Huang, C.; Wong, E.K.L.; Rider, K.B.; Smith, R.S.; Kay, B.D. *J. Phys. Chem.* **1996,** 100, 4988.
31. Stevenson, K.P.; Kimmel, G.A.; Dohnálek, Z.; Smith, R.S.; Kay, B.D. *Science* **1999,** 283, 1505.
32. Kimmel, G.A.; Dohnálek, Z.; Stevenson, K.P.; Smith, R.S.; Kay, B.D. *J. Chem. Phys*. **2001,** 114, 5295.
33. U.S. Department of Commerce, N. NIST: Electron-Impact Cross Section Database http://www.nist.gov/pml/data/ionization/index.cfm (accessed Jun 11, 2014).
34. Nakao, F. *Vacuum* **1975,** 25, 431.
35. Baskin Y; Meyer, L. *Phys. Rev.* **1955,** 100, 544.
36. Gibson, K.D.; Killelea, D.R.; Yuan, H.; Becker, J.S.; Sibener, S.J. *J. Chem. Phys.* **2011,** 134, 034703.
37. Smith, R.; Zubkov, T.; Kay, B. D. *J. Chem. Phys.* **2006,** 124, 114710.
38. Ma, C.; Bruce, M.R.; Bonham, R.A. *Phys. Rev. A* **1991**, 44, 2921.
39. Itikawa, Y. *J. Phys. Chem. Ref. Data* **2006,** 35, 31.
40. Bowron, D.T.; Finney, J.L.; Hallbrucker, A.; Kohl, I.; Loerting, T.; Mayer, E.; Soper, A.K. *J. Chem. Phys.* **2006,** 125, 194502.
41. May, R.A.; Smith, R.S.; Kay, B.D. *J. Chem. Phys.* **2013**, 138, 104501.
42. Gibson, K.D.; Isa, N.; Sibener, S.J. *J. Phys. Chem.* A **2006,** 110, 1469.
43. Reid, R. C.; Prausnitz, J. M.; Poling, B. E. *The Properties of Gases and Liquids, Fourth*

Edition, (McGraw-Hill, New York, N.Y., 1987).

44. Woltz P.J.H.; Nielsen, A.H. *J. Chem. Phys.* **1952,** 20, 307.
45. Jones, L.H.; Kennedy, C.; Ekberg, S. *J. Chem. Phys.* **1978,** 69, 833.
46. Byl, O.; Kondratyuk, P.; Forth, S.T.; FitzGerald, S.A.; Chen, L.; Johnson, J.K.; Yates, J.T. *J. Am. Chem. Soc.* **2003,** 125, 5889.
47. Fournier, R.P.; Savoie, R.; Bessette, F.; Cabana, A. *J. Chem. Phys.* **1968,** 49, 1159.
48. McMillen D.F.; Golden, D.M. *Annu. Rev. Phys. Chem.* **1982,** 33, 493.

CHAPTER 5

CAPTURE OF HYPERTHERMAL CO_2 BY AMORPHOUS WATER ICE VIA MOLECULAR EMBEDDING

The data presented in this chapter was previously published in the Journal of Physical Chemistry A. The following content was reprinted with permission from [Wenxin Li, Grant G. Langlois, K. D. Gibson, and S. J. Sibener, "Capture of Hyperthermal CO_2 by Amorphous Water Ice via Molecular Embedding" J. Phys. Chem. C, DOI 10.1021/jp504466r (2015).] Copyright 2015, American Chemical Society.

We present the first study detailing the capture and aggregation of hyperthermal CO_2 molecules by amorphous solid water (ASW) under ultra-high vacuum conditions at 125 K, near the amorphous/crystalline transition. Using time-resolved in situ reflection-absorption infrared spectroscopy (RAIRS), CO_2 molecules with translational energies above 3.0 eV are observed to directly embed underneath the vacuum-solid interface to become absorbed within the ice films despite an inability to adsorb at 125 K; this behavior is not observed for crystalline films. Upon embedding, the mobility of CO_2 within 125 K amorphous ice and the strength of its intermolecular interactions result in its segregation into clusters within the ice films. Tracing the kinetics of CO_2 embedding events under different energetic conditions allows for elucidation of the underlying dynamics, and we draw comparison with other projectiles we have studied to promote generalized conclusions in regards to empirical prediction of a projectile's embedding probability. Through application of a classical model of the entrance barrier for projectiles colliding with amorphous ice, we provide direct evidence for a unified connection between embedding probability and projectile momentum; an account of all embedding data measured by our group traces a unified barrier model. This work highlights the interplay between translational energy and momentum accommodation during collisions with ice in high speed gas flows.

5.1 Introduction

The interaction of gases with ice is fundamental to numerous scientific disciplines. In astrophysics, delivery of volatile species from comets theories of atmospheric formation on planets and moons focus primarily on delivery of volatile species from comets.[1-4] Simple gaseous species accumulate and concentrate within the ices of comets and pre-cometary matter,[5,6] potentially subject to bombardment by high-energy electromagnetic radiation and interstellar matter to form complicated molecules.[7] Simulation of these processes in many laboratories using pre-mixed cometary ice analogs has produced organic residues containing molecules potentially important in understanding possible sources of prebiotic chemistry on Earth.[8-14] Additionally, answers to important questions related to geophysics and global energy issues are built upon the foundation of a thorough understanding of gas-ice interactions, with intense focus on clathrate hydrates,[15,16] whose contemporary applications include endeavors into hydrogen storage[17,18] and capture of anthropogenic greenhouse gases.[19,20]

CO_2—along with its interaction with ice—represents a major constituent of interstellar matter,[21,22] and is hypothesized to be a major component of global climate forcing. Comparison between the sequestration and release of CO_2 by glacial ice during prior geological epochs and the current global climate provides tangible links to consequences associated with Earth's currently melting permafrost.[23,24] In this work, we present the first study on the capture and concentration of neutral, hyperthermal CO_2 by amorphous solid water (ASW) under ultra-high vacuum (UHV) conditions at a surface temperature where CO_2 adsorption is infeasible as a method of accretion. We demonstrate that the observed CO_2 uptake by ASW at 125 K is dominated by the process of energetic ballistic deposition, or "embedding." This is a phenomenon we have described at length in previous publications, whereby small atoms and molecules with high translational energies and trajectories near normal incidence directly bury underneath the vacuum-solid interface upon collision.[25-28]

Finally, we draw comparisons between the observed embedding efficacy of CO_2 in amorphous water ice and the other gaseous projectiles studied by our group—Xe, Kr, CF_4, SF_6—and *via* application of a classical empirical model to the activated process, firmly establish a generalized connection between projectile momentum and embedding probability.

The embedding of CO_2 and other small atoms and molecules into ASW inherently differs from percolation into the bulk following adsorption onto an icy surface, which itself is well characterized.[5,6,29-33] Namely, our results imply that ice composition can be modified by gases with high translational energies, even when ice temperature precludes adsorption.[7,8] These findings have direct implications in studies of planetesimals travelling at high speeds in protoplanetary nebulae,[34] and in studies and simulations of the hazardous icing of aircraft during flight.[35,36]

5.2 Experimental

The experiments referenced herein were conducted in a molecular beam scattering instrument described at length in a previous publication.[37] The instrument consists of a triply-differentially-pumped supersonic molecular beam connected to an ultra-high vacuum (UHV) chamber equipped, in part, with optics for performing time-resolved reflection-absorption infrared spectroscopy (RAIRS).

Ice coverage and CO_2 uptake in all experiments were quantified by integrating RAIR spectra by fitting observed bands with Gaussian peaks atop cubic baselines. All spectra were obtained using a Nicolet model 6700 infrared spectrometer with incident *p*-polarized IR radiation reflected from the underlying Au(111) crystal at an incident angle of 75° and directed into a liquid-nitrogen-cooled MCT/A detector. Spectra were averaged over 250 scans taken at 4 cm^{-1} resolution with clean Au(111) as background. Sixty to seventy-five layers (one layer = 1.07×10^{15} H_2O molecules[38,39]) of amorphous ice were deposited onto single-crystal Au(111) at 125 K, promoting both substrate independence and homogeneity; *i.e.*, self-similar structural presentation for layers of this thickness, at the vacuum-solid interface.[39,40] Under these conditions, the sticking coefficient of H_2O on both Au and ice is nearly unity,[37] and H_2O desorption is negligible over a period of hours. Ice thickness was quantified by backfilling the main chamber at a known deposition rate with respect to the Au(111) surface and correlating the rate with growth of the integrated intensity of the ~3300 cm^{-1} OH band.[41] This quantitation is valid with ice film thicknesses up to 200 layers using our setup due to optical field penetration, after which the OH band shape changes significantly.

In order to produce the highest possible CO_2 translational energies in our beam, we expand ~1% CO_2 diluted in H_2 at 400-600 psi through a 15 μm molybdenum pinhole, with all exposure to ice at normal incidence. CO_2 translational kinetic energies ranging from 0.9 eV to 4.1 eV are obtainable by resistively heating the beam nozzle from room temperature to 1200 K, with energy distribution widths ($\Delta E/E$) ranging from 18-46% depending upon nozzle temperature, as characterized using time-of-flight techniques. We note that this method of producing CO_2 with high translational energies causes CO_2 and H_2 to readily react under some of the chosen conditions—to near completion as the nozzle temperature approaches 1200 K at all stagnation pressures used—producing CO and H_2O through the reverse water-gas shift reaction[42] either homogeneously or catalyzed by the exposed metal surfaces. Similar beam reactivity phenomena were reported by Herschbach *et al.* in the case of small hydrocarbons forming larger hydrocarbons within the nozzle of a molecular beam under analogous conditions.[43] We plan to present the specifics of these interesting findings in an upcoming publication. While no evidence of CO accumulation is observed on or within the ice surfaces discussed in this paper, H_2O is deposited throughout our experiments with a rate typically at or below ~10^{-2} layers per second as a product of the reverse water-gas shift reaction taking place.

Total CO_2 flux from the seeded molecular beams is determined by first calibrating the pressure rise in the sample chamber with a nude Bayard-Alpert ion gauge while open to neat CO_2 beams.[28] With knowledge of the chamber pumping speed, the relative sensitivity of the gauge to CO_2,[44,45] and the beam's spot size on the Au(111) crystal, the molecular flux of the neat beam is determinable. For neat beams at different stagnation pressures, the calculated fluxes were each correlated with an observed rise in signal at $m/z = 44$ when open to the chamber as measured by a residual gas analyzer (RGA) located outside of the beam's line of sight. Linear regression yields direct conversion between RGA signal rise and total CO_2 flux, and in this way, CO_2 flux in seeded beams could be determined purely from the RGA readings for all experiments.

5.3 Results and Discussion

A. Embedding: Ice Structure and Composition

Upon exposure of ASW to high-translational-energy CO_2, a rich profile of local environments are observed between 2320 and 2380 cm^{-1}. Figure 5.1 depicts example chronological spectra obtained by continuously exposing an ASW film to CO_2 with average translational energy of 4.1 eV. While our analysis focuses primarily on monitoring the intensity of the most prominent mode at 2341 cm^{-1} as a function of exposure and CO_2 translational kinetic energy, the overall IR response of the film encompasses detailed information about the structure of the ice film after embedding and is worth highlighting. The sharp (FWHM < 5 cm^{-1}) signal at 2341 cm^{-1} exhibits a 4 cm^{-1} redshift compared to signals observed in pure CO_2 ices, both thick and thin.[33,46,47] This observation aligns with those made in several studies; CO_2

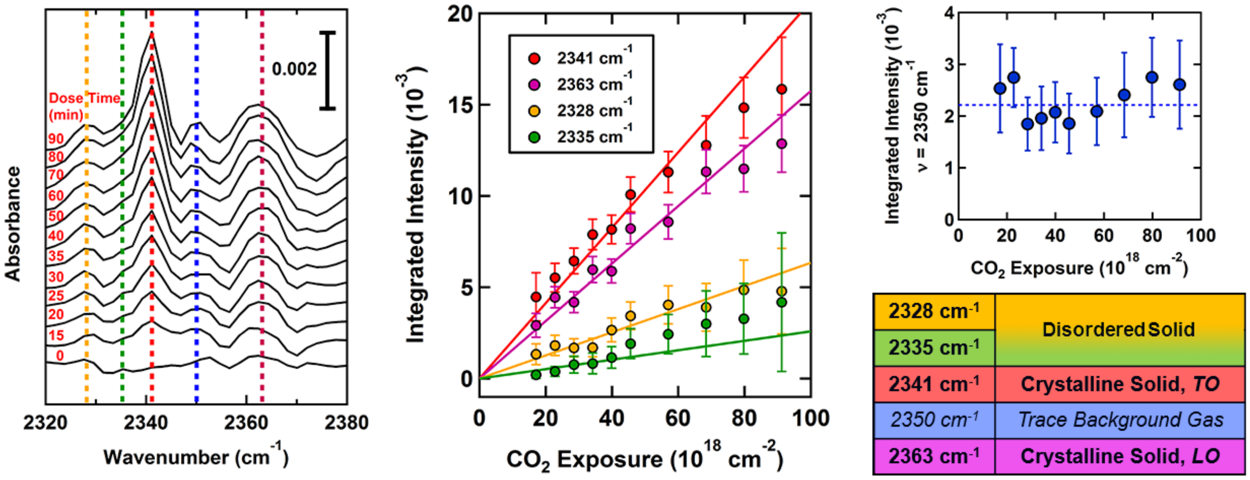

2328 cm^{-1}	**Disordered Solid**
2335 cm^{-1}	
2341 cm^{-1}	**Crystalline Solid, *TO***
2350 cm^{-1}	*Trace Background Gas*
2363 cm^{-1}	**Crystalline Solid, *LO***

Figure 5.1. Representative RAIR spectra obtained during exposure of 4.1 eV CO_2 to sixty-layer-thick amorphous H_2O ice film. Boldface signals in table (2328, 2335, 2341, 2363 cm^{-1}) are associated with solid CO_2 uptake, whose integrated peaks grow linearly as a function of total exposed CO_2. The signal at 2350 cm^{-1} is associated with trace background CO_2 in the IR beam path within the sample chamber and remains essentially constant throughout the experiment as shown in the top-right plot.

weakly interacting with surrounding water decreases the ν_3 mode's effective force constant, making distinction between *surface adsorbed* and *bulk absorbed* CO_2 trivial.[47,48] Given that stable CO_2 deposition occurs below 90 K[32]—much lower than our experimental conditions—and that another signal does not appear near 2345 cm^{-1}, we infer that all CO_2 accumulated on the surface must be buried beneath the vacuum-solid interface, despite the fact that the ASW film is nonporous as prepared.[49] It is also important to note that we do not observe uptake when the ice film is crystalline. This observation is consistent with our prior reports of embedding and persistance occurring more readily within amorphous films, compared to crystalline films; molecular dynamics simulations of hyperthermal Xe collisions with crystalline ice produce trajectories whereby a Xe atom is ejected from within the selvedge on the order of picoseconds.[25-28]

Concurrent with growth of the 2341 cm^{-1} peak is growth of a peak at 2363 cm^{-1}, suggesting that accumulated CO_2 molecules are not homogeneously, "infinitely" diluted within the ice but concentrated into small aggregates. This is in agreement with one study concluding that CO_2 is mobile within ice above 60 K and exhibits a high degree of segregation when deposited above this temperature; CO_2 exists within ices of this nature mostly as pure crystallites.[50] This peak assignment further aligns with numerous studies of CO_2 clusters in both pure gaseous and solid phases.[51-55] The two aforementioned peaks correspond, respectively, to the transverse optical (TO) and longitudinal optical (LO) modes of the crystallites, and the peak position of the LO mode in particular (2363 cm^{-1}) suggests that CO_2 aggregates within the ice resemble rods, as opposed to large slabs (2381 cm^{-1}) or spheres (2356 cm^{-1}).[56-58] Offering insightful contrast, CF_4 showed no signs of clustering after embedding into ASW grown under identical conditions in our prior work.[28] Aggregation dynamics within the ice film are expected to depend on both the mobility of the absorbed species and the relative energetic interactions between guest and host molecules. CF_4

molecules are quite similar to noble gases in terms of their intermolecular interactions; high symmetry and small size leads to CF_4's weak electrostatic interactions with itself and other molecules.[59] Interaction energies of CF_4 with itself and water are each on the order of only a few kJ/mol,[60-62] while CO_2 dimer interaction energy is roughly equal to, if not greater than, that of CO_2-H_2O, and closer in magnitude (~20-25 kJ/mol) to the H_2O dimer interaction energy (~40 kJ/mol).[32,63]

Aside from an unchanging weak absorption at 2050 cm^{-1} from trace gaseous CO_2 in the IR beam path, Figure 5.1 also tracks two weak features at 2328 cm^{-1} and 2335 cm^{-1}. The former has previously been identified in literature as belonging to amorphous or disordered CO_2,[64] although our surface is well above the temperature at which amorphous CO_2 is stable. Indeed, extremely red-shifted spectral features have been reported in CO_2/H_2O mixtures,[65] but again, studies such as these were conducted at temperatures well below 125 K, complicating direct comparison. Literature studies suggest that, for instance, the surface and subsurface layers of water ice nanocrystals can have differing degrees of disorder compared to their cores,[66,67] and absent any confirmation by high-level theoretical simulations of this system, it remains plausible that CO_2 aggregates formed after embedding exhibit analogous behavior.

B. Kinetics and Dynamics of CO2 Embedding in Ice

As noted in the experimental section, H_2O can also be generated in the seeded supersonic molecular beam at the nozzle temperatures required to obtain CO_2 with the highest translational energies studied. Consequentially, H_2O is also deposited onto the ice film throughout CO_2 exposure, typically at or below a rate of ~10^{-2} layers per second. To deconvolute our observations from this co-deposition, and to confirm no modification of our embedding results due to the presence of low water flux, a series of control experiments were executed, with results detailed in

Figure 5.2. Ice films were exposed to either CO_2/H_2O mixtures—produced by bubbling CO_2 through an H_2O filled reservoir—or exposed to a lower energy (~1 eV) CO_2 beam during simultaneous backfilling of the sample chamber with pure water vapor. Figure 5.2*a* compares RAIR spectra from both high- and low-energy trials with equal total CO_2 exposures. In all cases, only trace gaseous background CO_2 (2050 cm^{-1}) was observed when low-energy CO_2 was used, irrespective of the total H_2O co-deposition rate and the manner in which H_2O was deposited. Figure 5.2*b* shows an embedding experiment where, beginning at the 120-minute mark, the total deposition rate of H_2O was deliberately increased by one order of magnitude *via* simultaneous backfilling of the chamber with H_2O. As evidenced by the plot, the CO_2 uptake rate remains consistent despite the large differences in H_2O deposition rate. Thus, these results confirm the embedding rate's independence from the low water flux; burying does not occur. These findings are, again, further backed by temperature-programmed desorption (TPD) experiments in the literature performed on both Au(111) and H_2O ice that place stable deposition of CO_2 at surface temperatures well below 125 K.[32]

The initial CO_2 uptake rate is observed to be linear in all measurements made with exposure to CO_2 with translational energy 3.0 eV or greater. Figure 5.3 shows uptake rates of CO_2 by amorphous ice at three different average translational energies with the abscissae of each data set normalized to each other by their respective CO_2 fluxes. In order to approximate the total amount of CO_2 molecules embedded at any given time, the integrated intensity of the 2341 cm^{-1} peak is divided by the absorptivity of this mode for CO_2 diluted in ice (1:10), as measured *via* transmission IR by Sandford and Allamandola at 10 K.[63] The absorptivity is linearly corrected to one at 125 K, as discussed in their paper. Given this transformation, the slopes of the linear uptake curves

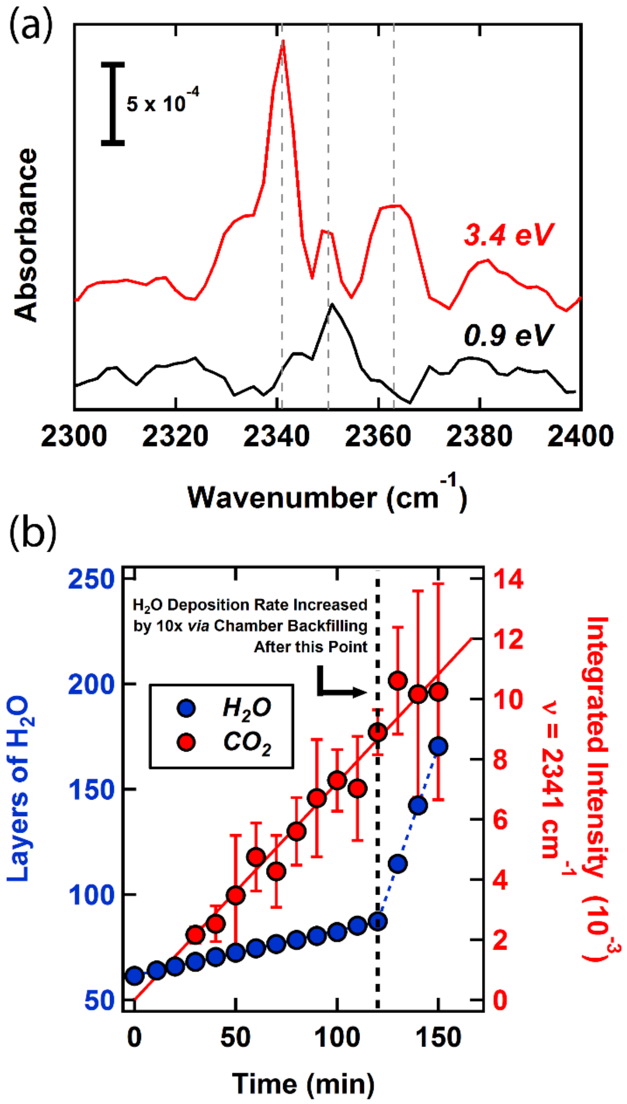

Figure 5.2. (*a*) CO_2 RAIRS signals obtained during exposure to a high-translational-energy seeded CO_2 beam (red) and during low-translational-energy beam co-deposition of CO_2/H_2O (black). High CO_2 translational energies are required for resolution of solid CO_2 spectroscopic signals. (*b*) Embedding experiment with two different total H_2O deposition rates over the course of exposure, showing no change in the rate of CO_2 uptake as measured by RAIRS and demonstrating the observed accumulation's independence from background water deposition.

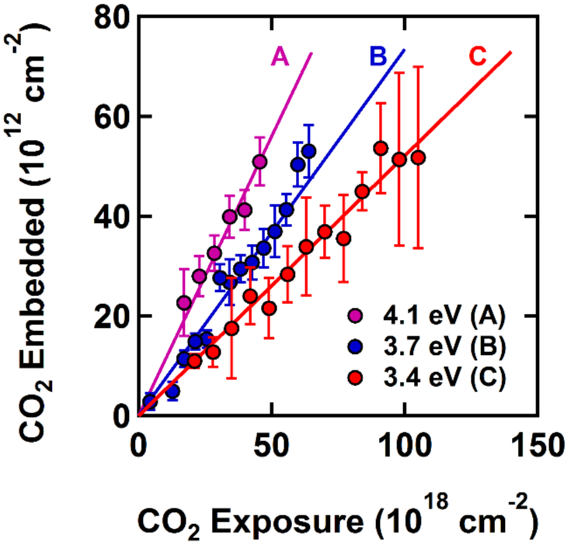

Figure 5.3. Initial embedding probabilities on ASW for three different average CO_2 energies. See text for details regarding conversion of ordinate axes from integrated peak intensity to number embedded. Over the energy range studied, as the average kinetic energy of the incident CO_2 increases, the initial embedding probability also increases.

represent initial embedding probabilities for CO_2 at the respective energetic conditions. As seen in Figure 5.3, the initial uptake rate is clearly highest for the most energetic CO_2 molecules.

The CO_2 molecules in the molecular beam populate a translational energy distribution with a finite width, and therefore each embedding probability measured represents a convolution of the energy distribution with a small range of probabilities. To deconvolute the data and extract the true energy dependence outlining the dynamics of the embedding process, a polynomial nonlinear least-squares fit to the data, $f(E)$, was employed as an ansatz for the actual rate dependence and deconvoluted from the incident energy distribution, $P(E)$, to give the measured dependence, $F(E)$, as plotted in Figure 5.4*a*:

$$F(E) = \int f(E)P(E)dE \qquad (5\text{-}1)$$

The results are consistent with conclusions made previously, namely that: (a) there is a rapid increase in embedding probability above some energetic threshold, and (b) given that the projectile is below a critical size, the mass of the projectile is important in predicting embedding efficacy.[28] Figure 5.4*b* clarifies this point, revealing the embedding probability of ~4 eV CO_2 to be roughly one and three orders of magnitude lower than that of homoenergetic CF_4 and Xe, respectively, despite similar size (radii as estimated from gas-phase van der Waals *b* parameters:[68] CO_2, 2.1 Å; CF_4, 2.9 Å; Xe, 2.7 Å).

C. Embedding as an Activated Process

In order for a projectile to embed, it clearly must first overcome an energetic barrier associated with travelling beyond the immediate vacuum-solid interface in order to become buried within or underneath the selvedge, and therefore embedding can be considered an activated process. As originally established by Lennard-Jones, the paradigmatic notion of a barrier formed from the crossing of repulsive and attractive states between a gaseous projectile and a metal surface sought

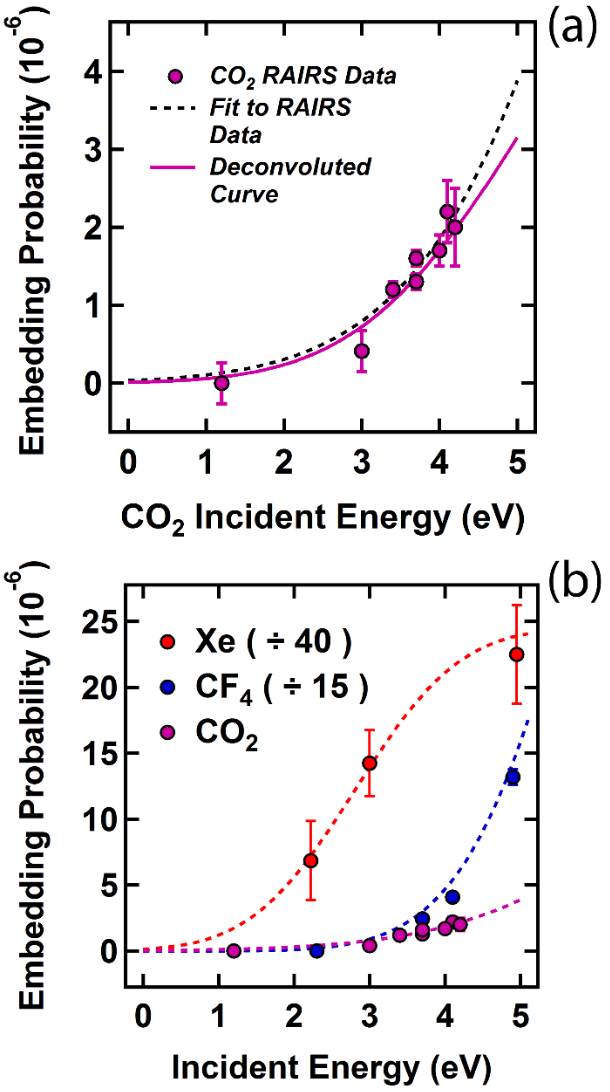

Figure 5.4. (*a*) Initial CO_2 embedding probability increases as a function of incident kinetic energy. Measured data are deconvoluted from the CO_2 energy distributions using a polynomial ansatz, yielding the solid purple curve (see text for details). (*b*) Application of constrained, parameterized *S*-curves to the data allow for comparison of CO_2 embedding probabilities to those previously measured for CF_4 and Xe. Over a similar energy range, the embedding probability for CO_2 is measured to be smaller by roughly one and three orders of magnitude as compared to CF_4 and Xe, respectively.

to describe the dynamics of dissociative adsorption.[69] The underlying dynamics behind projectiles embedding into ASW draw close comparison with these processes upon inspection (e.g. rapid increase above a threshold, saturation at high energy), and application of an empirical classical barrier to this entrance channel offers an opportunity to draw useful conclusions by comparing the dynamics of all projectiles we have studied, including CO_2. To this end, we adopt an S-shaped, parameterized form for the embedding probability used to evaluate the dissociative adsorption dynamics of molecular hydrogen on single-crystal copper surfaces[70] and described by Harris:[71]

$$\sigma(E) = \frac{A}{2}\left(1 + \tanh\frac{E - E_0}{W}\right) \tag{5-2}$$

In the above equation, E_0 represents the energetic barrier, W represents the range of energies over which the curve rises—related to a distribution of barrier heights dependent upon position of impact, and A represents the saturation value for the probability.

The application of this empirical model to our data is presented in Figure 5.4*b*. We expect that ice morphology critically influences the embedding process—projectiles are more deeply embedded in amorphous ice[25-28]—and while ASW morphology heavily depends upon both surface temperature and deposition angle, ASW films grown at 125 K are expected to be insensitive to deposition method,[49] and thus all ice films studied here are consistent. Consequently, A and W are held constant in these fits to compare the projectiles within this framework, given their size does not prevent their embedding; they are all smaller than SF_6, the largest projectile we have investigated which did not embed at any energy examined.[28] The fits were performed with A held constant at 0.001 and W constrained between 1 and 2 eV for the case of CO_2 due to our data sampling only the low-energy region of the curve. The curves in Figure 5.4*b* clearly show that, over the examined energy range, the embedding probability of CO_2—the projectile with the lowest mass—is significantly lower than that of the heavy CF_4 and Xe projectiles. Importantly, under this

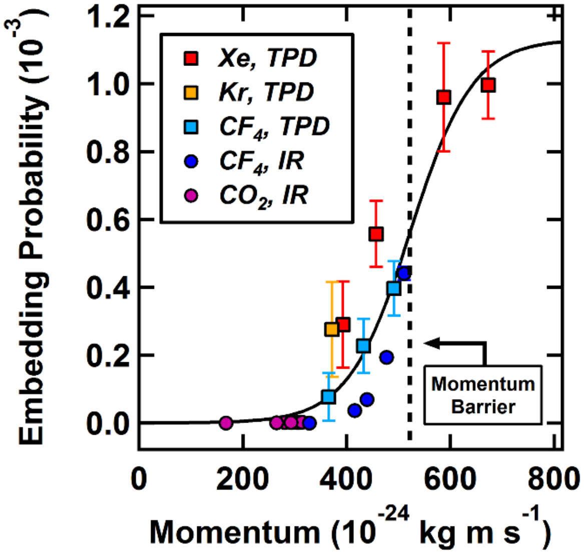

Figure 5.5. Accounting for the mass of each projectile yields a singular value for the barrier in terms of momentum; a plot of all amassed embedding data traces a unified barrier model across the sampled momentum space.

treatment, the *energetic* barrier values (E_0) for the Xe, CF_4, and CO_2 projectiles all yield nearly identical values for the barrier in terms of the *momentum*. Illustrated in Figure 5.5, the embedding probability is plotted against the incident translational momentum for all data amassed by our group, and the complete momentum space sampled appears to trace a single curve. This is the first compelling empirical evidence in support of our prior conclusion that embedding efficacy is shaped by the incident translational momentum of a projectile upon collision with ice.[28]

Open questions remain regarding the inherent differences in embedding efficacy involving ASW versus CI films. Ice films possess remarkable resilience to bombardment by high-energy projectiles *via* rapid energy dissipation,[41] and facile momentum transfer between projectiles and the recoiling ice matrix clearly leads to observable trapping at elevated temperatures relative to the desorption temperature of the projectiles, but perhaps *only* if the projectile drives deep enough into the ice film upon impact. Although possible that the initial entrance of a projectile is different between the two structures, factors affecting a projectile's persistence (*i.e.* extent of momentum transfer, mobility within the ice, cohesion of the surrounding ice lattice) once embedded are likely important—perhaps the most important—considerations, with higher embedding probability in ASW possibly linked to its hybrid liquid/solid characteristics.[72-74] While future theoretical work on this system is planned, support for this hypothesis comes in the form of prior molecular dynamics simulations of hyperthermal Xe collisions with hexagonal ice, where Xe atoms with high incident translational energy and trajectories primarily closer to normal incidence relative to the surface penetrated the vacuum-solid interface to greater depths, residing within the first one to four layers at the vacuum-solid interface and exhibiting low desorption probability at long ice residence time.[25,27]

5.4 Conclusions

Utilizing time-resolved *in situ* RAIRS we have conducted the first study of hyperthermal CO_2 capture by ASW under UHV conditions. These measurements were done at a temperature below but approaching its crystallization point. CO_2 is observed to directly embed underneath the vacuum-film interface and become trapped in the ice matrix at a much higher temperature than that allowed by thermal accretion, rapidly diffusing to form aggregates with primarily rod-like geometries, as suggested by the distinct spectroscopic signature observed. Application of a classical model treating the entrance of CO_2 and other gaseous projectiles into the ice as an activated process provides empirical evidence that projectile momentum is a general defining factor for embedding probability, provided that the projectile is not too large. Molecular dynamics simulations of the CO_2/H_2O interaction presented here would be a fruitful future endeavor and could provide further insight into the embedding of gaseous molecules with strong electrostatic interactions. Additionally, examination of embedding efficacies over a wider range of surface temperatures may better define the relationship between embedding probability and an embedded projectile's persistence in terms of its mobility within an amorphous ice film; we plan to pursue this route with the future construction of instrumentation capable of achieving significantly lower ice temperatures.

The results produced herein host significance in applications pertaining to the measurement and accurate modelling of gaseous accretion by ices, both terrestrial and extraterrestrial; relevant areas of interest include comet and planetesimal formation in the interstellar medium, gas capture related to global energy and climate issues, and the icing of aircraft in high velocity gas flows. A complete account of ice modification by gases is bolstered by recognition of embedding as a pathway for the uptake of gases by water ice at temperatures which would otherwise thermodynamically prohibit surface adsorption.

References

1. Sill, G.T.; Wilkening, L. *Icarus* **1978,** *33,* 13.
2. Owen, T.; Bar-Nun, A. *Icarus* **1995,** *116,* 215.
3. Dauphas, N. *Icarus* **2003,** *165,* 326.
4. Owen, T. *Space Sci. Rev.* **2008,** *138,* 301.
5. Notesco, G.; Bar-Nun, A.; Owen, T. *Icarus* **2003,** *162,* 183.
6. Yokoichi, R.; Marboeuf, U.; Quirico, E.; Schmitt, B. *Icarus* **2012,** *218,* 760.
7. Burke, D.J.; Brown, W.A. *Phys. Chem. Chem. Phys.* **2010,** *12,* 5947.
8. Ehrefreund, P.; Charnley, S.B. *Annu. Rev. Astron. Astrophys.* **2000,** *38,* 427.
9. Gudipati, M.S.; Allamandola, L.J. *Astrophys. J.* **2003,** *596,* L195.
10. Nuevo, M.; Bredehöft, J.H.; Meierhenrich, U.J.; d'Hendecourt, L.; Thiemann, W.H.-P. *Astrobiology* **2010,** *10,* 245.
11. Barks, H.L.; Buckley, R.; Grieves, G.A.; Mauro, E.D.; Hud, N.V.; Orlando, T.M. *ChemBioChem* **2010,** *11,* 1240.
12. Congiu, E.; Chaabouni, H.; Laffon, C.; Parent, P.; Baouche, S.; Dulieu, F. *J. Chem. Phys.* **2012,** *137,* 054713/1.
13. Kaiser, R.I.; Maity, S.; Jones, B.M. *Angew. Chem., Int. Ed.* **2014,** *54,* 195.
14. de Marcellus, P.; Meinert, C.; Myrgorodska, I.; Nahon, L.; Buhse, T.; d'Hendecourt, L.L.S.; Meierhenrich, U.J. *Proc. Natl. Acad. Sci.* **2015,** *112,* 965.
15. MacDonald, G.J. *Clim. Change* **1990,** *16,* 247.
16. Makogon, Y.F.; Holditch, S.F.; Makogon, T.Y. *J. Pet. Sci. Eng.* **2007,** *56,* 14.
17. Schüth, F. *Nature* **2005,** *434,* 712.
18. Veluswarmy, H.P.; Kumar, R.; Linga, P. *Appl. Energy* **2014,** *122,* 112.
19. Aaron, D.; Touris, C. *Sep. Sci. Technol.* **2005,** *40,* 321.

20. Linga, P.; Kumar, R.; Lee, J.D.; Ripmeester, J.; Englezos, P. *Int. J. Greenhouse Gas Control* **2010,** *4*, 630.
21. d’Hendecourt, L.B.; de Muizon, M.J. *Astron. Astrophys.* **1989,** *223,* L3.
22. Gibb, E.L.; Whittet, D.C.B.; Schutte, W.A.; Boogert, A.C.A.; Chiar, J.E.; Ehrenfreund, P.; Gerakines, P.A.; Keane, J.V.; Tielens, A.G.G.M.; van Dishoeck, E.F.; Kerkhof, O. *Astrophys. J.* **2000,** *536,* 347.
23. Martínez-Botí, M.A.; Foster, G.L.; Chalk, T.B.; Rohling, E.J.; Sexton, P.F.; Lunt, D.J.; Pancost, R.D.; Badger, M.P.S.; Schmidt, D.N. *Nature* **2015,** *518,* 49.
24. Martínez-Botí, M.A.; Marino, G.; Foster, G.L.; Ziveri, P.; Henehan, M.J.; Rae, J.W.B.; Mortyn, P.G.; Vance, D. *Nature* **2015,** *518,* 219.
25. Gibson, K.D.; Killelea, D.R.; Yuan, H.; Becker, J.S.; Pratihar, S.; Manikandan, P.; Kohale, S.C.; Hase, W.L.; Sibener, S.J. *J. Phys. Chem. C* **2012,** *116,* 14264.
26. Gibson, K.D.; Killelea, D.R.; Becker, J.S.; Yuan, H.; Sibener, S.J.. *Chem. Phys. Lett.* **2012,** *531,* 18.
27. Pratihar, S.; Kohale, S.C.; Yang, L.; Manikandan, P.; Gibson, K.D.; Killelea, D.R.; Yuan, H.; Sibener, S.J.; Hase, W.L. *J. Phys. Chem. C* **2013,** *117,* 2183.
28. Gibson, K.D.; Langlois, G.G.; Li, W.; Killelea, D.R.; Sibener, S.J. *J. Chem. Phys.* **2014,** *141,* 18C514/1.
29. Ocampo, J.; Klinger, J. *J. Colloid Interface Sci.* **1982,** *86,* 377.
30. Bar-Nun, A.; Dror, J.; Kochavi, E.; Laufer, D. *Phys. Rev. B* **1987,** *35,* 2427.
31. Notesco, G.; Bar-Nun, A. *Icarus* **1997,** *126,* 336.
32. Collings, M.P.; Anderson, M.A.; Chen, R.; Dever, J.W.; Viti, S.; Williams, D.A.; McCoustra, M.R.S. *Mon. Not. R. Astron. Soc.* **2004,** *354,* 1133.

33. Kumi, G.; Malyk, S.; Hawkins, S.; Reisler, H.; Wittig, C. *J. Phys. Chem. A* **2006,** *110,* 2097.

34. Hood, L.L. *Meteorit. Planet. Sci.* **1998,** *33,* 97.

35. Joslin, R.D. *Annu. Rev. Fluid Mech.* **1998,** *30,* 1.

36. Cebeci, T.; Kafyeke, F. *Annu. Rev. Fluid Mech.* **2003,** *35,* 11.

37. Gibson, K.D.; Killelea, D.R.; Yuan, H.; Becker, J.S.; Sibener, S.J. *J. Chem. Phys.* **2011,** *134,* 034703/1.

38. Pirug, G.; Bonzel, H.P. *Surf. Sci.* **1998,** *405,* 87.

39. Henderson, M.A. *Surf. Sci. Rep.* **2002,** *46,* 1.

40. Hodgson, A.; Haq, S. *Surf. Sci. Rep.* **2009,** *64,* 381.

41. Killelea, D.R.; Gibson, K.D.; Yuan, H.; Becker, J.S.; Sibener, S.J. *J. Chem. Phys.* **2012,** *136,* 144705/1.

42. Tingey, G.L. *J. Phys. Chem.* **1966,** *70,* 1406.

43. Shebaro, L.; Bhalotra, S.R.; Herschbach, D. *J. Phys. Chem. A* **1997,** *101,* 6775.

44. Itikawa, Y. *J. Phys. Chem. Ref. Data* **2002,** *31,* 749.

45. Itikawa, Y. *J. Phys. Chem. Ref. Data* **2006,** *35,* 31.

46. Falk, M. *J. Chem. Phys.* **1987,** *86,* 560.

47. Gálvez, O.; Ortega, I.K.; Maté, B.; Moreno, M.A.; Martín-Llorente, B.; Herrero, V.J.; Escribano, R.; Gutiérrez, P.J. *Astron. Astrophys.* **2007,** *472,* 691.

48. Bernstein, M.P.; Cruikshank, D.P.; Sanford, S.A. *Icarus* **2005,** *179,* 527.

49. Kimmel, G.A.; Stevenson, K.P.; Dohnálek, Z.; Smith, R.S.; Kay, B.D. *J. Chem. Phys.* **2001,** *114,* 5284.

50. Hodyss, R.; Johnson, P.V.; Orzechowska, G.E.; Goguen, J.D.; Kanik, I. *Icarus* **2008,** *194,* 836.

51. Barnes, J.A.; Gough, T.E. *J. Chem. Phys.* **1987,** *86,* 6012.

52. Ewing, G.E.; Sheng, D.T. *J. Phys. Chem.* **1988,** *92,* 4063.

53. Fleyfel, F.; Devlin, J.P. *J. Phys. Chem.* **1989,** *93,* 7292.

54. Signorell, R.; Kunzmann, M.K. *Chem. Phys. Lett.* **2003,** *371,* 260.

55. Bonnamy, A.; Georges, R.; Hugo, E.; Signorell, R. *Phys. Chem. Chem. Phys.* **2005,** *7,* 963.

56. Jones, L.H.; Swanson, B.I. *J. Phys. Chem.* **1991,** *95,* 2701.

57. Ovchinnikov, M.A.; Wight, C.A. *J. Chem. Phys.* **1993,** *99,* 3374.

58. Taraschewski, M.; Cammenga, H.K.; Tuckermann, R.; Bauerecker, S. *J. Phys. Chem. A* **2005,** *109,* 3337.

59. Winkler, M.; Harnes, J.; Børve, K.J. *J. Phys. Chem. A* **2011,** *115,* 13259.

60. Tsuzuki, S.; Uchimaru, T.; Mikami, M.; Urata, S. *J. Chem. Phys.* **2002,** *116,* 3309.

61. Mahlanen, R.; Jalkanen, J.-P.; Pakkanen, T.A. *Chem. Phys.* **2005,** *313,* 271.

62. Caminati, W.; Maris, A.; Dell'Erba, A.; Favero, P.G. *Angew. Chem. Int. Ed.* **2006,** *45,* 6711.

63. Sandford, S.A.; Allamandola, L.J. *Astrophys. J.* **1990,** *355,* 357.

64. Escribano, R.M.; Muñoz Caro, G.M.; Cruz-Diaz, G.A.; Rodríguez-Lazcano, Y.; Maté, B. *Proc. Nat. Acad. Sci.* **2013,** *110,* 12899.

65. Ehrenfreund, P.; Boogert, A.C.A.; Gerakines, P.A.; Tielens, A.G.G.M., van Dishoeck, E.F. *Astron. Astrophys.* **1997,** *328,* 649.

66. Buch, V.; Delzeit, L.; Blackledge, C.; Devlin, J.P. *J. Phys. Chem.* **1996,** *100,* 3732.

67. Devlin, J.P.; Buch, V. *J. Phys. Chem. B* **1997,** *101,* 6095.

68. *CRC Handbook of Chemistry and Physics.* 89th ed. CRC Press: Boca Raton, FL, 2008-2009; 6.

69. Lennard-Jones, J.E. *Trans. Faraday Soc.* **1932,** *28,* 333.

70. Balooch, M.; Cardillo, M.J.; Miller, D.R.; Stickney, R.D. *Surf. Sci.* **1974,** *46,* 358.

71. Harris, J. *Surf. Sci.* **1989,** *221,* 335.

72. Smith, R.S.; Dohnálek, Z.; Kimmel, G.A.; Stevenson, K.P.; Kay, B.D. *Chem. Phys.* **2000,** *258,* 291.

73. Angell, C.A. *Annu. Rev. Phys. Chem.* **2004,** *55,* 559.

74. Shalit, A.; Perakis, F.; Hamm, P. *J. Phys. Chem. B* **2013,** *117,* 15512.

CHAPTER 6

REVERSE WATER-GAS SHIFT REACTION IN SUPERSONIC NOZZLE WITH CATALYTIC METAL SURFACE

Resistive heating of the metal surface of a supersonic molecular beam's nozzle is shown to be very effective in converting CO_2 diluted (1% and 10%) in H_2 to CO and H_2O via the reverse water-gas shift (RWGS) reaction at temperatures that preclude simple pyrolysis. The reaction yield is observed to reach values as high as 90% at 750 ℃, with no other hydrocarbons detected. The stainless steel surface of the nozzle appears to facilitate the reaction as a heterogeneous catalyst. Reaction yield is observed to increase with higher nozzle temperature, P_{CO_2}/P_{H_2}ratio, or lower stagnation pressure. The dependence of the reaction upon stagnation pressure highlights an interplay between the escape of reactants from the nozzle and associated RWGS reaction kinetics.

6.1 Introduction

The thermodynamic equilibrium that exists between a system containing carbon dioxide, hydrogen, water vapor and carbon monoxide has served as a foundation for the mass production of important, high-demand chemicals, especially ammonia and methanol. The direct reaction of carbon dioxide with hydrogen is an endothermic reaction known as the reverse of the well-known water-gas shift reaction (RWGS). The reaction is a moderately exothermic and is expressed by:

$$CO + H_2O \leftrightarrow\ CO_2 + H_2,\ \Delta H^o =\ -41.09\ kJ/mol \tag{6-1}$$

Due to extraneous formation of alcohol or hydrocarbon byproducts, and low conversions under experimentally convenient equilibrium conditions, the RWGS reaction has not attracted as much attention as its forward-direction complement. There are two major experimental methods for performing the RWGS reaction: heterogeneous catalysis and high-temperature pyrolysis;[1–6] the latter typically requires very high temperatures (>800 ℃) to overcome the energetic barrier.[1] The catalytic reaction, in contrast, is surprisingly fast when performed over several metal and metal-oxide catalysts,[4] yet the process is often accompanied by Fischer-Tropsch reactions, potentially producing various hydrocarbons including ethane.[7–9] Moreover, the overall RWGS conversion rate is typically less than 50%.[2,5,10–13]

In this paper, we report a remarkably facile route for RWGS reactions utilizing supersonic expansion of CO_2/H_2 mixtures within a heated nozzle made of stainless steel. Highly selective production of CO and H_2O is observed, with conversion yields of up to 90% at 750 ℃. Herschbach and co-workers have reported formation of higher hydrocarbons from ethane utilizing supersonic expansion from heated metal nozzles.[14] Somorjai and co-workers utilized a similar approach in elucidating the interplay between kinetic and thermodynamic control of methane pyrolysis and conversion to heavier hydrocarbons with large conversion rates.[13] The mechanism of the chemical process is discussed; formation of H radicals on the inner surface of the nozzle is followed by the reaction and desorption to the gas phase prior to supersonic expansion. The presence of the metallic wall is expected to facilitate the observed reaction.

6.2 Experimental

A. Molecular Beam Source

The experiments were conducted in an ultra-high vacuum (UHV) chamber, coupled to a triply differentially pumped molecular beam line, which has been described previously.[15,16] High translational energy supersonic molecular beams were produced by expanding 1% or 10% CO_2 diluted in H_2 through a nozzle fitted with a 15 µm Molybdenum pinhole; the nozzle gland is made of 316 stainless steel. The nozzle is wrapped along its length with wire that can be resistively heated up to 1000 ℃, and surrounded by a thin tantalum sheet to promote efficient, even heating.

Nozzle temperature was monitored with a type K thermocouple spot-welded onto the tip of the nozzle.

The molecular beam line consists of three stages of differential pumping. The gas expands into the source chamber through the nozzle described above, then enters the second differential stage, which houses a chopper wheel for time-of-flight (TOF) or square-wave (SQW) measurements. The molecules in the beam leave the beam chamber and enter into the detection chamber and traverse an electron bombardment ionizer. The ions are mass-filtered by a quadrupole and detected by electron multiplier.

In typical experiments, the reactant gas was held at stagnation pressures ranging from 200 to 700 psi. To ensure that the intensity of the beam is linearly related to the stagnation pressure, CO_2 gas intensity was monitored with different stagnation pressures at room temperature. As shown in Figure 6-1, the intensity increases linearly with increasing stagnation pressure. The thermodynamic equilibrium of the gas inside the nozzle is controlled by holding the nozzle at the temperature of interest within the range of 550 – 700 ℃ for at least two hours prior to data acquisition. Total intensity of each component of the stream was characterized using TOF measurements for the 10% mixtures andSQW measurements for the 1% mixtures. The dominant ionization signals of additional possible products such as ethane, acetone, and ethanol were also monitored.

B. RWGS Reaction Yield Calculation

CO_2 conversion was quantified by integrating the chopper-modulated signalsunder normal and catalytic beam conditions. When reaction occurs between CO_2 and H_2 (subscript *H*), the signal at m/z=28 comes from two contributions: ionization of CO and dissociative electron detachment of CO_2. At nozzle temperatures below 500 ℃ (subscript *L*), the gas mixture is not observed to react,

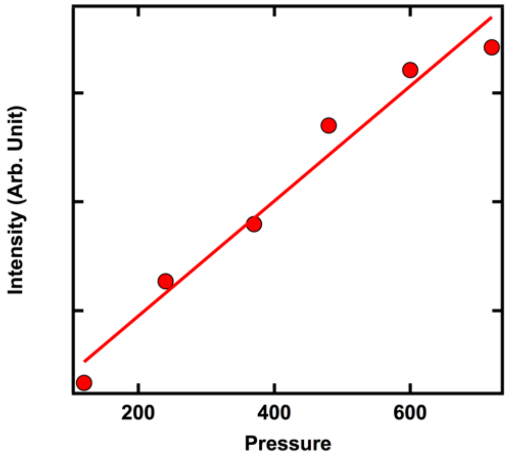

Figure 6.1. The gas intensity dependence with stagnation pressure was checked from pressure 120 psi up to 720 psi at 300K, with no RWGS reaction. The intensity was calculated by integration of TOF spectra of CO_2 at m/z=44. Within this pressure range, the intensity of the beam is linearly related with stagnation pressure.

and thus the signal at m/z=28 is from CO_2 only. Thus, the signal obtained at m/z=44 (I_{44}) and m/z=28 (I_{28}) is defined as:

$$I_{44} = CQ_{44}[N_{CO_2}\sigma_{CO_2}] \tag{6-2}$$

$$I_{28,L} = CQ_{28}\left[N_{CO_2}\sigma_D\right] \tag{6-3}$$

$$I_{28,H} = CQ_{28}\left([N_{CO}\sigma_{CO}] + \left[N_{CO_2}\sigma_D\right]\right) \tag{6-4}$$

N_{CO_2} and N_{CO} are the number densities of CO_2 and CO, Q_{44} and Q_{28} are the quadrupole transmission coefficients at m/z = 44 and 28, and *C* is an empirical constant related to our particular setup. The quoted cross sections correspond to dissociative electron detachment of CO_2 and ionization of CO_2 and CO in the ionizer, given below: [17,18]

$$CO_2 + e^- \xrightarrow{\sigma_D} CO^+ + O + 2e^-, \sigma_D = 0.389\ \text{Å}^2 \tag{6-5}$$

$$CO_2 + e^- \xrightarrow{\sigma_{CO_2}} {CO_2}^+ + 2e^-, \sigma_{CO_2} = 2.25\ \text{Å}^2 \tag{6-6}$$

$$CO + e^- \xrightarrow{\sigma_{CO}} CO^+ + 2e^-, \sigma_{CO} = 1.82\ \text{Å}^2 \tag{6-7}$$

Above 500 ℃, the ratio of CO/CO_2 intensity, η_H, is therefore:

$$\eta_H = \frac{I_{28,H}}{I_{44}} = \frac{CQ_{28}[N_{CO}\sigma_{CO}] + CQ_{28}\left[N_{CO_2}\sigma_D\right]}{CQ_{44}[N_{CO_2}\sigma_{CO_2}]} \tag{6-8}$$

Below 500 ℃, the ratio η_L is simply:

$$\eta_L = \frac{I_{28,L}}{I_{44}} = \frac{CQ_{28}\left[N_{CO_2}\sigma_D\right]}{CQ_{44}[N_{CO_2}\sigma_{CO_2}]} \tag{6-9}$$

With rearrangement of the equations above, the relative number density of CO and CO_2 in the product beam while reaction occurs is quantified by:

$$R = \frac{N_{CO}}{N_{CO_2}} = \left(\frac{\eta_H}{\eta_L} - 1\right)\left(\frac{\sigma_D}{\sigma_{CO}}\right) \tag{6-10}$$

R is readily calculable from knowledge of the cross sections from the literature, similar to previous studies,[19,20] and corrects for differential detection at m/z=28 by our detector. The yield of the

RWGS reaction, y, is therefore readily quantifiable using this measured relative number density of CO and CO_2:

$$y = \frac{N_{CO}}{N_{CO}+N_{CO_2}} = \frac{R}{R+1} \tag{6-11}$$

6.3 Results and Discussion

A. Yield of the reaction

In order to identify the products generated within the nozzle, time-of flight mass spectrometry was employed to characterize beams generated using various nozzle temperatures, pressures, and CO_2/H_2 ratios of 1% and 10%. Figure 6-2 shows example of TOF spectra of 10% CO_2 diluted in H_2, expanded at both room temperature and temperatures above 500 ℃. In Figure 6-2(a), mass spectra show only peaks corresponding to the presence of CO_2 and H_2O in the unreacted mixture as prepared, with the presence of a small peak at m/z=28 ascribed to formation of CO in the spectrometer's ionizer. Due to dissociative electron detachment of CO_2. In Figure 6-2(b-d), starting above 500 ℃, the relative signal intensities change significantly; a stark decrease in CO_2 intensity is accompanied by a clear increase in CO intensity, with detection of a new signal at m/z = 18 associated with H_2O production. Other possible products such as ethane, acetone, and ethanol, were not detected within the limits of our instrumentation. This is an implication of highly selective reactivity under our experimental conditions, namely that only the RWGS reaction occurs, possibly unaccompanied by Fischer-Tropsch reactions. These latter processes typically involves formation of surface-bound metal carbonyls that further react with hydrogen to form products other than CO and H_2O.[8,9] Under our experimental conditions, Fischer-Tropsch processes are not observed to contribute to formation of products.

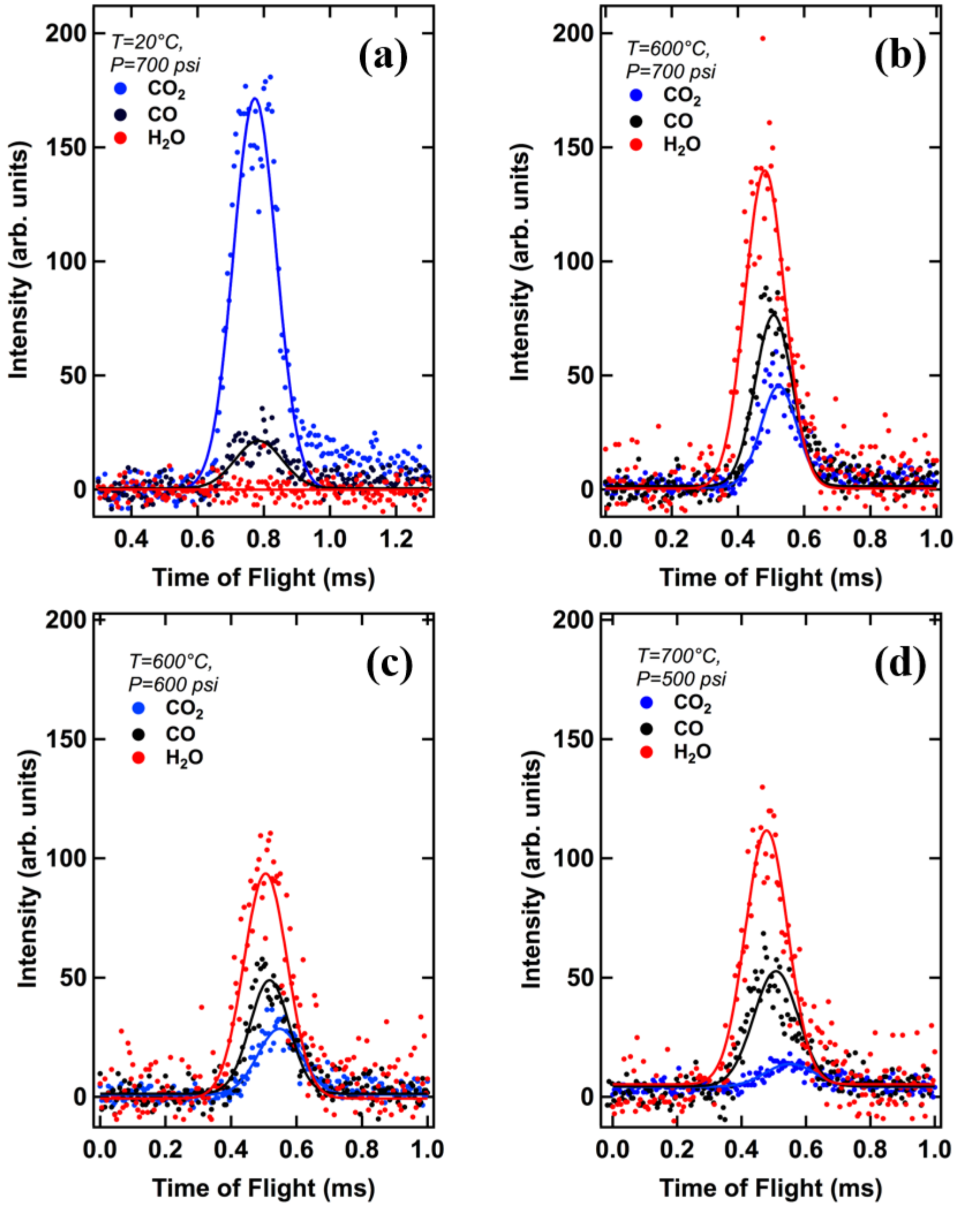

Figure 6.2. Time-of-flight beam profiles of the RWGS reaction. Panel (a) was taken at room temperature, 700 psi stagnation pressure, panel (b) was taken at 600 ℃ / 700 psi, panel (c) was taken at 600 ℃ / 600 psi, panel (d) was taken at 700 ℃ / 500 psi. The gas mixture was 10% CO_2 seeded in H_2. At temperatures higher than 500 ℃, significant amounts of CO_2 react, producing CO and water in the beam.

To track reactant depletion and product formation, TOF spectra are integrated *via* fits to guassian peaks to determine the total intensity of each species in the product beam. Observed intensity at m/z=28 is from the ionization of both CO and CO_2, and thus tracking CO production requires a subtraction of the contribution to this channel from CO_2. An example of this correction is given in Figure 6-3 using data obtained at 400 psi. Clearly, this correction becomes less important at higher nozzle temperatures due to the decreased presence of CO_2 in the product stream.

Figure 6-4 shows representative datasets tracking the change in reactants and products as a function of the nozzle temperature and pressure. Each column of five panels was measured during a single day. Of note is that the catalytic nature of the nozzle is deactivated after several runs. This deactivation is caused by coke formation behind the nozzle orifice that eventually clogs the nozzle. To regenerate the nozzle's cleanliness, the nozzle gland is removed from vacuum and sonicated in ethanol for 15 minutes. In Figure 6-4, sets 4 and 5 are observed to be deactivated; intensities of gas species are low. Except for these two sets of data, the intensity of CO_2 decreases, while intensities of H_2O and N_{CO}/N_{CO_2} increase as temperature is raised. Figure 6-5 illustrates the variation in RWGS reaction yield as a function of nozzle temperature. An average value of η_L is obtained using data collected only at 20 ℃ over the entire stagnation pressure range used. As temperature is raised, the yield increases almost linearly at all investigated stagnation pressures. This observation is consistent with the endothermic nature of the RWGS reaction.[2,11] At 750 ℃, the yield is observed to reach values as high as 90%.

Several authors have studied RWGS reactivity under similar temperature and pressure conditions with quartz reactors;[10,11,18] conversion was typically less than 0.1%.[10,18] Bustamante and co-workers investigated the effect of the metallic walls in the reaction.[11] By comparing walls made of metal and quartz, they claimed a chromium-rich surface was an active surface, resulting

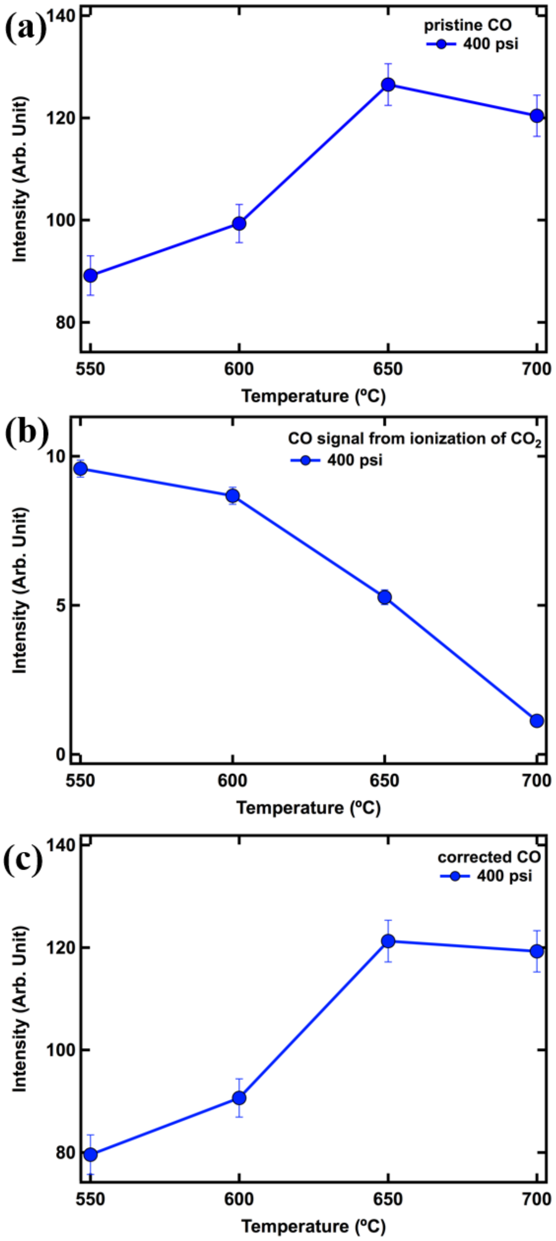

Figure 6.3. This figure is a sample correction of CO signal at stagnation pressure 400 psi. Panel (a) shows the pristine CO (m/z=28) intensity from integration of TOF measurement. It includes signal from ionization of both CO_2 and CO. Panel (b) shows the intensity of m/z=28 signal from ionization of CO_2. Panel (c) shows the corrected CO intensity, with subtraction of intensity from ionization of CO_2. Where not visible, the error bars are smaller than the data point size used.

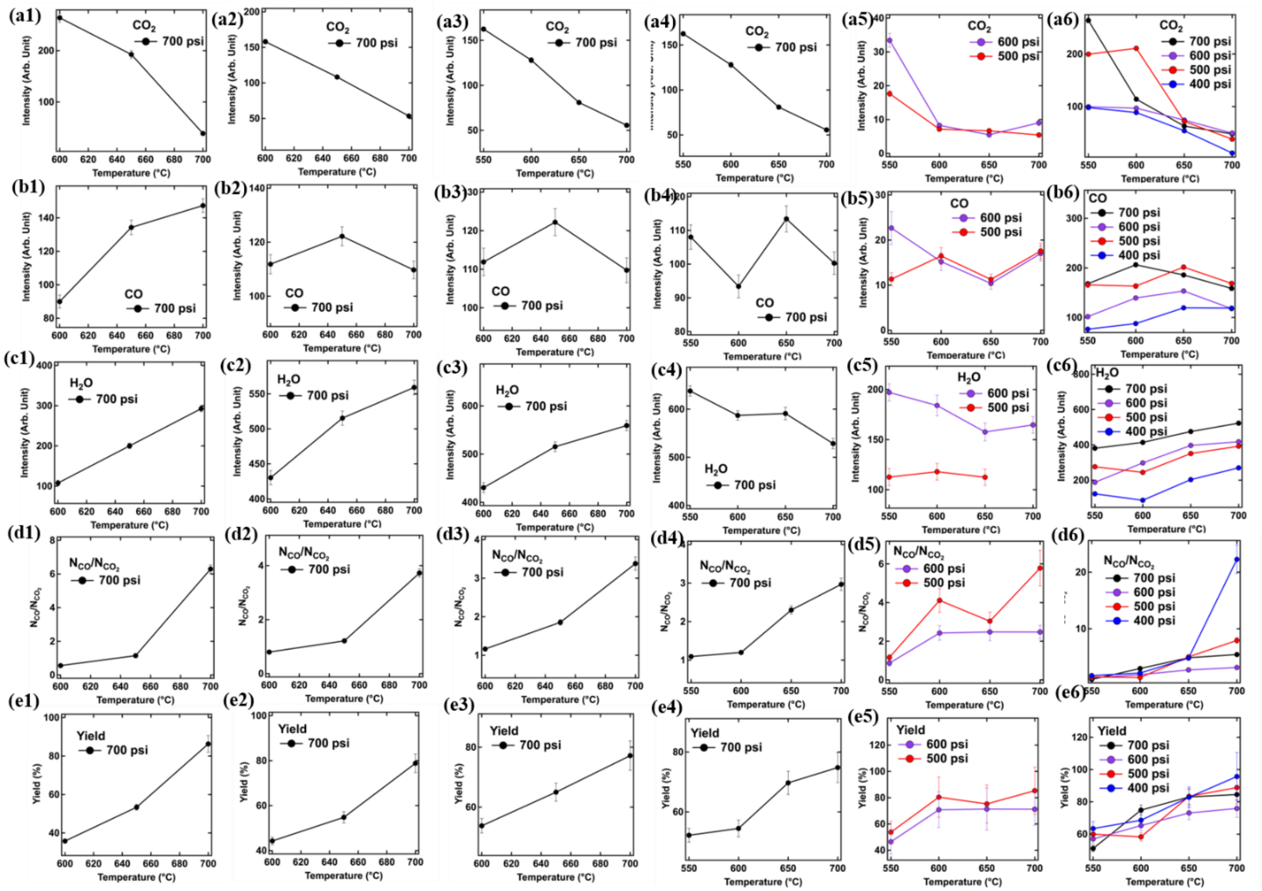

Figure 6.4. These panels show data sets of TOF data obtained at various pressures at different days. Each set of data were taken in the same day. Panel sets (a), (b) and (c) are intensity dependence of gas CO, CO_2 and H_2O at different temperatures. The intensities are obtained by integration of TOF spectra for each constituent of the gas at various temperatures and stagnation pressures. Intensity of CO is corrected by subtraction of intensity from ionization of CO_2. Panel (d) is the ratio of number density of CO and CO_2 over the examined temperature range. Where not visible, the error bars are smaller than the data point size used.

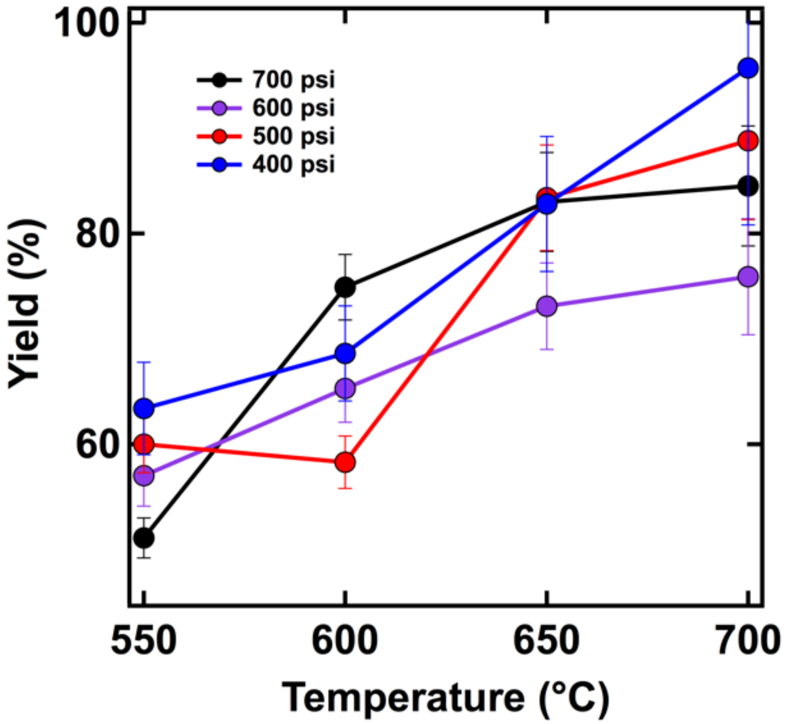

Figure 6.5. Dependence of yield with nozzle temperature at various pressures. The value of η_L is 0.13 ± 0.01, obtained at 20 ℃. The yield of the observed reaction increases with increasing nozzle temperature.

in higher conversion rates of up to 55% at 900 ℃ at ambient pressure. They assumed the metal walls of the reactor catalyzed the reaction. Such surface-facilitated reactions utilizing supersonic beams have been demonstrated in other studies.[21] Somorjai *et. al.* reported close to 100% conversion of ethane to heavier hydrocarbons in a supersonic nozzle beam.[13] They assumed the mechanism involved generation of free radicals at the nozzle surface and their subsequent gas-phase reactions before exiting the nozzle into the collision-free environment during the course of the supersonic expansion. Therefore, it is reasonable that the nozzle surface in this study was also an active surface, yielding high conversion of CO_2.

Further discussion regarding the elemental composition and structure of the nozzle wall is important here. Stainless steel is widely used in industrial applications and consumer products. The passive property of stainless steel is achieved by the formation of a chromium oxide layer on the surface. This layer of oxide prevents further oxidation of the underlying alloy. Surface analytical techniques indicate that in addition to chromium and oxygen, large amounts of iron are also present on the surface.[26] When stainless steel is vacuum annealed (> 500 ℃), surface chromium depletes and an increase in iron content is reported.[27,28] The Imoto group has shown that heating stainless steel in vacuum to temperatures above 1000 ℃ causes a dramatic increase in the surface concentration of iron.[29] Beavis found water formation when hydrogen is in contact with a stainless steel surface at temperatures greater than 100 ℃, and that the yield increased with increasing temperature. The source of oxygen was identified as possiblyoxidized carbon or water, which react with the steel surface during storage. This is consistent with what we observed under our conditions.[26]

B. Thermodynamics and Reaction Mechanism

The equilibrium constant K_p as a function of partial pressures of the gas species is:

$$K_p = \frac{P_{CO} * P_{H_2O}}{P_{CO_2} * P_{H_2}} \tag{6-12}$$

Assuming stoichiometric production of CO and H_2O, the equation can be rearranged to:

$$K_P = \left(\frac{P_{CO}}{P_{CO_2}}\right)^2 * \frac{P_{CO_2}}{P_{H_2}} = R^2 * \frac{P_{CO_2}}{P_{H_2}} = R^2 * \frac{1-R}{\alpha - R} \tag{6-13}$$

R is the relative number density of CO and CO_2, calculated from equation 6-10, and α is the initial ratio of P_{H_2}/P_{CO_2} before reaction. From the Gibbs free energy of the system:

$$\ln K_P = -\frac{\Delta H^o}{RT} + \frac{\Delta S^o}{R} \tag{6-14}$$

A plot of $\ln K_P$ as a function of 1/T yields ΔH^o, as shown in Figure 6-6. From the slope of the resulting linear plot we obtain $\Delta H^o = 96.4 \pm 8.6$ kJ mol^{-1}. This value is consistent with the expected endothermic nature of the reaction; the reaction is thermodynamically favored at higher temperatures. The value, however, differs from gas-phase studies, which is cited as 41 kJ/mol.[2,23]

The mechanisms of RWGS reactions have been studied both in the gas phase and over catalysts.[1,2,4,10,12] Several early investigations suggest surface-mediated processes, with the mechanism broadly classified as either regenerative or associative.[2,12] Reported mechanisms are dependent on catalyst composition and reaction temperature, and considerable dispute remains in mechanistic studies.[2,30] In light of our current results, the RWGS reaction mechanism taking place within our nozzle is not yet clear. High-temperature pyrolysis would require temperatures higher than those studied here, which implies that a surface-specific process is taking place.[1,10] The lack of other hydrocarbon products implies that surface-bound metal carbonyls are either not formed or do not further react with hydrogen once formed. Beavis claimed that the presence of iron on a surfacefacilitates the generation of water.[26] High temperature annealing of the stainless steel, accomplished during increases the abundance of iron from the surface and therefore could raise the probability for water generation. As shown in Figures 6-7 and 6-8, reaction yield appears to be

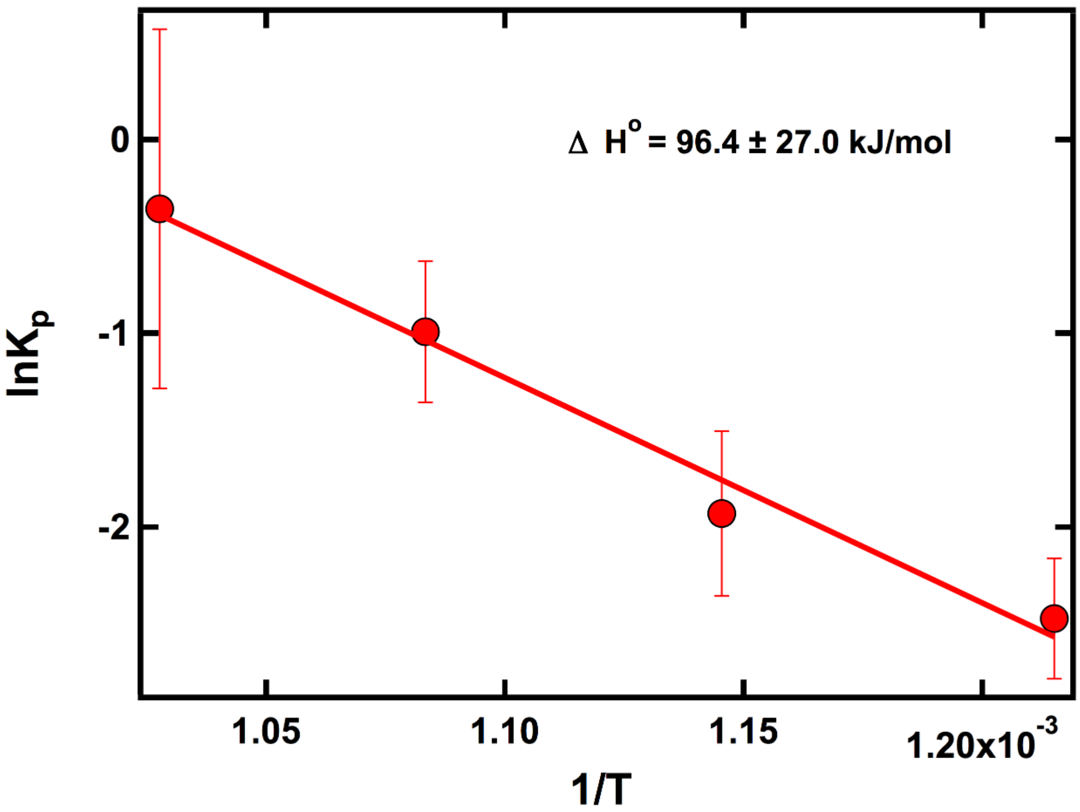

Figure 6.6. Plot of lnK_p as a function of $(^1/_T)$. Averaged values of lnK_p at different temperatures are used here. From the slope of the fitting, we obtain a value of ΔH^o of 96.4 ±8.6 kJ mol $^{-1}$.

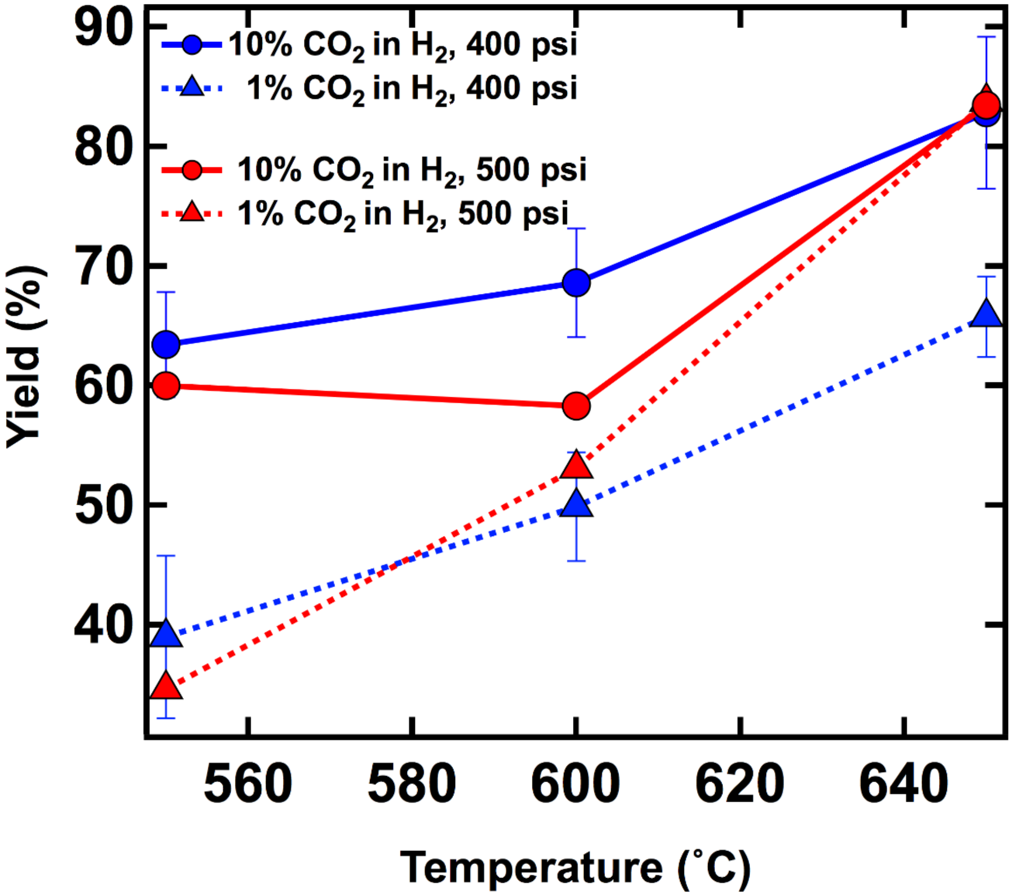

Figure 6.7. The reaction yield as a function of nozzle temperature with different P_{CO_2}/P_{H_2}ratios at 400 psi and 500 psi stagnation pressure. In general, higher ratio gives higher yield at the samenozzle temperature.

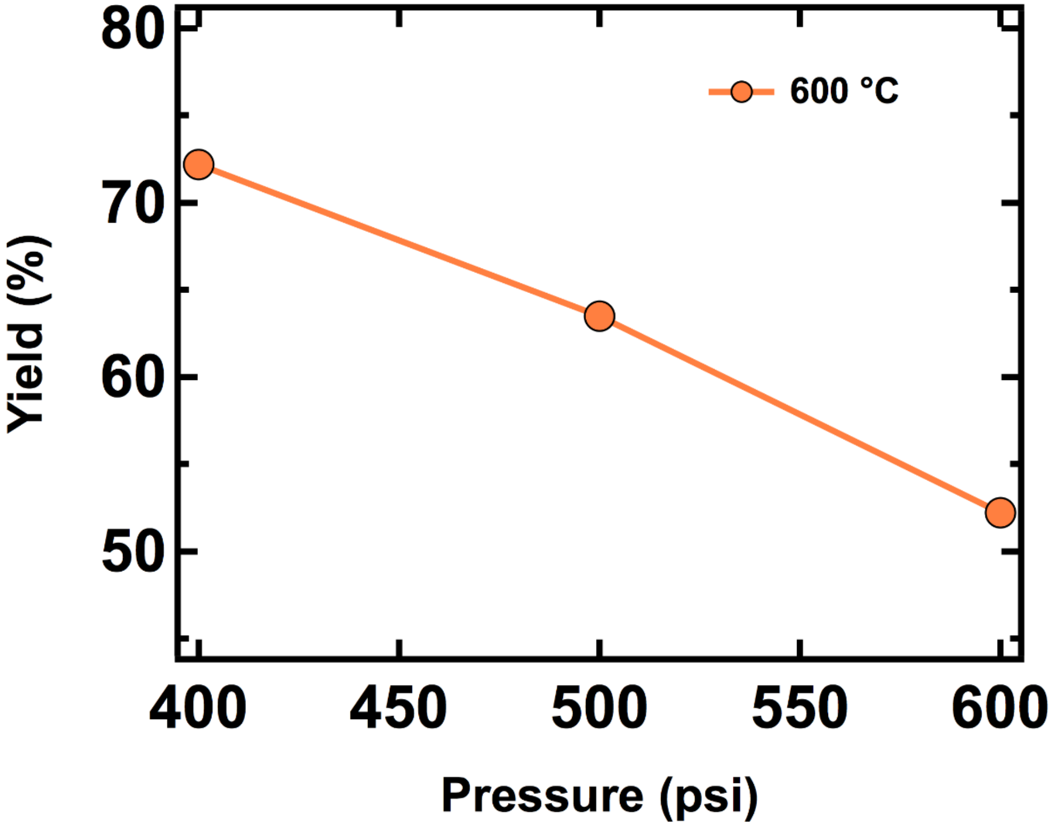

Figure 6.8. The dependence of reaction yield with stagnation pressure at nozzle temperature 600 ℃. The gas mixture was 10% CO_2 seeded in H_2. The yield is observed to be inversely proportional to pressure.

proportional to P_{CO_2}/P_{H_2} ratio, with higher yields observed in 10% CO_2/H_2 mixtures under identical nozzle conditions, but in general is observed to be inversely proportional to nozzle stagnation pressure.

Here, we postulate one possible mechanism based on the discussion above:

$$H_{2\,(g)} \rightarrow 2H_{(ads)} \tag{6-15}$$

$$CO_{2(g)} \leftrightarrow CO_{(ads)} + O_{(ads)} \tag{6-16}$$

$$O_{(ads)} + 2H_{(ads)} \leftrightarrow H_2O_{(g)} \tag{6-17}$$

$$CO_{(ads)} \rightarrow CO_{(g)} \tag{6-18}$$

$$H_2O_{(ads)} \rightarrow H_2O_{(g)} \tag{6-19}$$

In the above steps, (ads) refers to a surface-adsorbed species. It can be located on either a metal or metal oxide of Iron or Chromium. Previous studies show hemolytic dissociation of chemisorbed H_2 could result in OH^- or metal-hydrogen species on iron oxide surfaces.[31] The chemisorption and dissociation of H_2 is therefore a likely first step in our observed reactivity. Following dissociative CO_2 adsorption, several studies show formic acid species are subsequently generated on the catalyst surface after further reaction with H_2.[32] However, the lack of Fischer-Tropsch reaction products implies the formation of surface-bound formic acid is not a main channel under our conditions. Another possible elementary step is:

$$CO_{2(g)} + H_{(ads)} \leftrightarrow CO_{(g)} + OH_{(ads)} \tag{6-20}$$

The energy barrier of above step is calculated to be higher than 300 kJ mol^{-1}, which is not favored. Based on these results, we assume that reactivity is initiated by dissociation of the hydrogen on the inner surfaces of the nozzle, followed by dissociative chemisorption of carbon dioxide and subsequent water generation on the surface. Finally, water and CO desorb from the surface to the gas phase. Grenoble found that the heat of desorption of CO from a metal is high, which could indicate that the overall catalytic reactivity of the reaction is dominated by the CO desorption.[33] On Iron, CO has a heat of desorption of 136 kJ mol^{-1}.[33] This value is close to our calculated enthalpy, and suggest desorption of CO into gas is possibly the rate-limiting step, and that our beam conditions actually kinetically hinder equilibrium being reached. More evidence is needed to clarify this mechanism in terms of our experimental observations.

The yield of the reaction depends on both P_{CO_2}/P_{H_2} ratio and stagnation pressure. As H_2 uptake saturates rapidly on the surface under high pressure conditions, the reaction likely depends directly upon the probability of CO_2 finding an active site on the nozzle surface. Thus, an increase in the P_{CO_2}/P_{H_2} ratio will yield higher CO_2 partial pressure, which will naturally increase this probability. This effect is shown in Figure 6-7.[24] Another parameter to consider is the residence time of CO_2 in the nozzle gland. To estimate this, we utilize the relation for quasi one-dimensional subsonic mass flow rate from a nozzle source:.[34]

$$\frac{dm}{dt} = P_0 A \left[\frac{\gamma W}{R T_0}\left(\frac{2}{\gamma+1}\right)^{(\gamma+1)/(\gamma-1)}\right]^{1/2} \tag{6-21}$$

In the above equation, P_0 is the stagnation pressure, A is the nozzle area, γ is the heat capacity ratio of CO_2, W is the molar mass of CO_2, T_0 is the nozzle temperature, and R is the gas constant. The mass flow is easily rewritten in terms of number flow, dN/dt, and the number of CO_2 molecules inside the gland at any given time is assumed to remain constant and is calculated *via* the ideal gas law. Thus, the residence time is approximated as the ratio of the constant number of CO_2 molecules within the nozzle gland to the rate at which these molecules escape:

$$N/(dN/dt) = \frac{V}{N_A A}\left[\frac{W}{\gamma R T_0}\left(\frac{2}{\gamma+1}\right)^{-(\gamma+1)/(\gamma-1)}\right]^{1/2} \qquad (6\text{-}22)$$

Above, V is the volume within the nozzle gland, and N_A is Avogadro's number. The residence time at 500 psi and 700 °C is estimated to be on the order of ~10 ms. This lifetime is potentially short compared to the equiibrium reaction lifetimes of the elementary steps, and therefore suggests our reactivity is kinetically limited. This reasoning is in line with previous reports by Somorjai,[13] and is one possible explanation for the disparity between the reported RWGS enthalpy and our measured value. With an increase in either the stagnation pressure or the size of the nozzle (resulting in higher flow rate), the residence time will decrease.. Thus, shorter time would be available for the CO_2 molecules to find a catalytically-active site on the nozzle surface, leading to lower probability for reaction and a lower yield. This effect is confirmed in Figure 6-8, where RWGS reaction yield is observed to be inversely proportional to nozzle stagnation pressure at a nozzle temperature of 600 °C.

6.4 Conclusions

Utilizing a supersonic expansion beam technique, we demonstrate highly selective reactivity between carbon dioxide and molecular hydrogen involved in the RWGS reaction. This reaction exhibits reaction yields as high as 90% at nozzle temperatures approaching 750 °C. The yield of the reaction increases as nozzle temperature or the P_{CO_2}/P_{H_2}ratio is raised, and decreases with incremental stagnation pressure due to the increase in flow rate of the reactants out of the nozzle where the reaction takes place. The metal surface was found to serve as a heterogeneous catalyst for the reaction. This supersonic expansion technique provides opportunities to screen various catalytic reactions under high temperature and high pressure conditions. Chen and Ellison have utilized a supersonic flash pyrolysis source to produce clean, jet-cooled radical beams without recombination and/or secondary dissociation.[24–26] Thus, it is feasible for this technique to facilitate such reactions with surface-generated gas-phase radicals, followed by rapid desorption and cooling of the intermediate products.

References

1. Bradford, B. W. *J. Chem. Soc.* **1933**, 1557.
2. Newsome, D. S. *Catal. Rev.* **1980**, 21, 275.
3. Chinchen, G. C.; Spencer, M. S.; Waugh, K. C.; Whan, D. A. *J. Chem. Soc. Faraday Trans.* **1987**, 83, 2193.
4. Spencer, M. S. *Catal. Letters* **1995**, 32, 9.
5. Pettigrew, D. J.; Trimm, D. L.; Cant, N. W. *Catal. Letters* **1994**, 28, 313.
6. Koeppel, R. A; Baiker, A; Wokaun, A. *Appl. Catal. A Gen.* **1992**, 84 , 77.
7. Weatherbee, G.; Bartholomew, C. H. *J. Catal.* **1984**, 87, 352.
8. Rofer-DePoorter, C. K. *Chem. Rev.* **1981**, 81, 447.
9. Dry, M. E.; Anderson, J. R.; Boudart, M. (Editor), Catalytic Activation of Carbon Dioxide, *Am. Chem. Soc. Symp. Ser*. **1988**. 336.
10. Tingey, G. L. *J. Phys. Chem.* **1987**, 70, 1406.
11. Bustamante, F.; Enick, R.; Rothenberger, K.; Howard, B.; Cugini, A.; Ciocco, M.; Morreale, B. *Fuel Chem. Div. Prepr.* **2002**, 47, 663.
12. Ginés, M. J. L.; Marchi, A. J.; Apesteguía, C. R. Catalysts. *Appl. Catal. A Gen.* **1997**, 154, 155.
13. Romm, L.; Kim, Y. H.; Somorjai, G. A. *J. Phys. Chem. A* **2001**, 105, 7025.
14. Chen, P.; Colson, S. D.; Chupka, W. A.; Berson, J. A. *J. Phys. Chem.* **1986**, 90, 2319.

15. Minsek, D. W.; Chen, P. *J. Phys. Chem.* **1990**, 94, 8399.

16. Rohrs, H. W.; Wickhamjones, C. T.; Ellison, G. B.; Berry, D.; Argrow, B. M. *Rev. Sci. Instrum.* **1995**, 66, 2430.

17. Shebaro, L.; Bhalotra, S. R.; Herschbach, D. *J. Phys. Chem. A* **1997**, 101, 6775.

18. Stirniman, M. J.; Li, W.; Sibener, S. J. *J. Chem. Phys.* **1995**, 103, 451.

19. Yuan, H.; Killelea, D. R.; Tepavcevic, S.; Kelber, S. I.; Sibener, S. J. *J. Phys. Chem. A* **2011**, 115, 3736.

20. Miller, D. R. *Rev. Sci. Instrum.* **1969**, 40, 1566.

21. Sibener, S. J.; Richard, B. J.; Cheuk, Y. N.; Lee, Y. T. *Rev. Sci. Instrum.* **1980**, 51, 167.

22. Graven, W. M.; Long, F. J. *J. Am. Chem. Soc.* **1954**, 76, 2602.

23. Romm, L.; Somorjai, G. A. *Catal. Letters* **2000**, 64, 85.

24. Valnnice, M. A., Kinetics of Catalytic Reactions. Springer, New York, 2005

25. Smith, B, *Int. J. Chem. React. Eng.* **2010**, 8, 1.

26. Beavis, L. C. *J. Vac. Sci. technol*. **1973**, 10, 386.

27. Killeen, J. C., Smith, A. F., Wild, R. K. *Corros. Sci.* **1976**, 16, 551.

28. Park, R. L., Houston, J. E., Schreiner, D. G. *J. Vac. Sci. Technol.* **1972**, 9, 1023.

29. Tanabe, T., Imoto, S. *Trans. Jpn. Inst. Metal.* **1979**, 20, 507.

30. Smith, B., Loganathan, M., Shantha, M. S. *Int. J. Chem. React. Eng.* **2010**, 8, R4.

31. Kurtz, R. L., Henrich, V. E. *Phys. Rev. B* **1987**, 36, 3413.

32. Henrich, V. E., Cox, P. A. The surface Science of Metal Oxides. Cambridge University Press, Cambridge, 1994, Chapter 6.

33. Grenoble, D. C., Edstadt, M. M., Ollis, D. F. *J. Catal.*, **1981**, 67, 90.

34. Scoles, G. Atomic and Molecular Beam Methods. Volume I. Oxford University Press, Oxford, 1988.

APPENDIX

Supplementary Figures

Figures showing the IR and TOF spectra to generate figures presented in previous chapters.

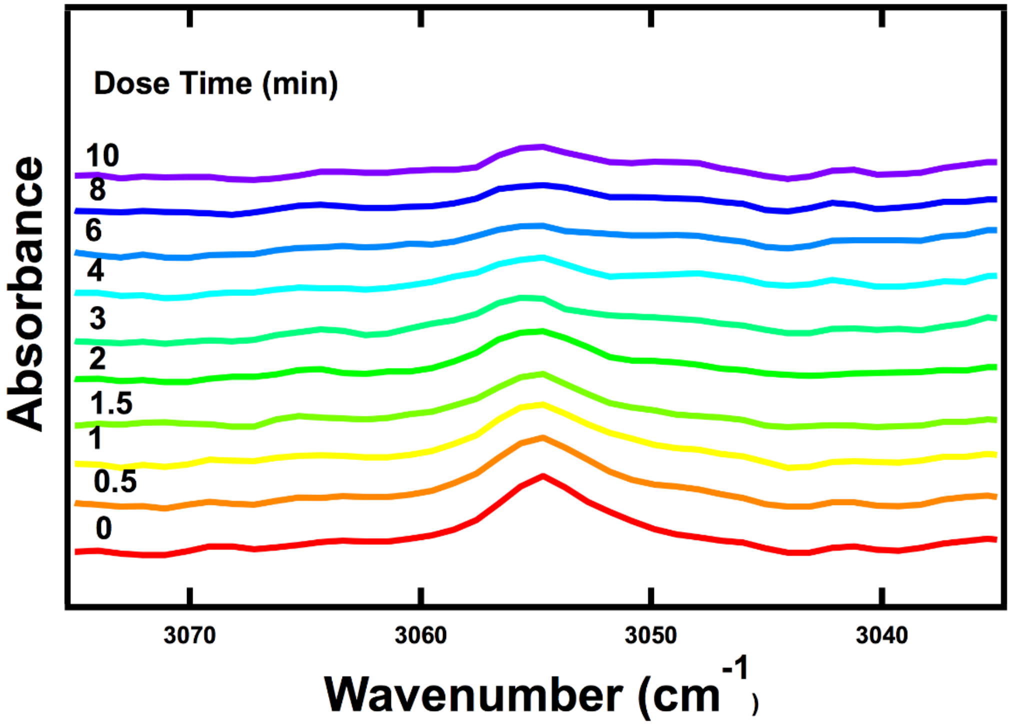

Figure A.1. RAIR spectra of oPE monolayer versus O(^{3}P) exposure of ~4 x 10^{15} O(^{3}P)/cm^2. It indicates decay of the C-H stretching mode intensity at 3055 cm^{-1}. From bottom to top are the spectra from unreacted SAM to reacted SAM with O(^{3}P) exposure up to 10 minutes.

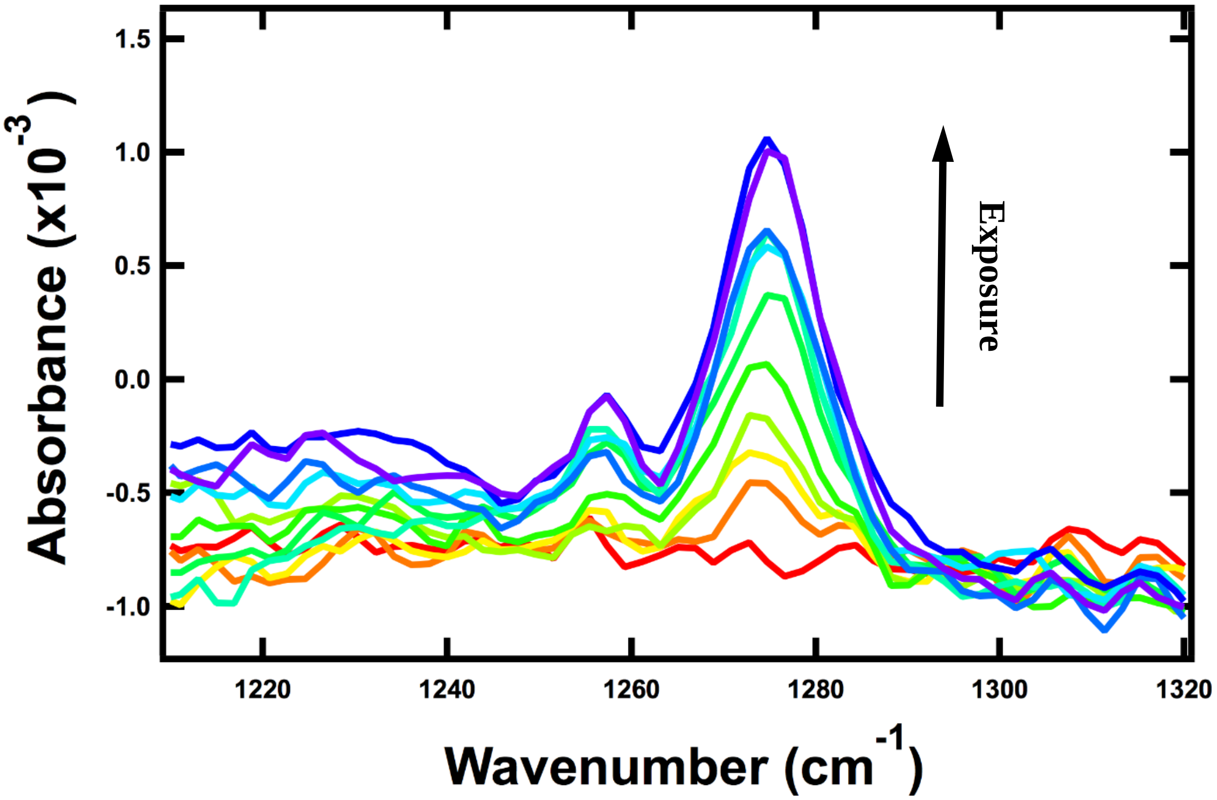

Figure A.2. Energetic ballistic deposition of 4.1 eV CF_4 into ASW ice is characterized by the appearance of RAIRS peaks at 1276 and 1257 cm^{-1}, the intensity of which increases linearly with respect to the total amount of CF_4 dosed onto the surface at normal incidence.

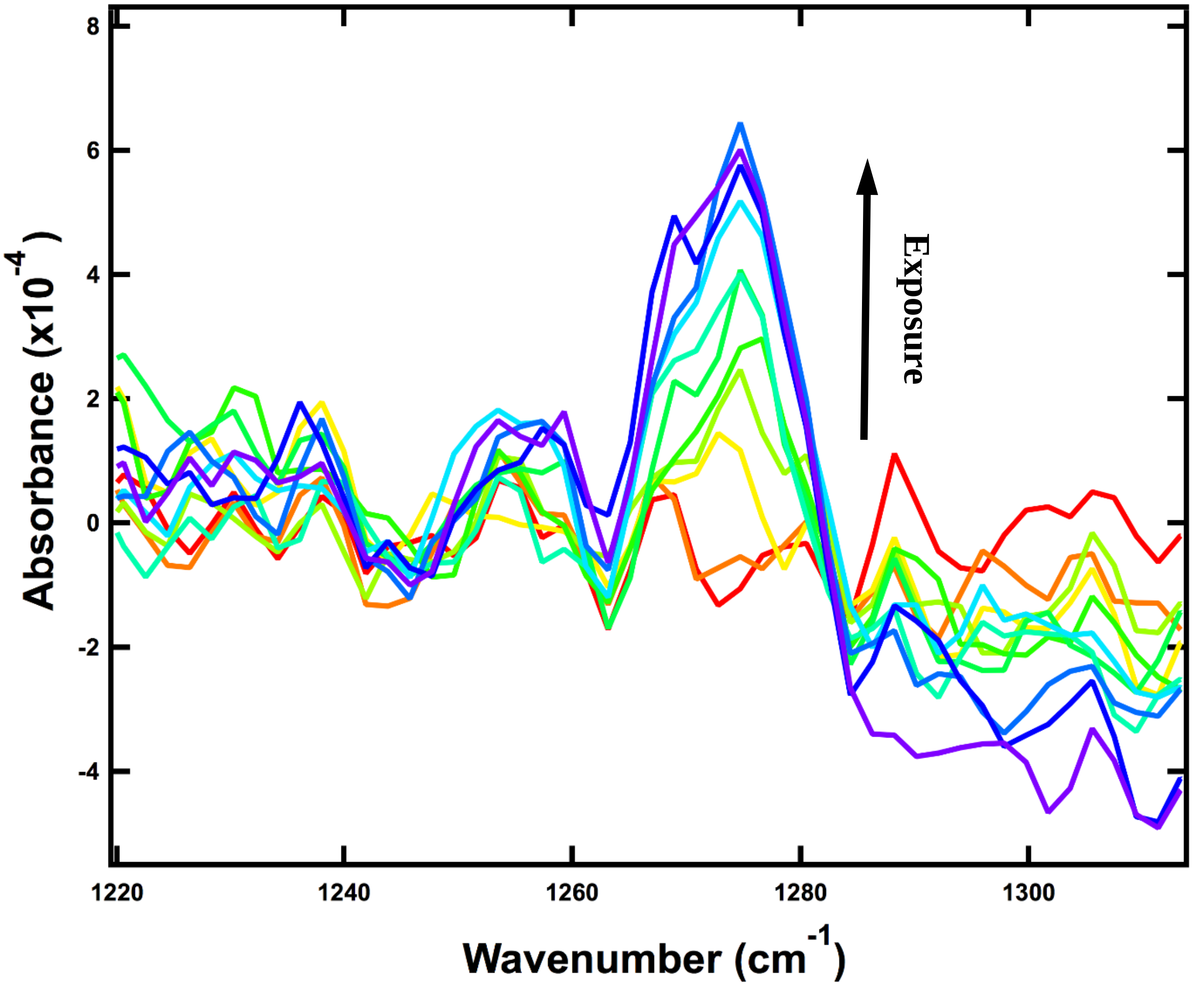

Figure A.3. Energetic ballistic deposition of 3.7 eV CF_4 into ASW ice is characterized by the appearance of RAIRS peaks at 1276 and 1257 cm^{-1}, the intensity of which increases linearly with respect to the total amount of CF_4 dosed onto the surface at normal incidence.

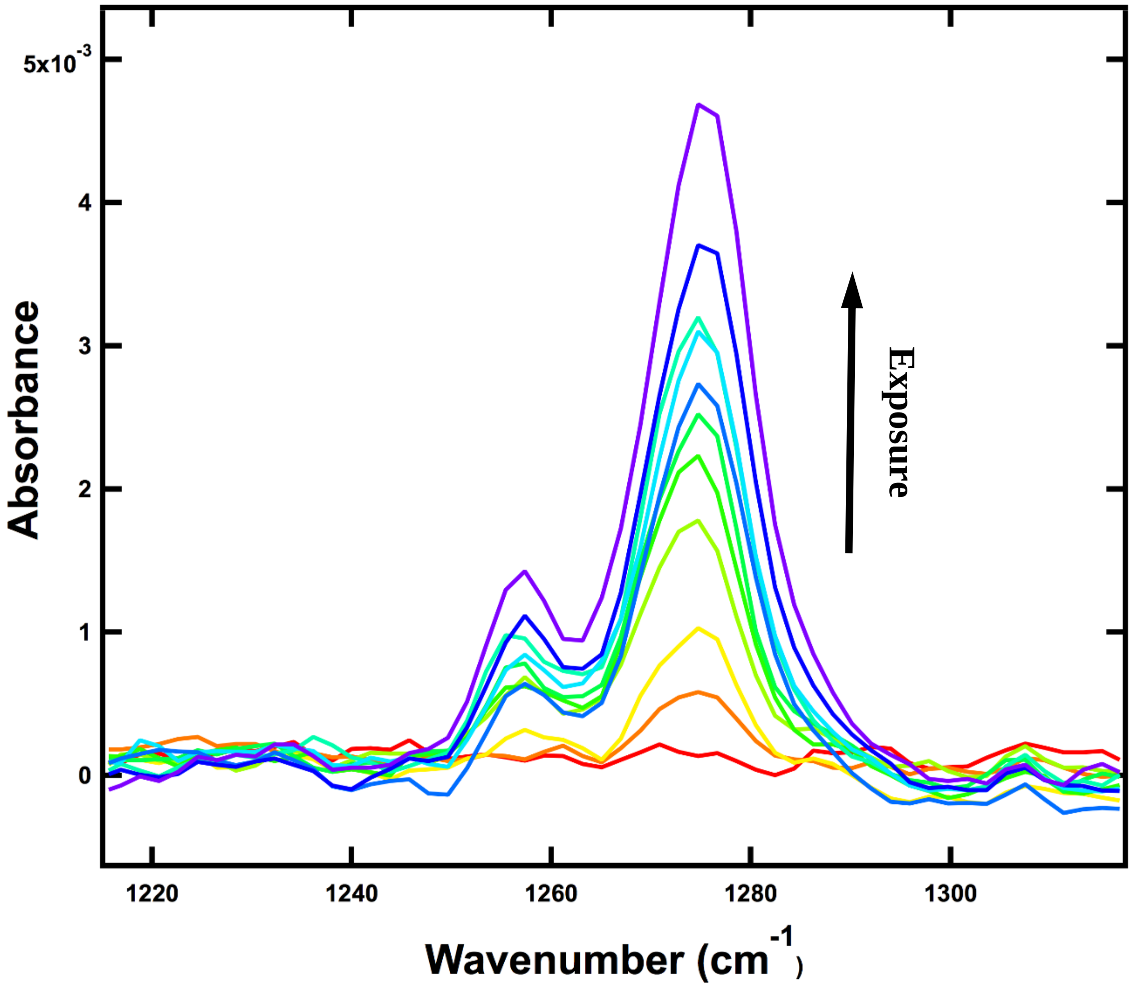

Figure A.4. Energetic ballistic deposition of 4.7 eV CF_4 into ASW ice is characterized by the appearance of RAIRS peaks at 1276 and 1257 cm^{-1}, the intensity of which increases linearly with respect to the total amount of CF_4 dosed onto the surface at normal incidence.

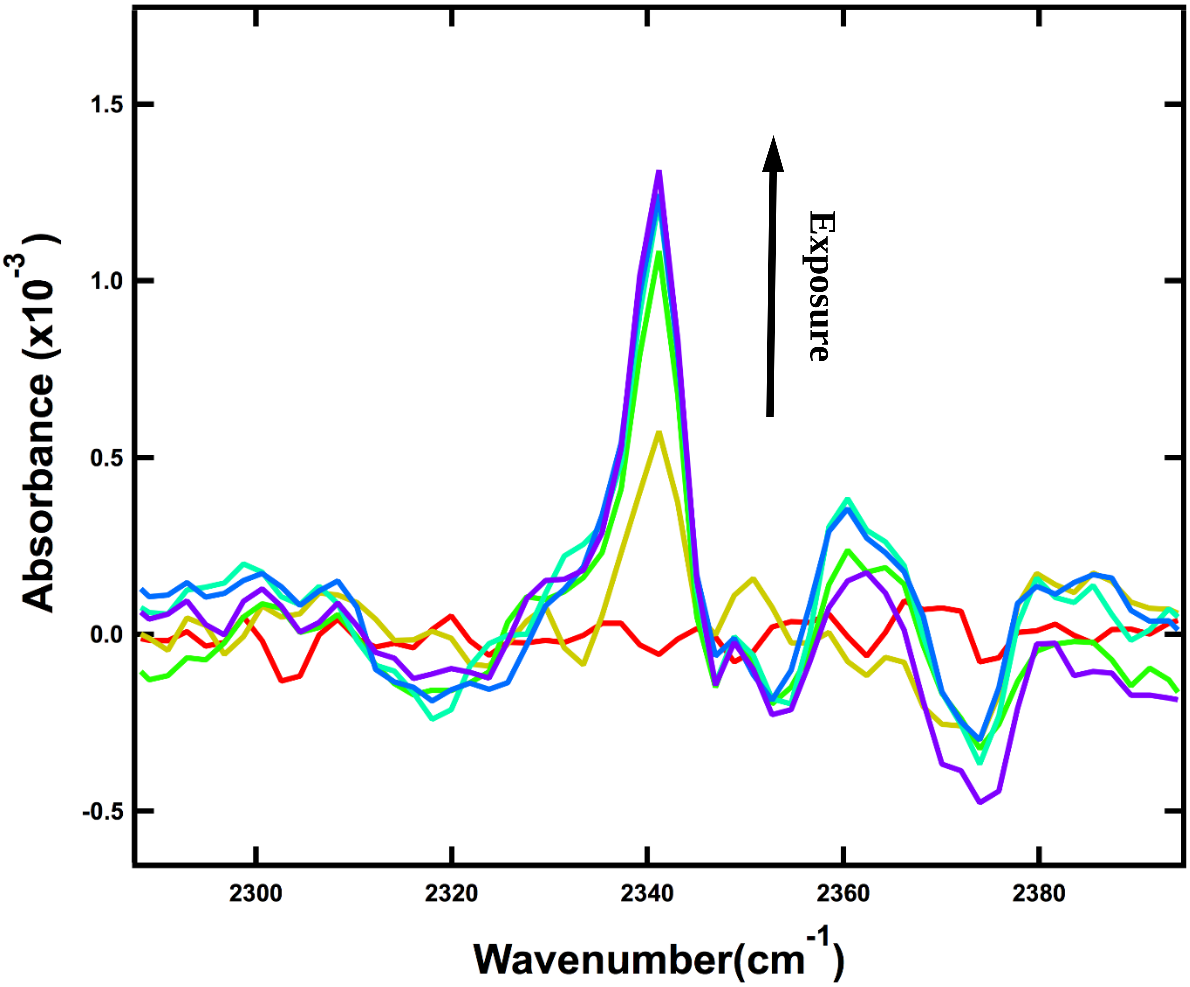

Figure A.5. RAIRS signals obtained during exposure to a 3.0 eV seeded CO_2 beam into ASW ice.

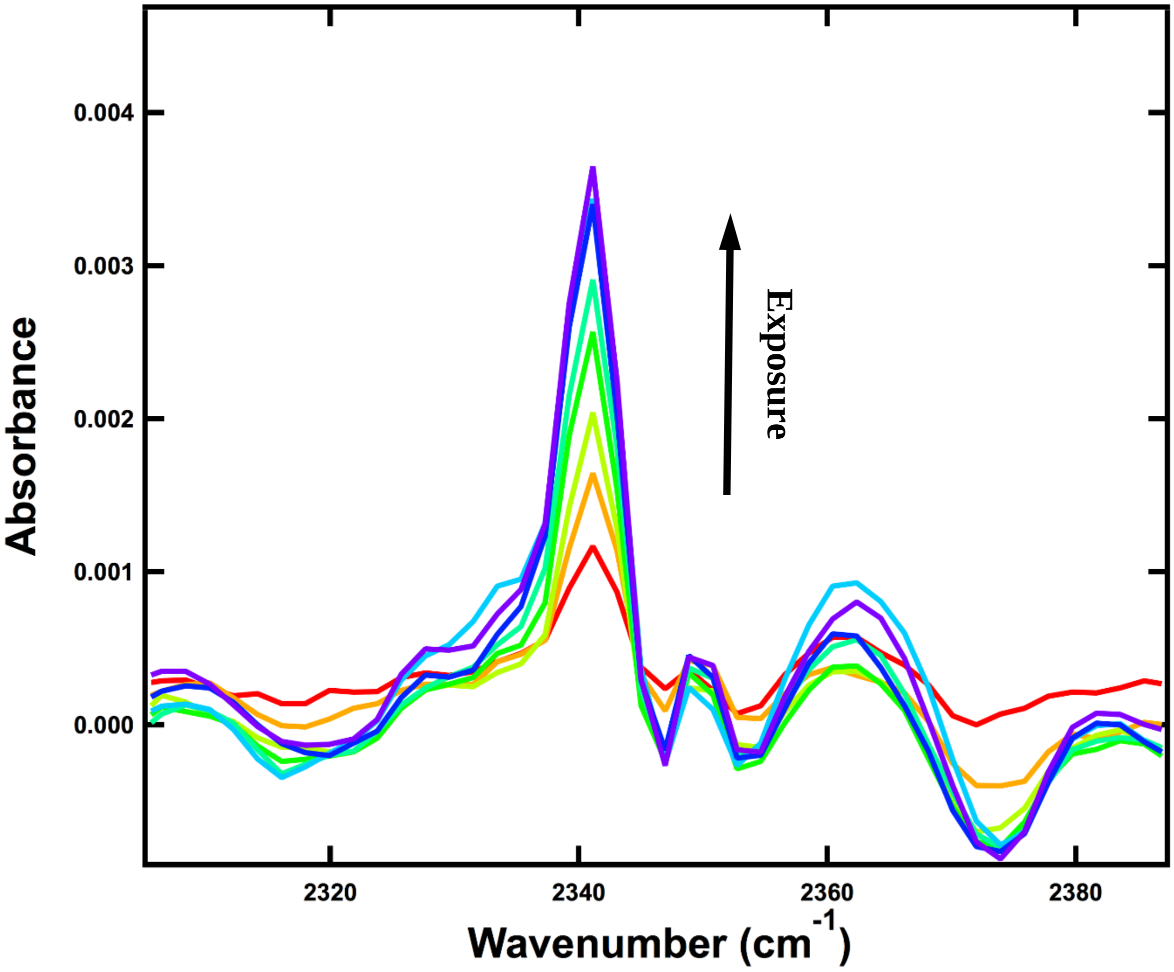

Figure A.6. RAIRS signals obtained during exposure to a 4.2 eV seeded CO_2 beam into ASW ice.

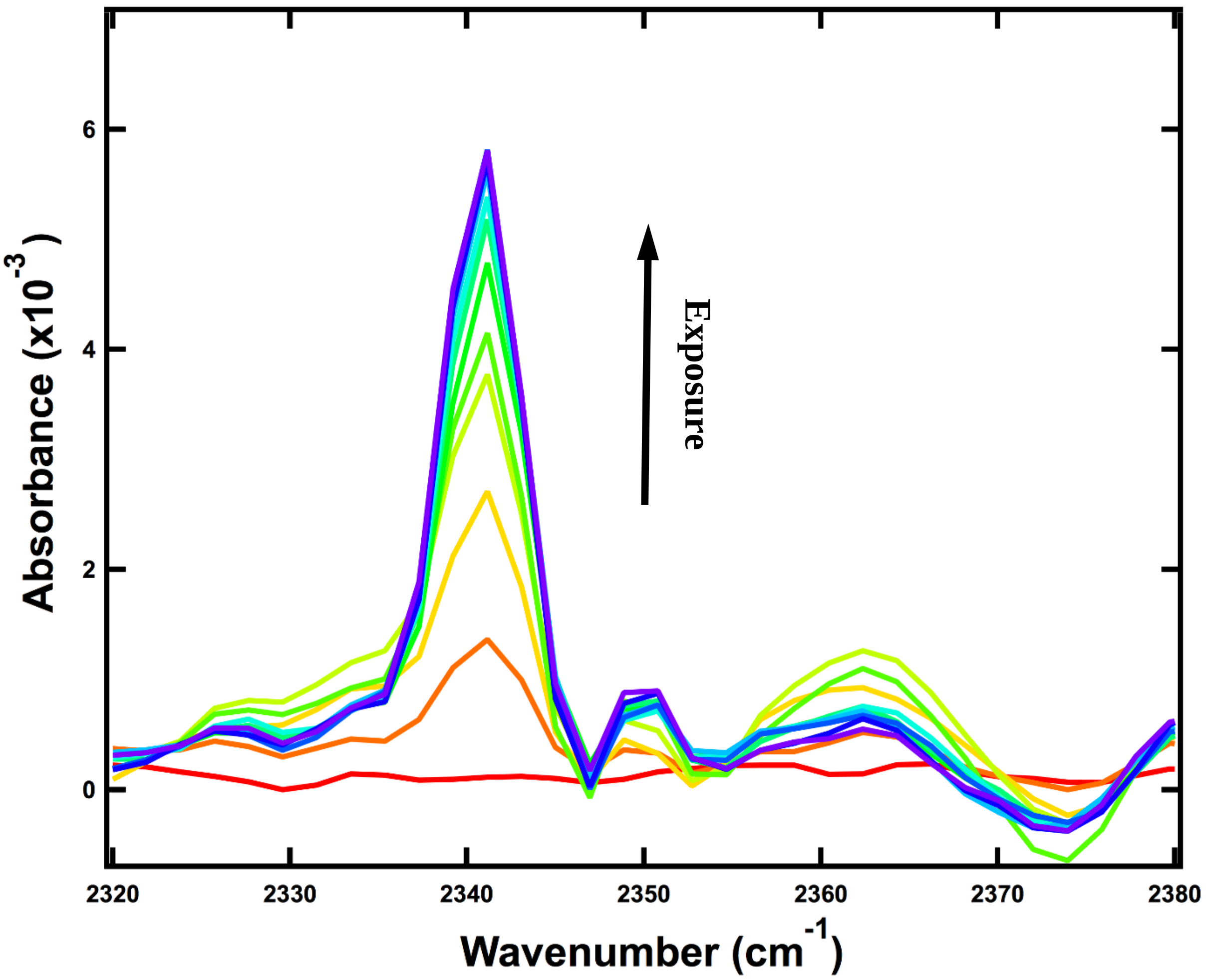

Figure A.7. RAIRS signals obtained during exposure to a 4.0 eV seeded CO_2 beam into ASW ice.

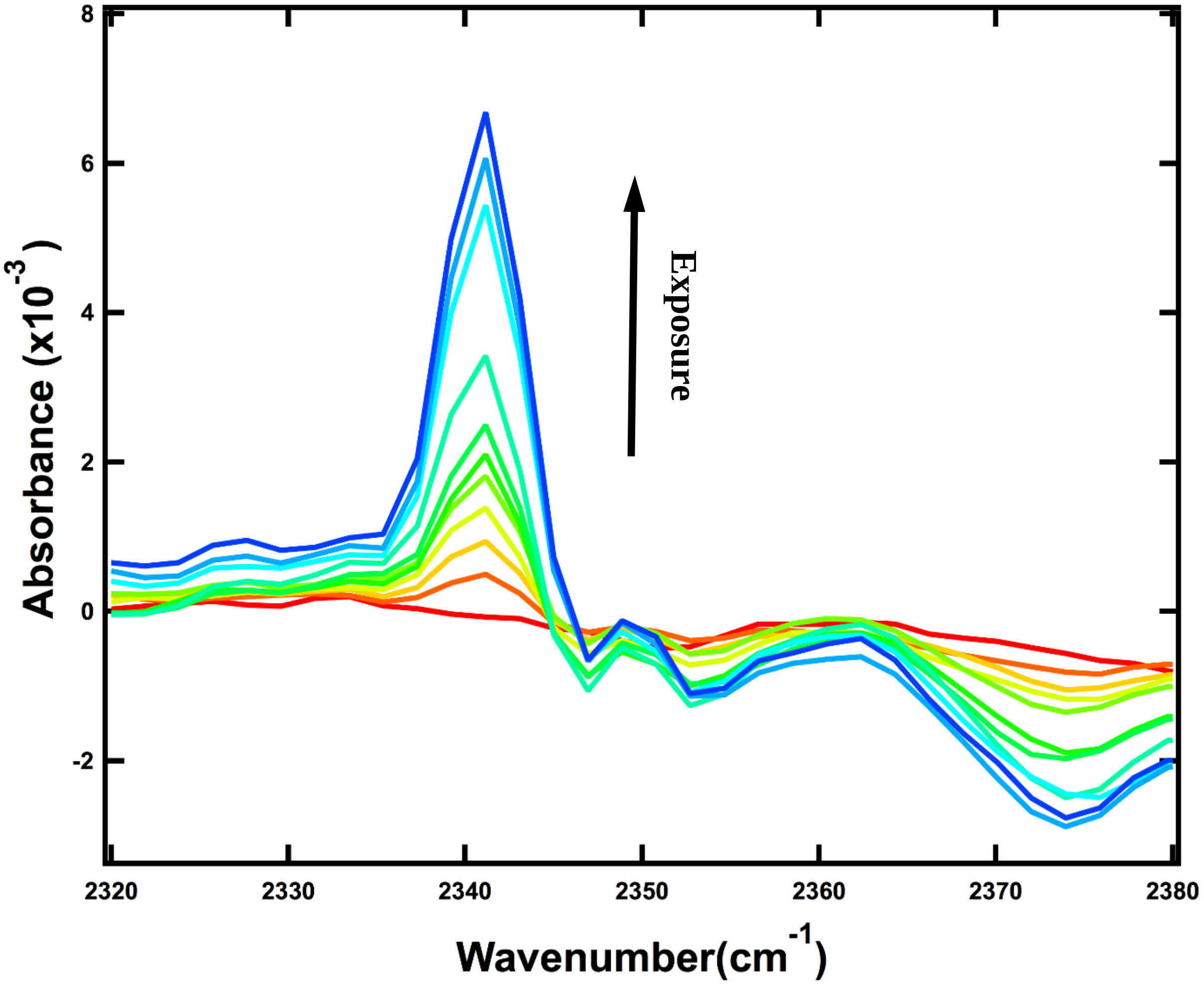

Figure A.8. RAIRS signals obtained during exposure to a 3.7 eV seeded CO_2 beam into ASW ice.

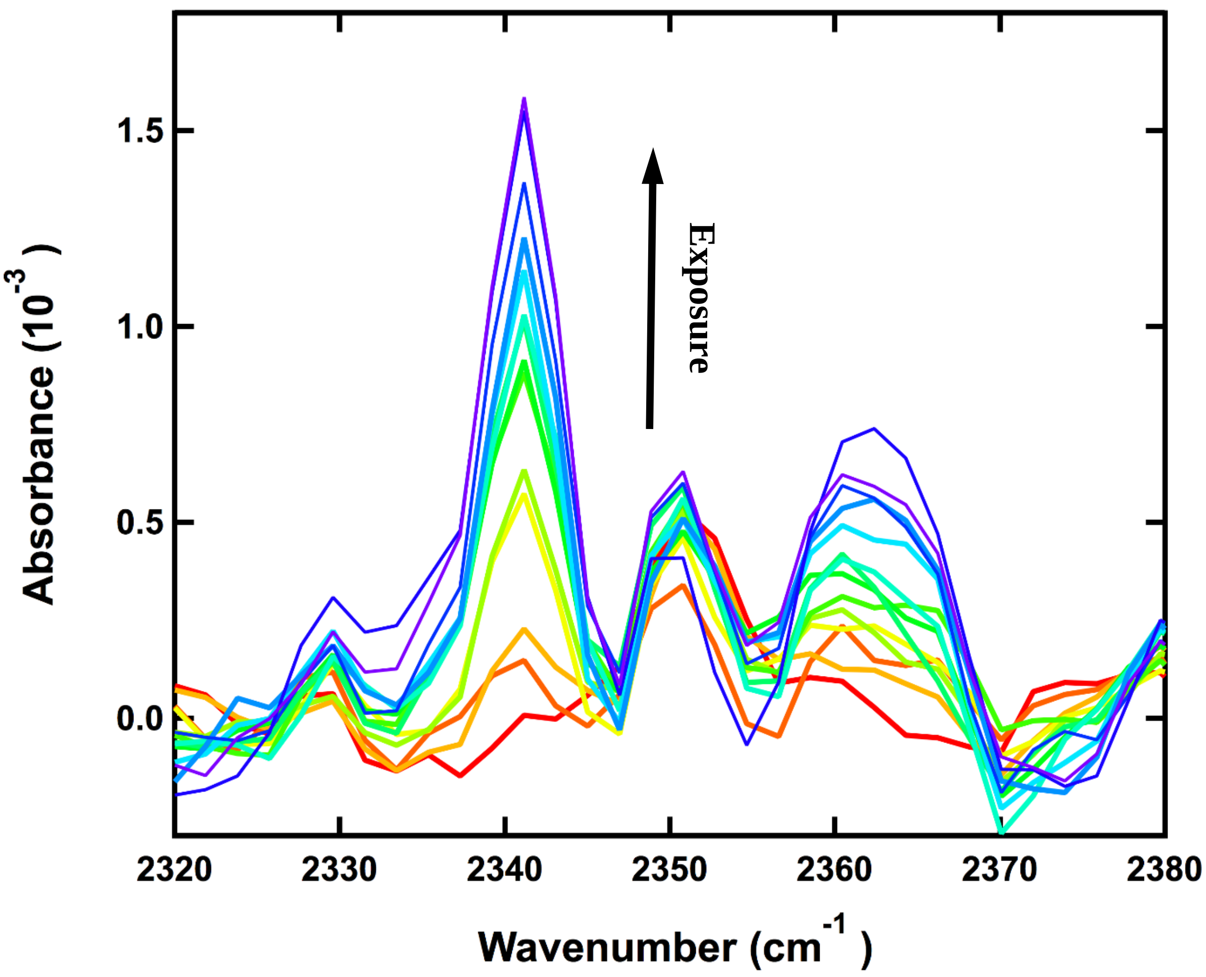

Figure A.9. RAIRS signals obtained during exposure to a 3.7 eV seeded CO_2 beam into ASW ice.

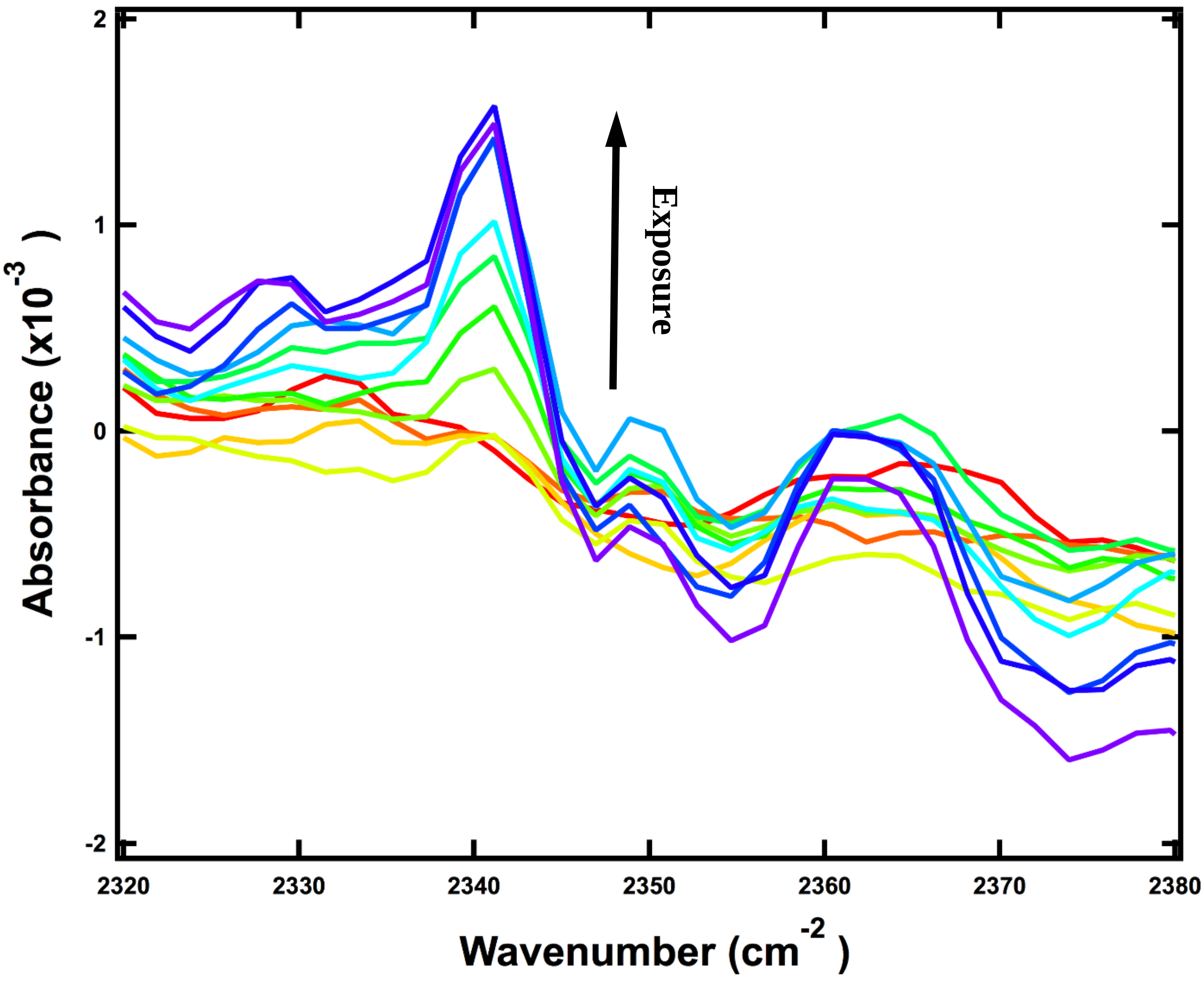

Figure A.10. E RAIRS signals obtained during exposure to a 3.4 eV seeded CO_2 beam into ASW ice.

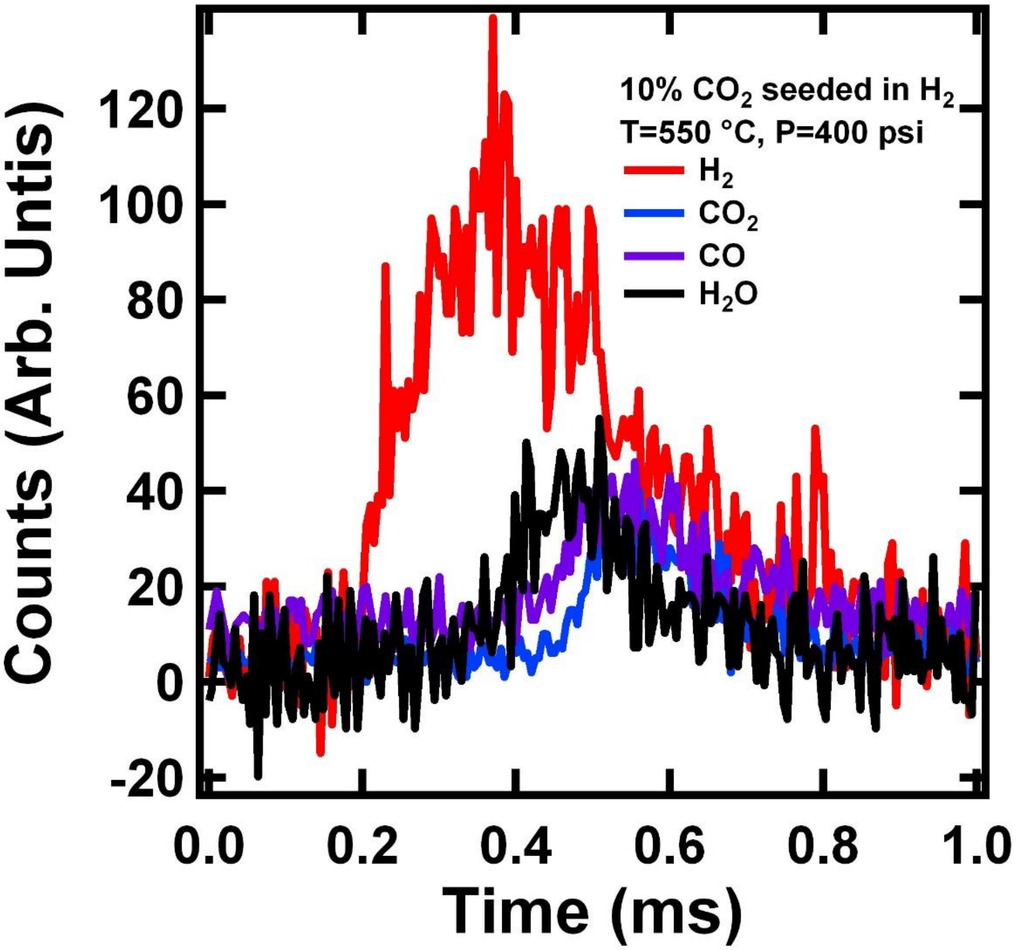

Figure A.11. TOF beam profiles for 10% CO_2 in H_2 gas mixtures at stagnation pressure 400 psi, with a nozzle temperature of 550 ℃. Spectra indicates H_2, CO_2, CO and H_2O gas species respectively.

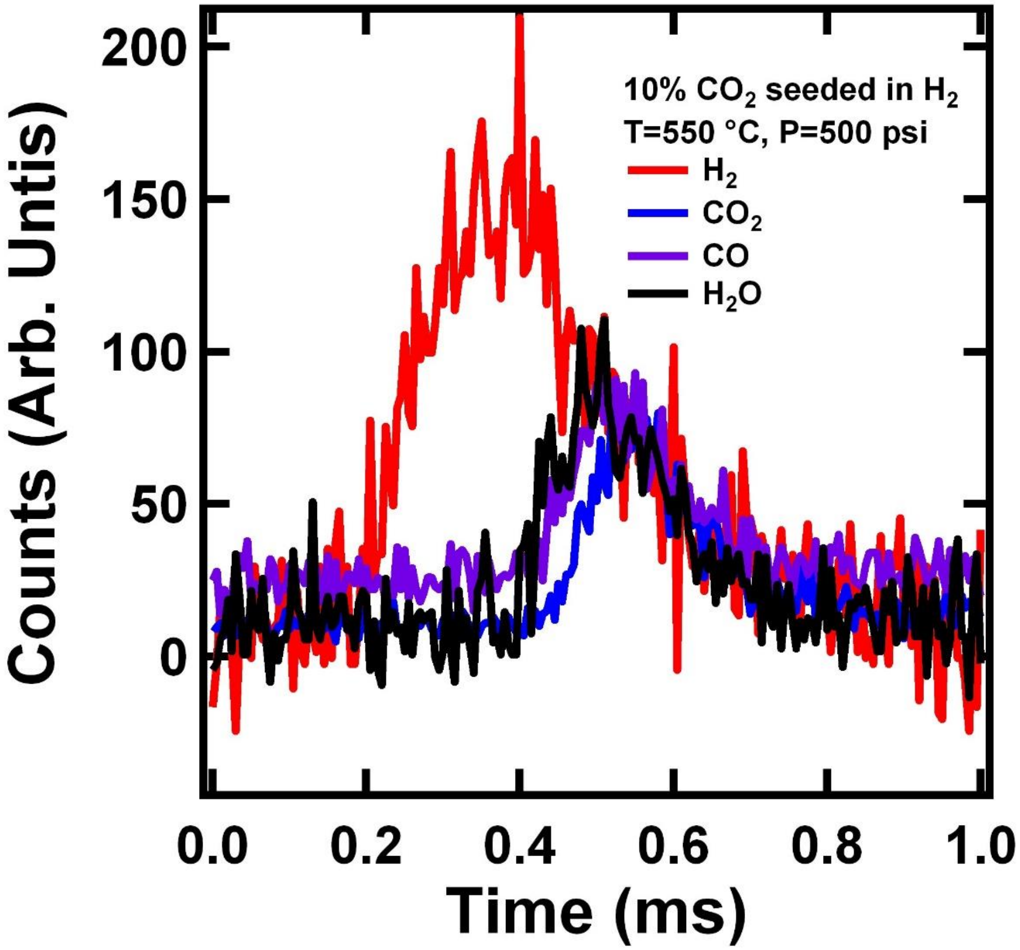

Figure A.12. TOF beam profiles for 10% CO_2 in H_2 gas mixtures at stagnation pressure 500 psi, with a nozzle temperature of 550 ℃. Spectra indicates H_2, CO_2, CO and H_2O gas species respectively.

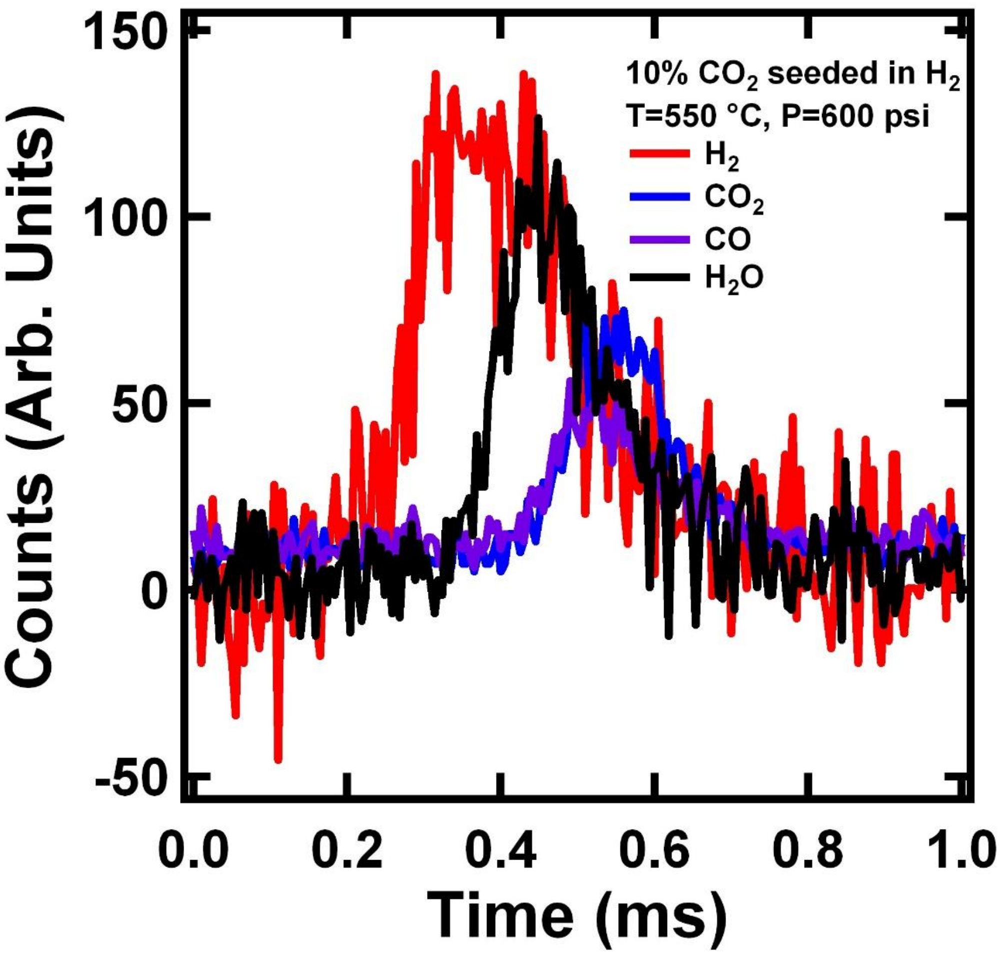

Figure A.13. TOF beam profiles for 10% CO2 in H2 gas mixtures at stagnation pressure 600 psi, with a nozzle temperature of 550 ℃. Spectra indicates H_2, CO_2, CO and H_2O gas species respectively.

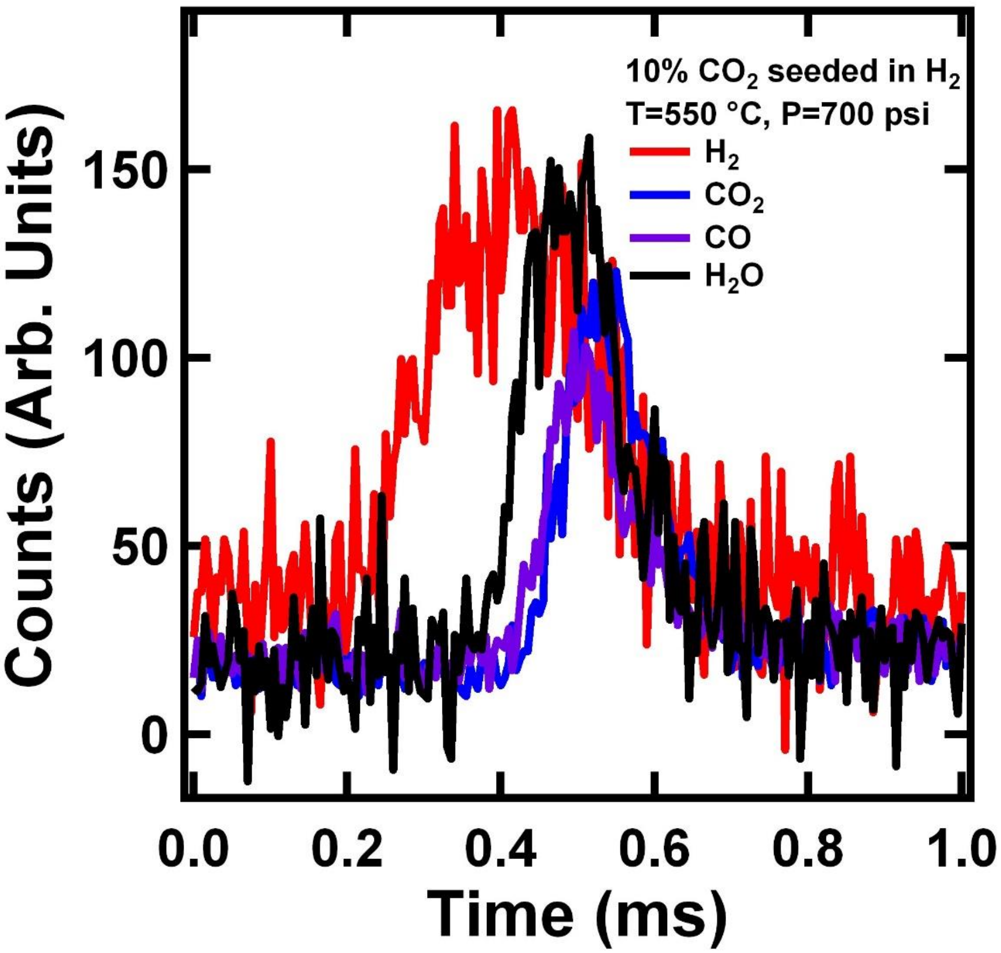

Figure A.14. TOF beam profiles for 10% CO_2 in H_2 gas mixtures at stagnation pressure 700 psi, with a nozzle temperature of 550 ℃. Spectra indicates H_2, CO_2, CO and H_2O gas species respectively.

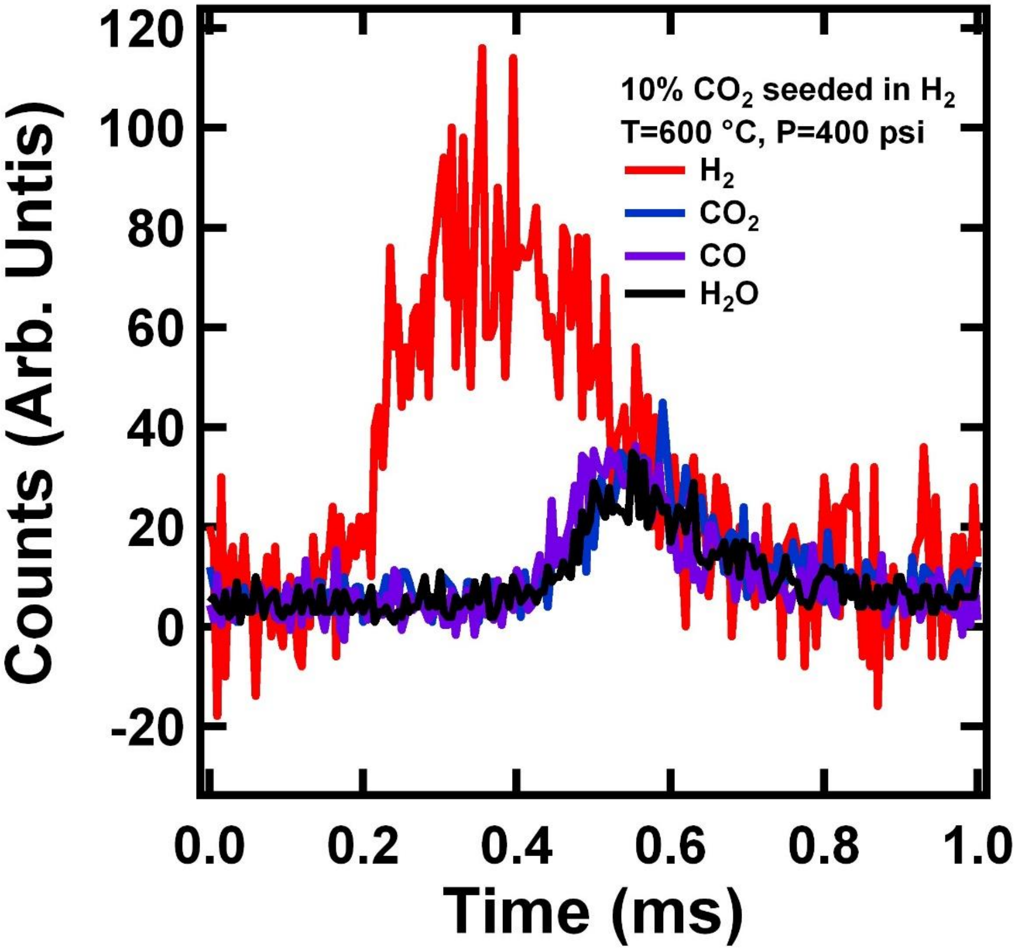

Figure A.15. TOF beam profiles for 10% CO_2 in H_2 gas mixtures at stagnation pressure 400 psi, with a nozzle temperature of 600 ℃. Spectra indicates H_2, CO_2, CO and H_2O gas species respectively.

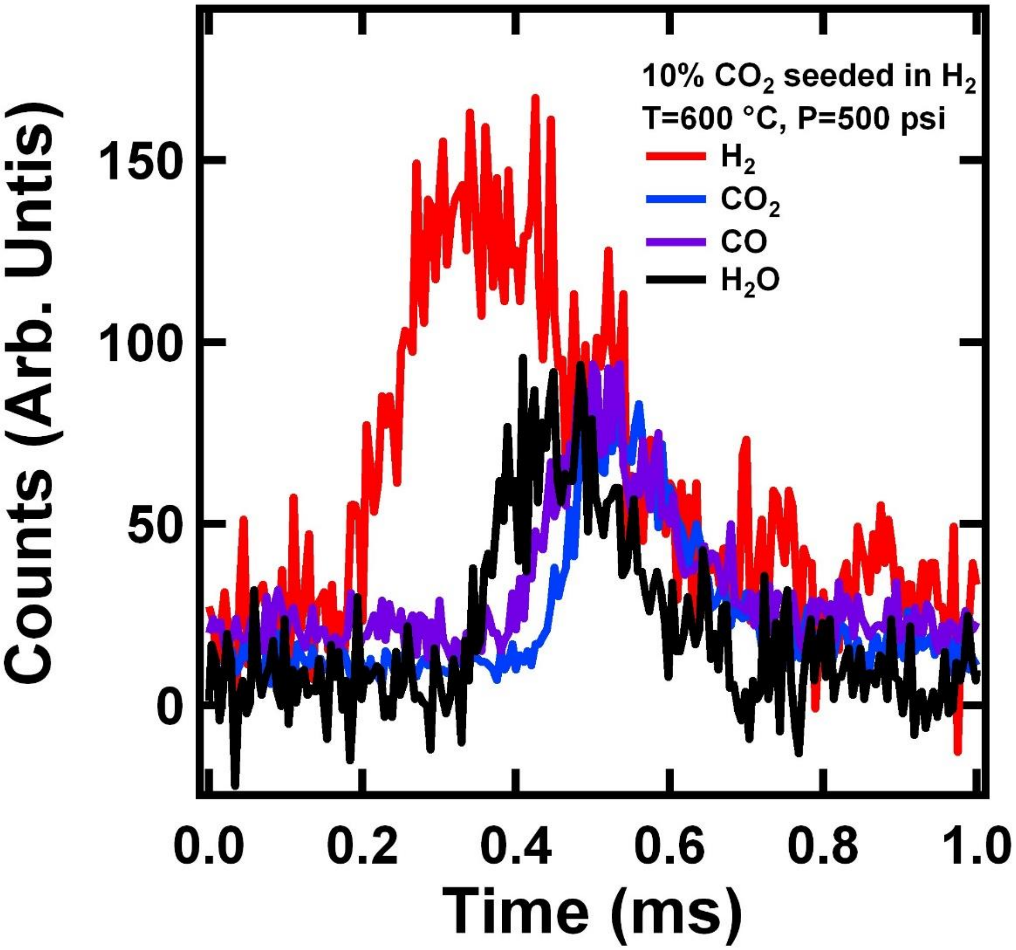

Figure A.16. TOF beam profiles for 10% CO_2 in H_2 gas mixtures at stagnation pressure 500 psi, with a nozzle temperature of 600 ℃. Spectra indicates H_2, CO_2, CO and H_2O gas species respectively.

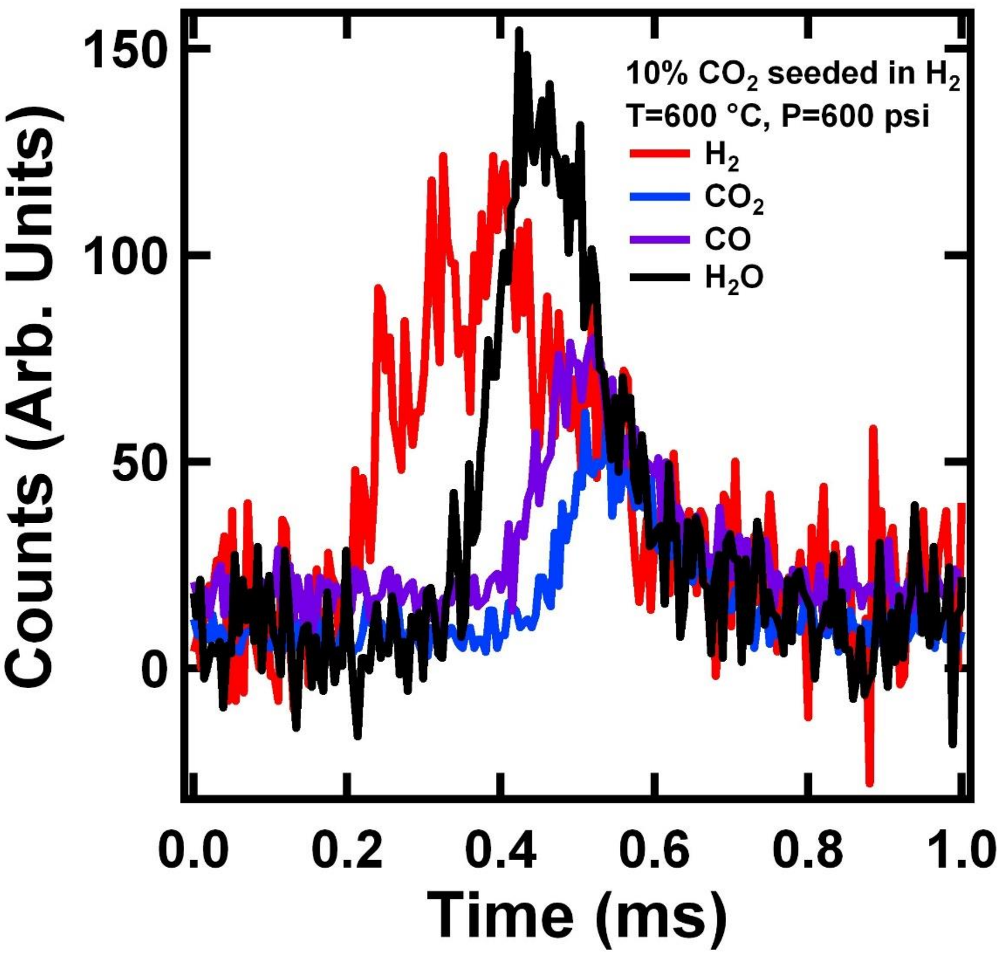

Figure A.17. TOF beam profiles for 10% CO_2 in H_2 gas mixtures at stagnation pressure 600 psi, with a nozzle temperature of 600 ℃. Spectra indicates H_2, CO_2, CO and H_2O gas species respectively.

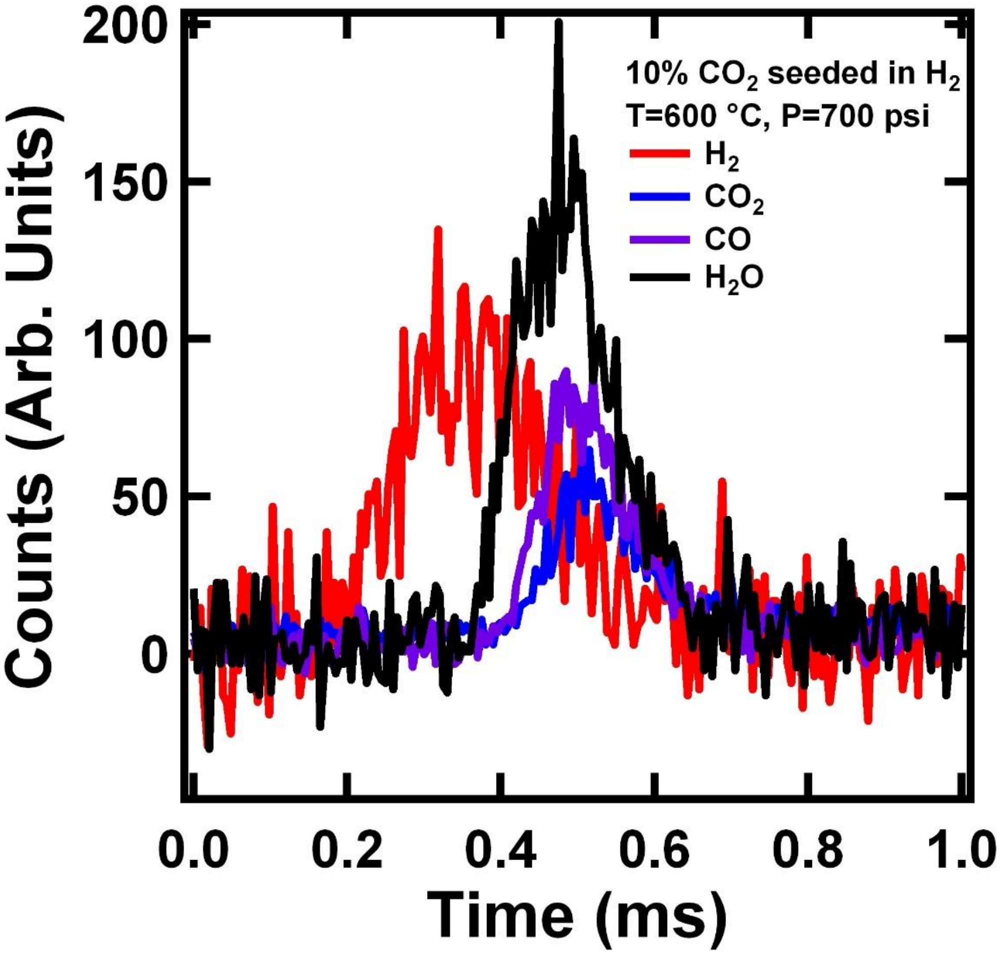

Figure A.18. TOF beam profiles for 10% CO_2 in H_2 gas mixtures at stagnation pressure 700 psi, with a nozzle temperature of 600 ℃. Spectra indicates H_2, CO_2, CO and H_2O gas species respectively.

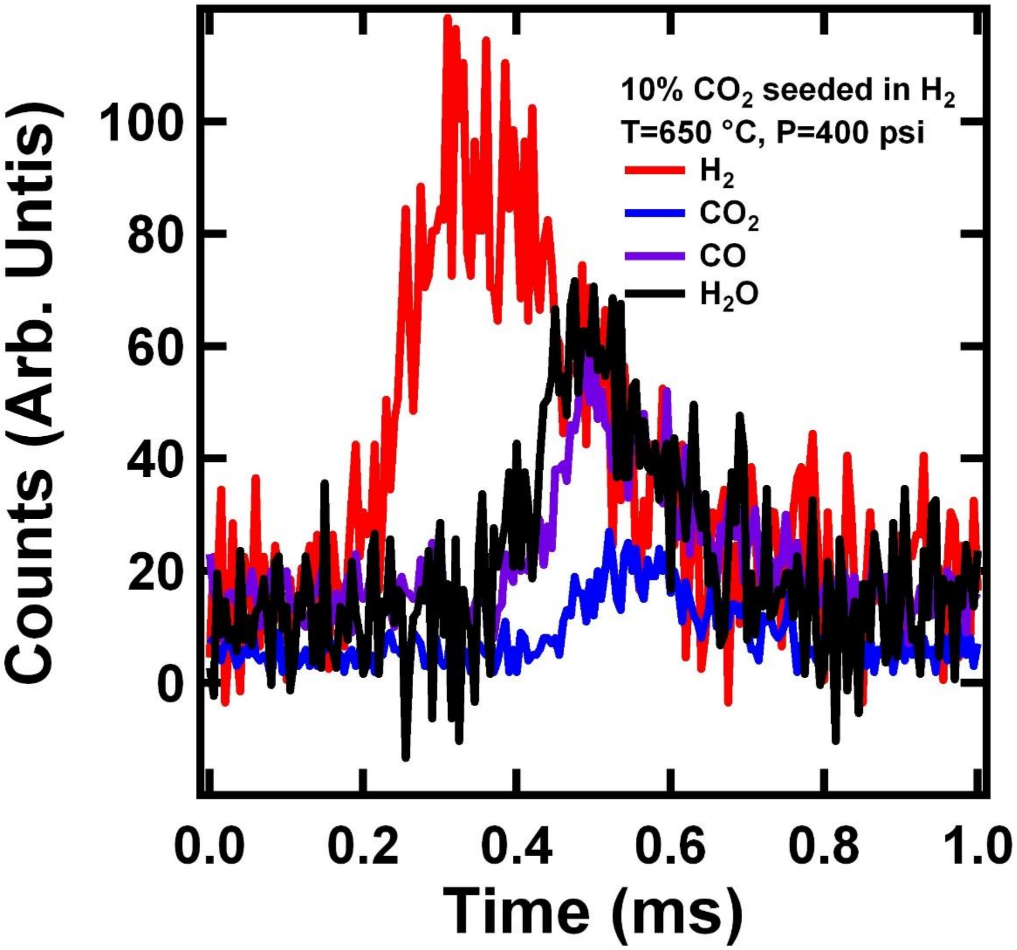

Figure A.19. TOF beam profiles for 10% CO_2 in H_2 gas mixtures at stagnation pressure 400 psi, with a nozzle temperature of 650 ℃. Spectra indicates H_2, CO_2, CO and H_2O gas species respectively.

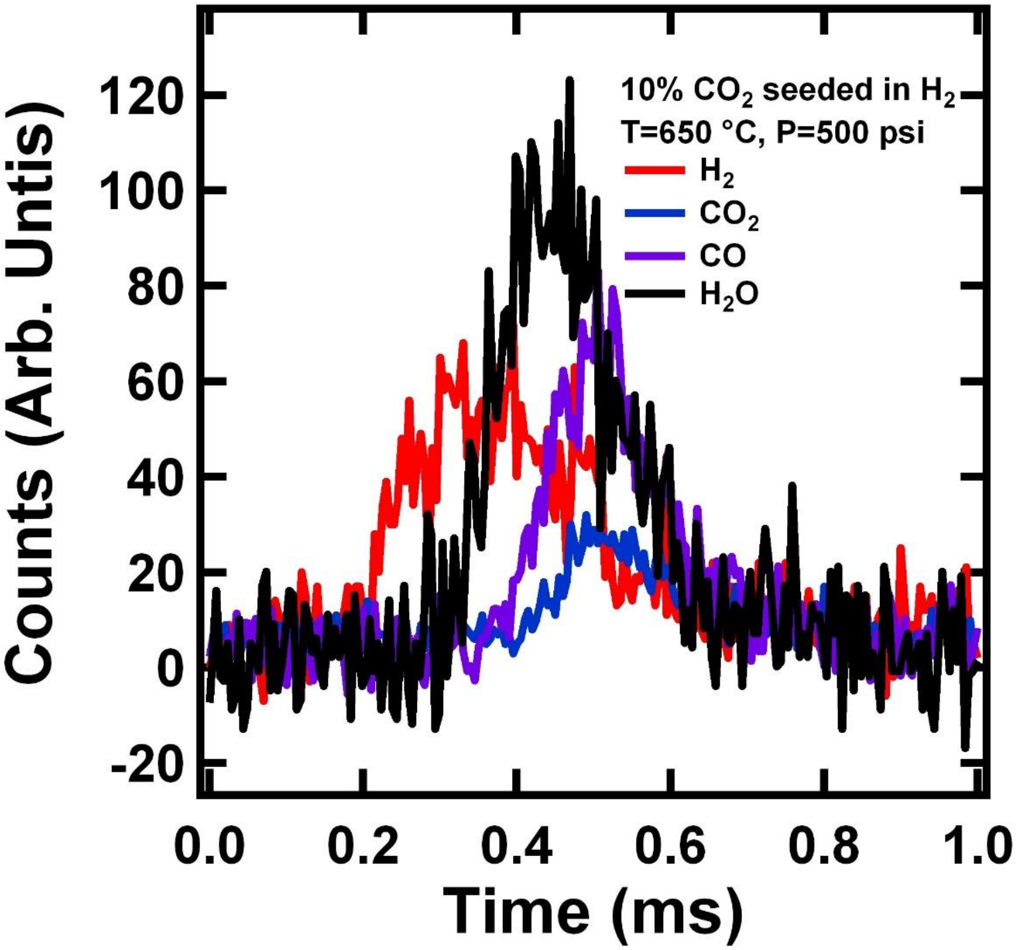

Figure A.20. TOF beam profiles for 10% CO_2 in H_2 gas mixtures at stagnation pressure 500 psi, with a nozzle temperature of 650 ℃. Spectra indicates H_2, CO_2, CO and H_2O gas species respectively.

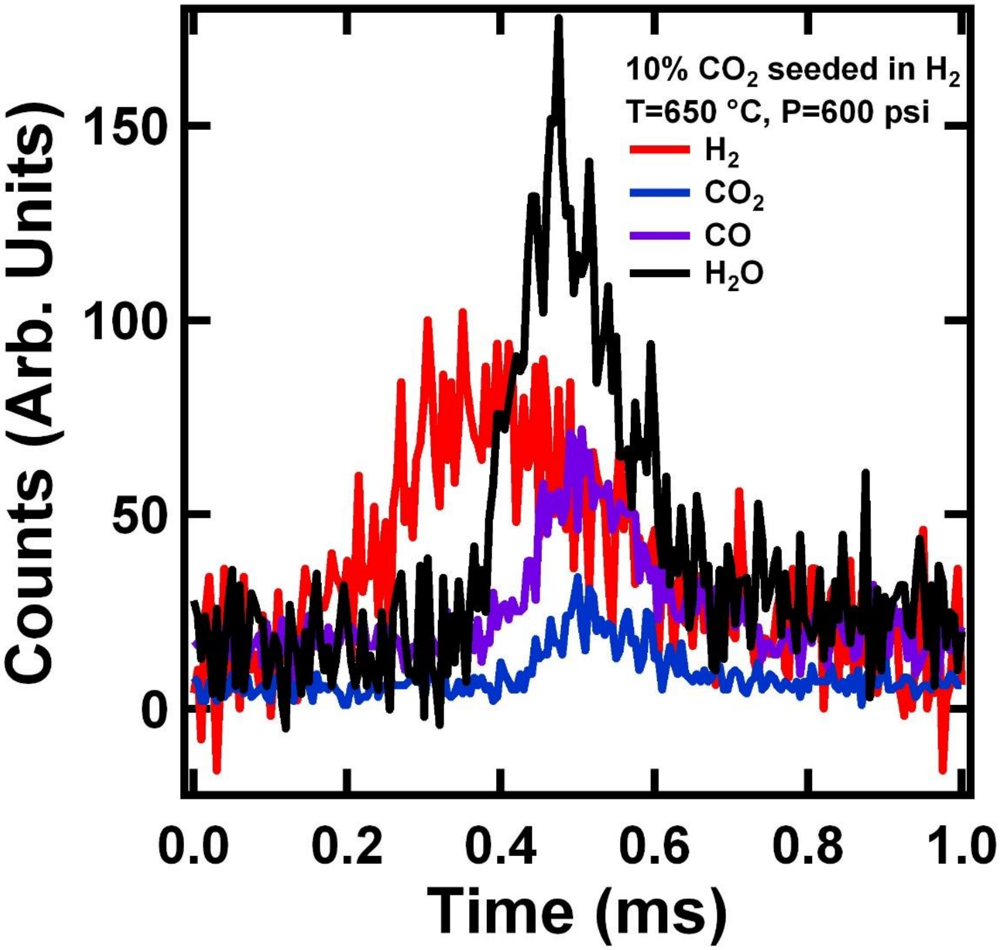

Figure A.21. TOF beam profiles for 10% CO_2 in H_2 gas mixtures at stagnation pressure 600 psi, with a nozzle temperature of 650 ℃. Spectra indicates H_2, CO_2, CO and H_2O gas species respectively.

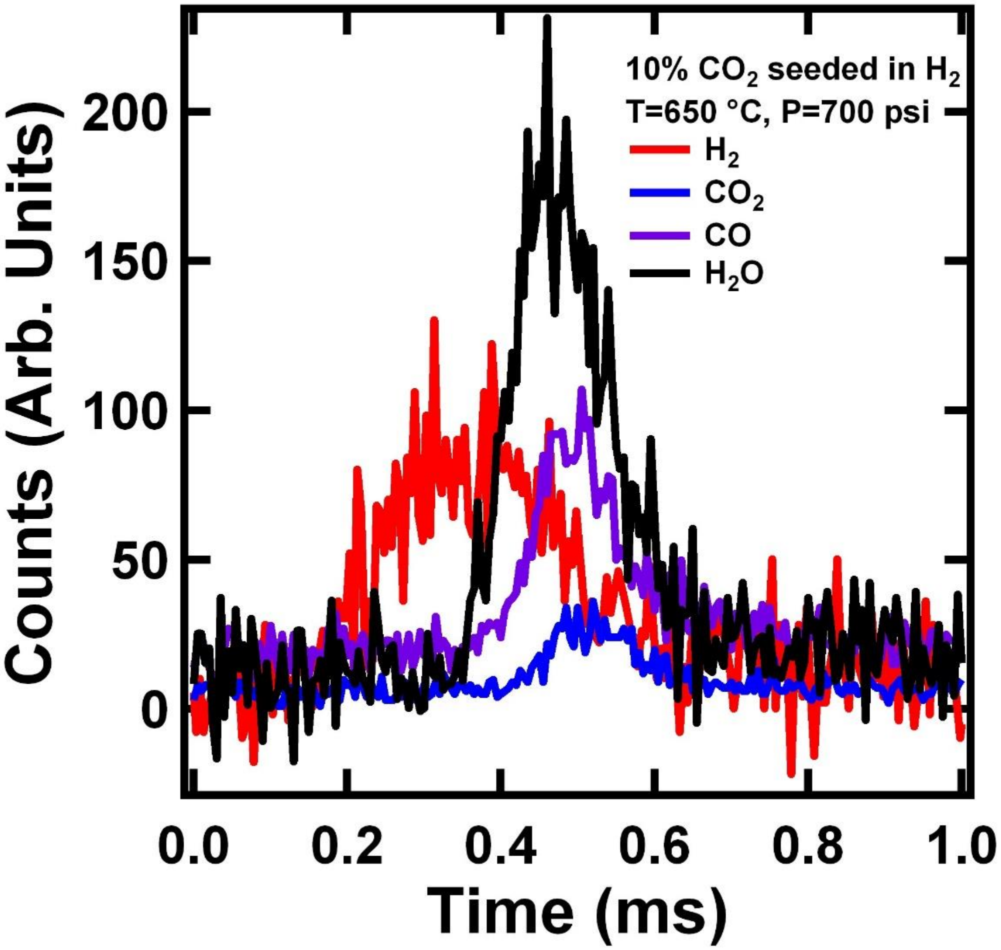

Figure A.22. TOF beam profiles for 10% CO_2 in H_2 gas mixtures at stagnation pressure 700 psi, with a nozzle temperature of 650 ℃. Spectra indicates H_2, CO_2, CO and H_2O gas species respectively.

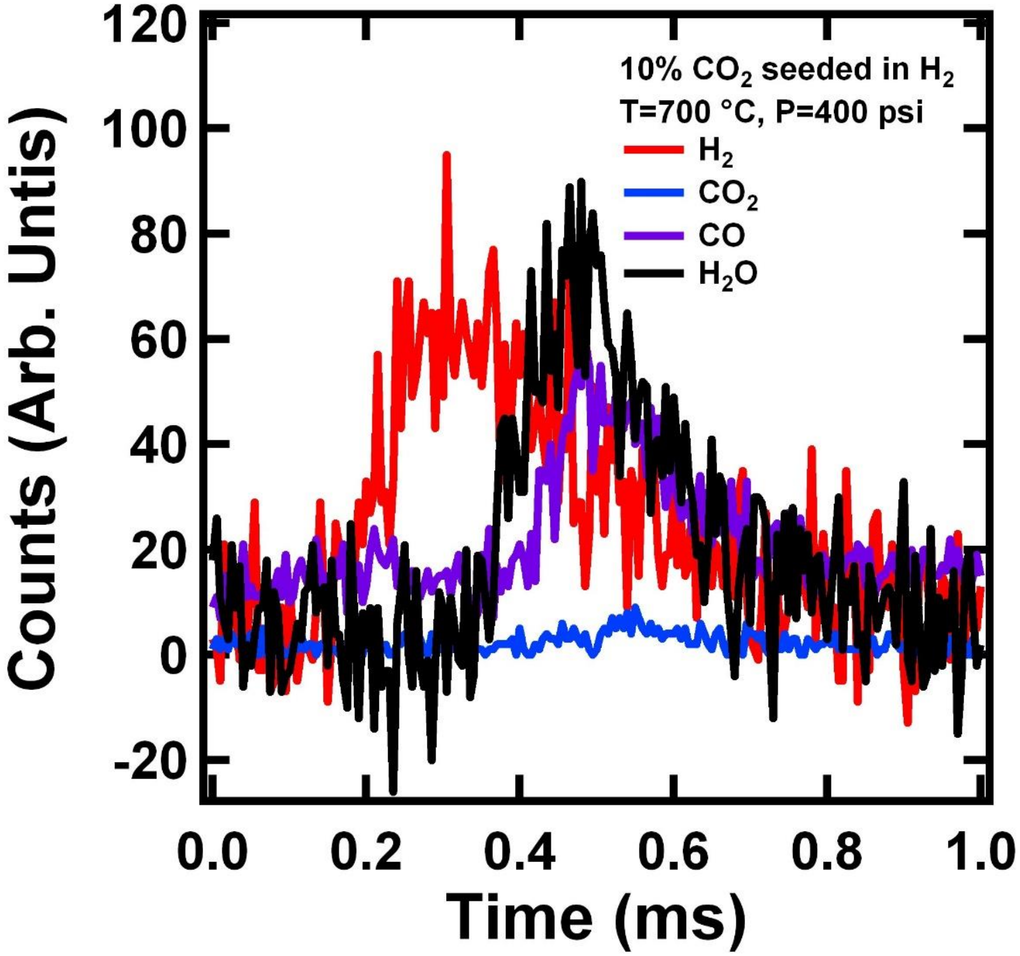

Figure A.23. TOF beam profiles for 10% CO_2 in H_2 gas mixtures at stagnation pressure 400 psi, with a nozzle temperature of 700 ℃. Spectra indicates H_2, CO_2, CO and H_2O gas species respectively.

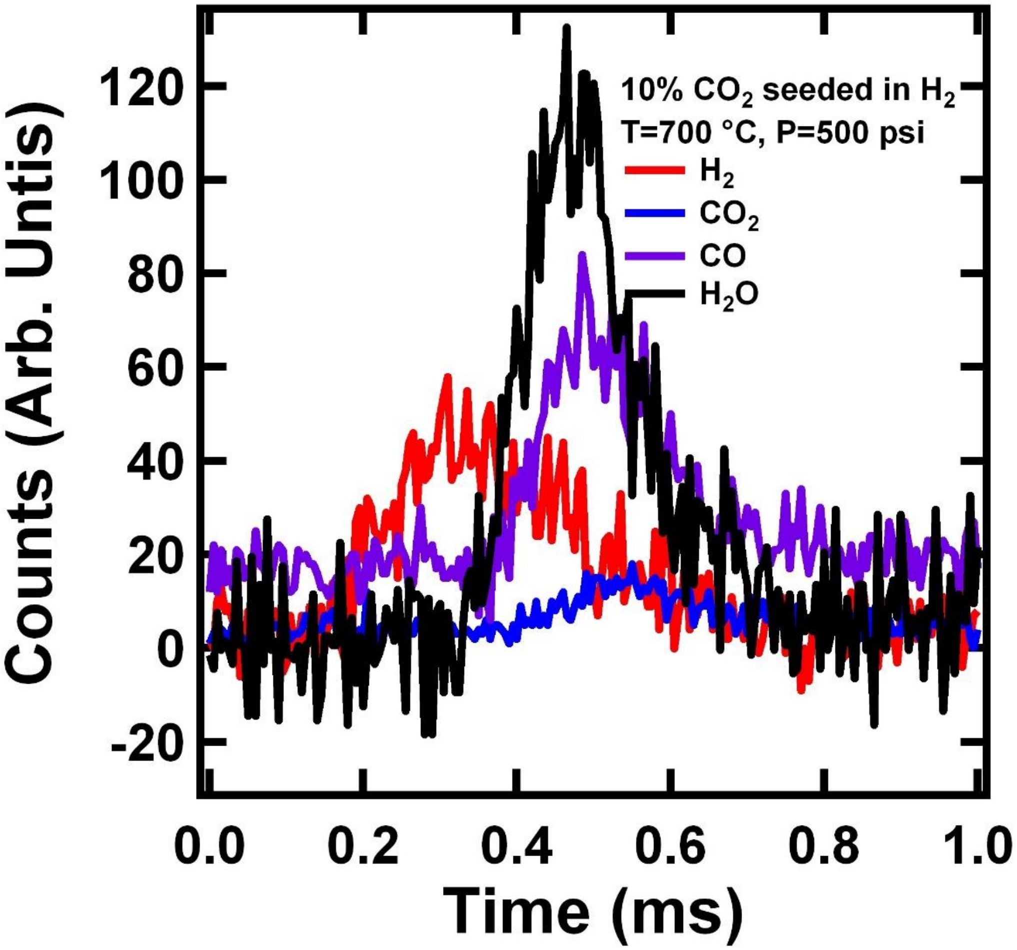

Figure A.24. TOF beam profiles for 10% CO_2 in H_2 gas mixtures at stagnation pressure 500 psi, with a nozzle temperature of 700 ℃. Spectra indicates H_2, CO_2, CO and H_2O gas species respectively.

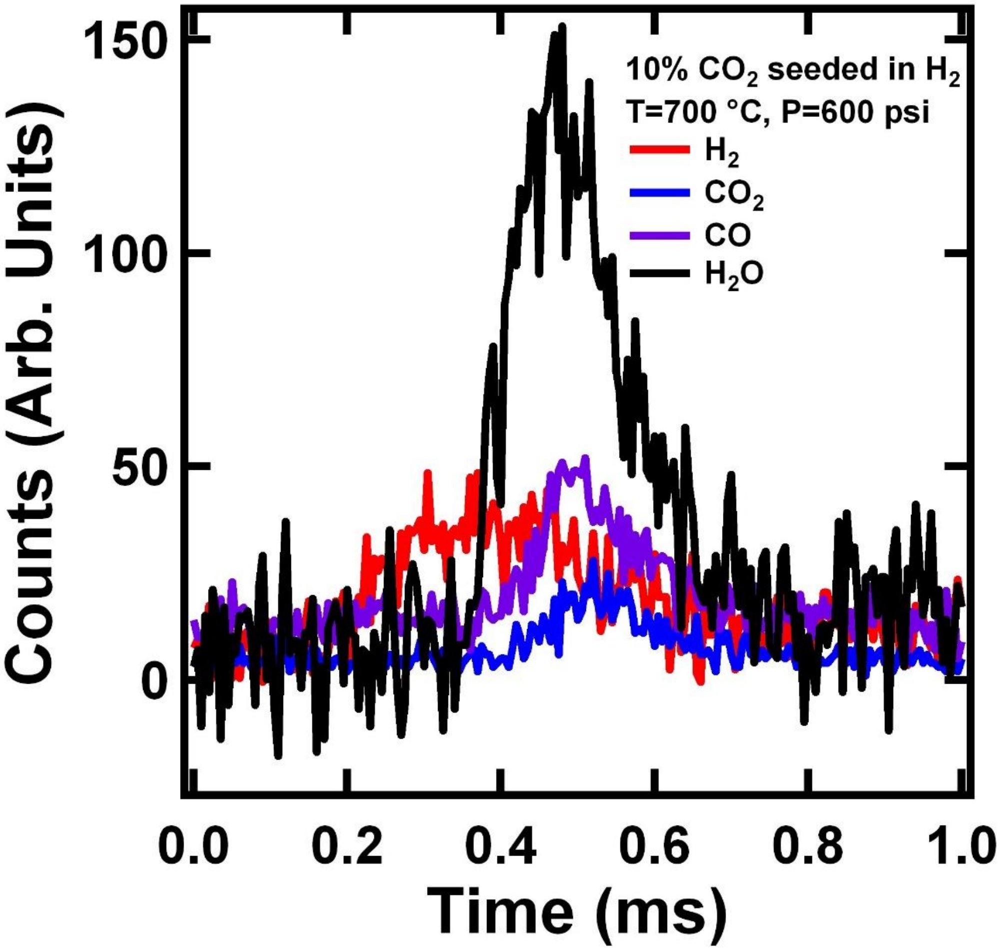

Figure A.25. TOF beam profiles for 10% CO_2 in H_2 gas mixtures at stagnation pressure 600 psi, with a nozzle temperature of 700 ℃. Spectra indicates H_2, CO_2, CO and H_2O gas species respectively.

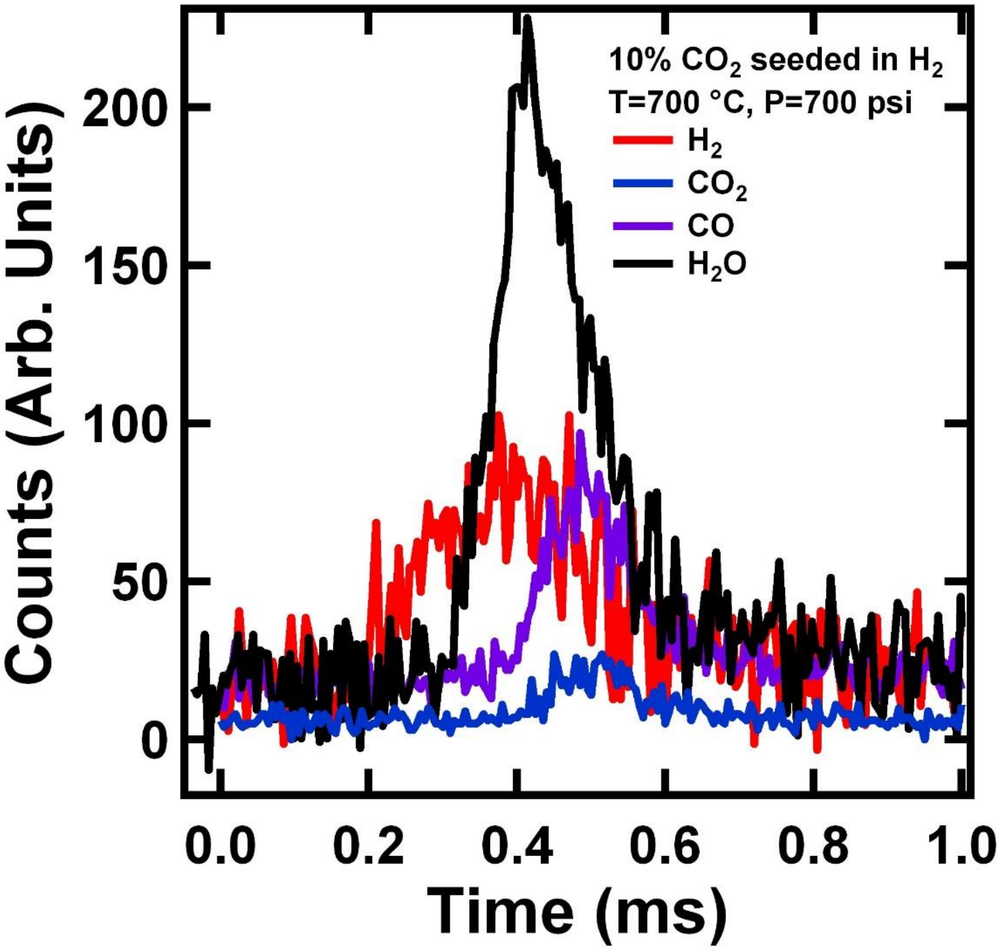

Figure A.26. TOF beam profiles for 10% CO_2 in H_2 gas mixtures at stagnation pressure 700 psi, with a nozzle temperature of 700 ℃. Spectra indicates H_2, CO_2, CO and H_2O gas species respectively.

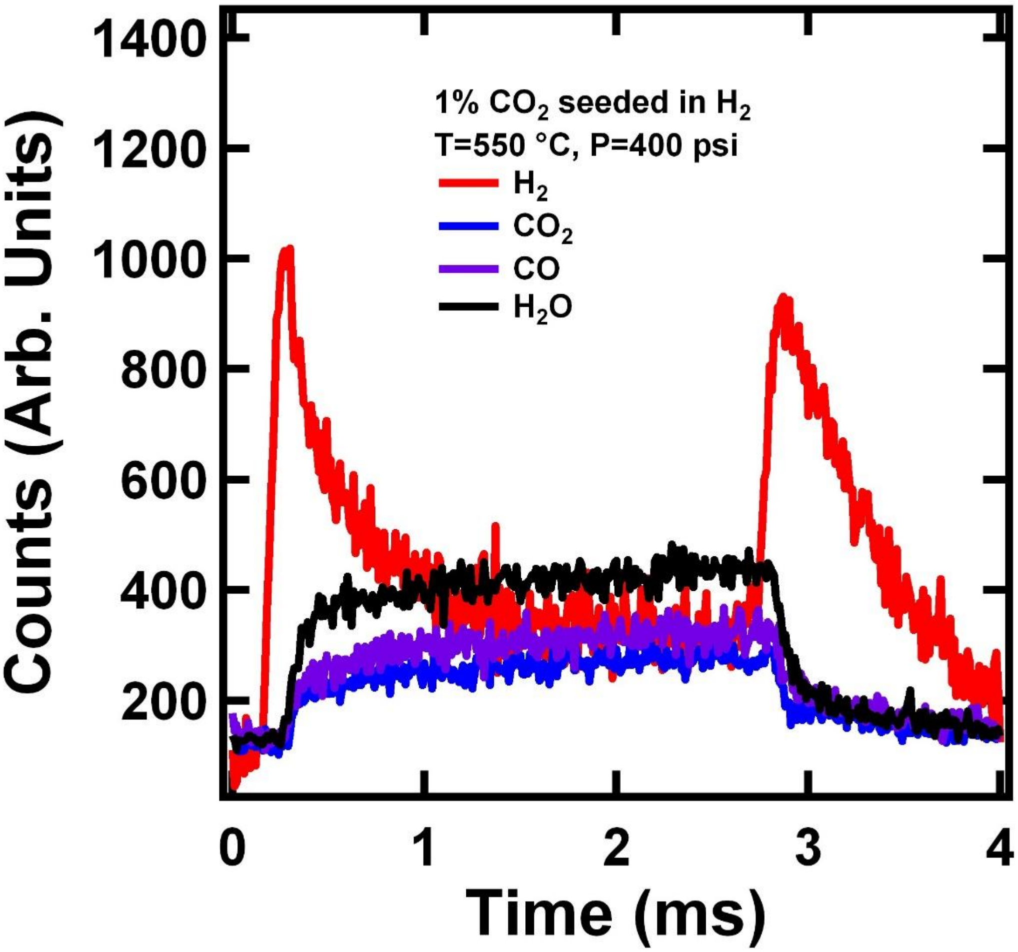

Figure A.27. SQW beam profiles for 1% CO_2 in H_2 gas mixtures at stagnation pressure 400 psi, with a nozzle temperature of 550 ℃. Spectra indicates H_2, CO_2, CO and H_2O gas species respectively.

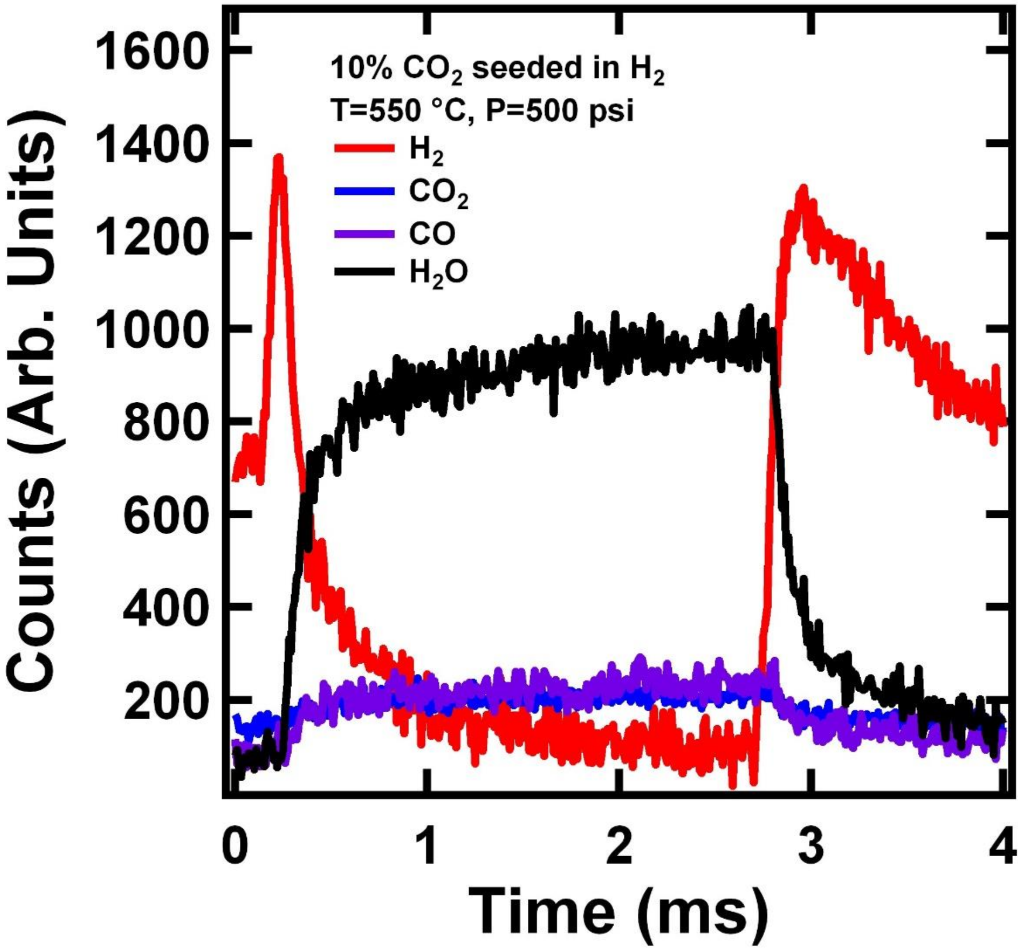

Figure A.28. SQW beam profiles for 1% CO_2 in H_2 gas mixtures at stagnation pressure 500 psi, with a nozzle temperature of 550 ℃. Spectra indicates H_2, CO_2, CO and H_2O gas species respectively.

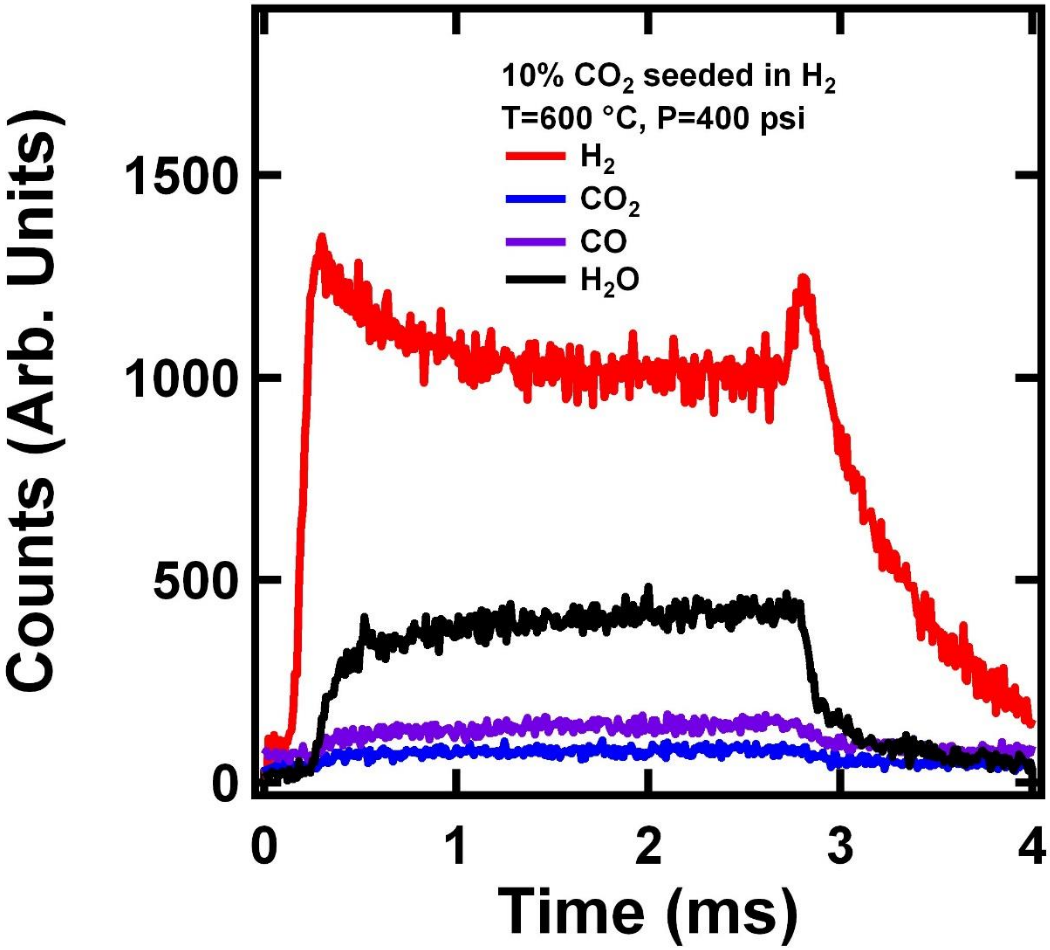

Figure A.29. SQW beam profiles for 1% CO_2 in H_2 gas mixtures at stagnation pressure 400 psi, with a nozzle temperature of 600 ℃. Spectra indicates H_2, CO_2, CO and H_2O gas species respectively.

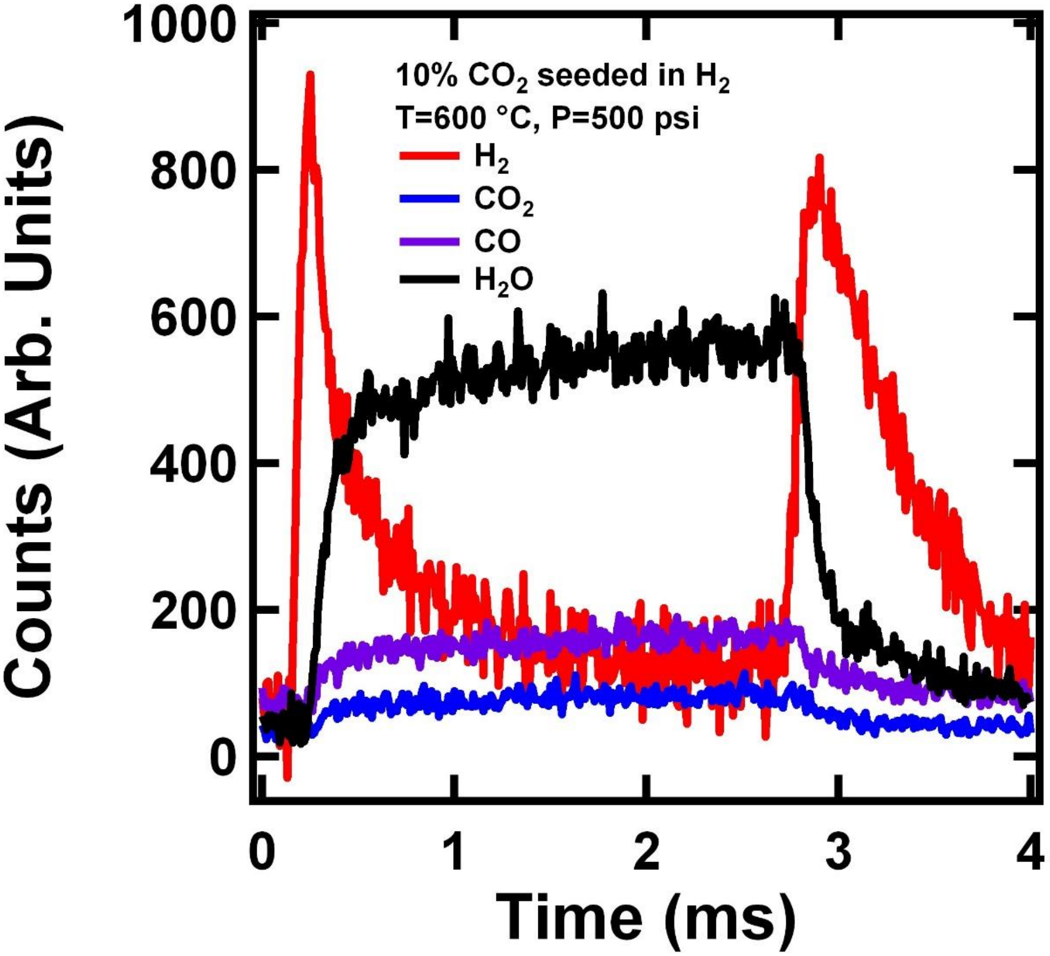

Figure A.30. SQW beam profiles for 1% CO_2 in H_2 gas mixtures at stagnation pressure 500 psi, with a nozzle temperature of 600 ℃. Spectra indicates H_2, CO_2, CO and H_2O gas species respectively.

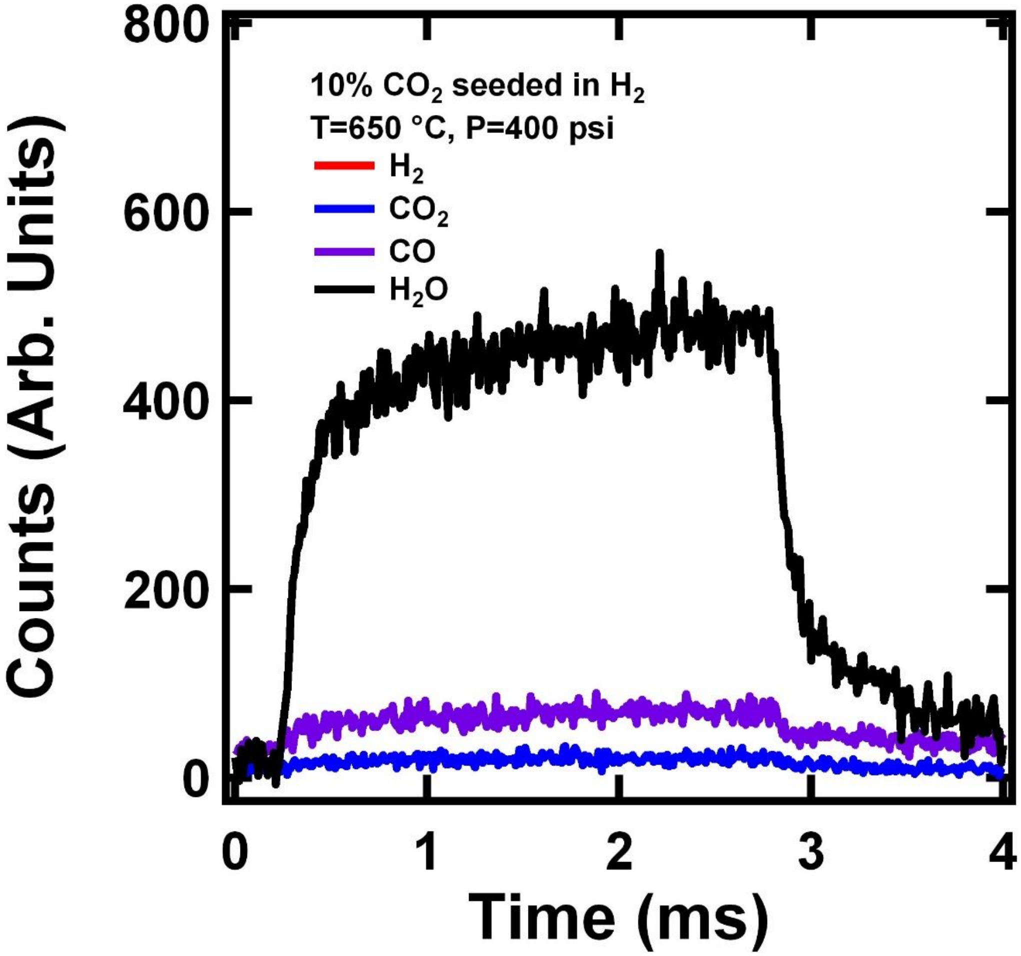

Figure A.31. SQW beam profiles for 1% CO_2 in H_2 gas mixtures at stagnation pressure 400 psi, with a nozzle temperature of 650 ℃. Spectra indicates H_2, CO_2, CO and H_2O gas species respectively.

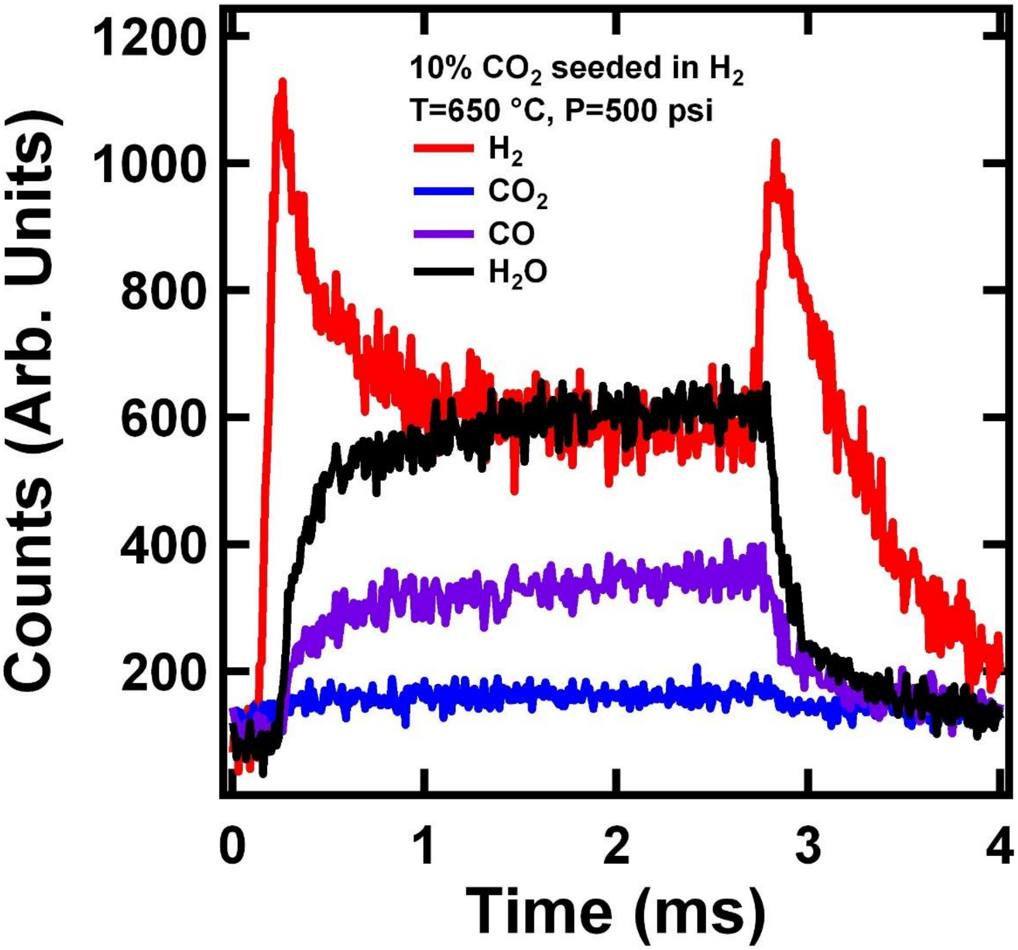

Figure A.32. SQW beam profiles for 1% CO_2 in H_2 gas mixtures at stagnation pressure 500 psi, with a nozzle temperature of 650 ℃. Spectra indicates H_2, CO_2, CO and H_2O gas species respectively.